Reactivation potential of fractures and faults

Zur Erlangung des akademischen Grades eines

Doktors der Naturwissenschaften (Dr. rer. nat.)

von der KIT Fakultät für Bauingenieur-, Geo- und Umweltwissenschaften
des Karlsruher Instituts für Technologie (KIT)

genehmigte

Dissertation

von

Felix Allgaier

aus Stuttgart

Tag der mündlichen Prüfung: 26. April 2024
Erster Gutachter: Prof. Dr. Christoph Hilgers
Zweiter Gutachter: Prof. Dr. Andreas Henk
Dritter Gutachter: Prof. Stephen Laubach, PhD

Karlsruhe (2025)

Acknowledgments

First and foremost, I am deeply indebted to my advisor Christoph Hilgers for his support, guidance and input of new ideas as an essential part of this work. He initiated the project that forms the essential basis of my doctoral thesis. Thank you for fruitful and long discussions, which have improved the quality of this work and also broadened my geoscientific horizon.

Andreas Henk and Stephen Ernest Laubach are thankfully acknowledged for their valuable contributions as co-referees for the examination of this thesis. I sincerely appreciate their time and effort in reviewing my dissertation, which has greatly contributed to its completion.

Benjamin Busch is thanked for his invaluable support and guidance in administrative matters as well as for always being available to evaluate new ideas. Beside long discussions, his profound knowledge and meticulous internal reviews significantly contributed to the quality of this work.

I would like to thank the entire Structural Geology group at KIT for making this journey an incredibly rewarding and enjoyable experience. Special thanks go to my office colleague Dennis Quandt for his support in collecting data in the field as well as for the entertaining time we spent together at KIT. Jonas Greve is thanked for enjoyable discussions that covered both geological and off-topic subjects, taking place both virtually and during our bouldering sessions. In addition, I would like to thank Ulrike Brecht for her support in dealing with the KIT bureaucracy. To my esteemed colleagues Agnes Kontny, Luis Baumgartner, Jasemin Ölmez, Martin von Dollen, Chaojie Cheng, Bruno Mendes, and Kevin Altinger, I am thankful for the welcoming and collegial atmosphere throughout my time in the institute.

Birgit Müller and Thomas Niederhuber are thankfully acknowledged for their expert reviews of my manuscripts, which considerably improved their quality.

I want to thank Nevena Andrić-Tomašević, Paul Baville, Giridas Maiti, Lucas Eskens, and Robin Ulwig from the General Geology group for the enjoyable lunch breaks and entertaining after-work gatherings.

Finally, I would like to express my deepest gratitude to my family and friends for their continuous support and presence. Special thanks go to my brother Moritz for always taking care when needed. I would especially like to thank my partner Katharina Steiger for her endless and loving support throughout the entire journey.

Abstract

Faults and fractures represent major controlling factors for subsurface fluid flow in sedimentary basins (Ruhr Basin and Upper Rhine Graben) in Germany and similar settings world-wide, and are therefore important for a range of geo-energy applications. Further, faults can present socio-technical challenges due to reactivation-induced seismicity, compromising the feasibility of geo-energy projects. This study aims to combine structural geological analysis with geomechanical approaches to assess the structural control of fractures and faults on fluid flow in two sedimentary basin settings (Ruhr Basin and Upper Rhine Graben, Germany). Moreover, this study aims to evaluate the potential risk of fault reactivation in the context of post-mining related flooding of abandoned hard coal mines (Ruhr Basin).

For the tight Upper Carboniferous sandstones of the Ruhr Basin (Germany), a better understanding of the fracture networks is crucial to understand subsurface fluid flow pattern, which is beneficial for the successful development of geo-energy utilization.

Two outcrops of Upper Carboniferous sandstones (Namurian C and Westphalian A), located along the southern part of the Variscan Ruhr Basin, are studied utilizing digital outcrop models for fracture detection and attribute quantification. The Namurian C outcrop near Hattingen is situated approximately 13 km west of the Westphalian A outcrop near Witten. In addition, the Bork 10 well provides a core description-based fracture data set, that allows the comparability of outcrop and subsurface to be assessed. The well penetrates the Upper Carboniferous (Westphalian A) approximately 30 to 40 km northeast of the outcrops, providing insights into the fracture inventory of the subsurface.

Comparable fracture orientation statistics are observed in both outcrops, with three dominant fracture trends detected: NNE-SSW to NE-SW (set 1), WNW-ESE (set 2), and NNW-SSE to N-S (set 3). For the additional analysis of the orientation statistics of the fracture data set of Bork 10, there is an acceptable agreement for fracture orientations between outcrop and subsurface. Two dominant N-S and W-E trends occur in the Bork 10 along with subordinate NNE-SSW and NW-SE striking fractures.

The Terzaghi-corrected averaged fracture intensity (P_{10}) exhibits variations between both outcrops for comparable fracture trends, ranging from 0.4 to 3.1 m^{-1}. These fracture intensities values are 1.1 to 4.5 times higher than the P_{10} values of comparable fracture orientations in the Bork 10 well.

Outcrop analysis indicates that the fracture height is limited by the thickness of the individual sandstone beds since the majority of the detected fractures is bed-restricted. Both outcrops are dominated by high-angle fractures with respect to bedding, while the Bork 10 data set is characterized by a mixture of intermediate to high-angle (w.r.t. bedding) fractures, indicating differences in the fracture inventory despite comparable orientation statistics. This discrepancy might be attributed to the different burial and uplift histories, as outcrops experienced uplift-related stress relief.

Identified fracture trends of the Bork 10 are geomechanically analyzed following the slip and dilation tendency concept to gain better understanding of stress-controlled subsurface fluid flow patterns in tight Upper Carboniferous sandstones. N-S as well as NW-SE trending near-vertical fractures are favorably oriented within the present-day stress field to be hydraulically conductive. Highest dilation tendencies are associated with NNW-SSE striking fractures.

Post-mining related flooding of abandoned hard coal mines in the water province “Haus Aden” (Ruhr Basin, Germany) might affect fault stability as stress conditions change. Based on a constructed 3D structural model of the NE part of the water province “Haus Aden” NW-SE to NNW-SSE trending normal faults are identified as the most susceptible fault trend for reactivation.

The probabilistic fault reactivation assessment, focused on NW-SE to NNW-SSE trending normal faults, is performed for a depth level of 1000 m below ground representing former mining levels. No reactivation potential is shown for considering a mine water rebound up to a depth level of 640 m below ground. Under hydrostatic conditions, a low reactivation potential is determined, requiring high differential stresses to exceed the chosen frictional fault strength ($\mu = 0.5$, $\mu = 0.67$). The overall low potential for fault reactivation aligns with the absence of observed natural seismicity in the eastern Ruhr Basin. This provides a promising setting for future geothermal applications, given that fault instability can pose a significant risk.

Further, a workflow is tested to account for the spatial variability of the frictional fault strength. To better capture the phenomena of along-strike and dip changes of the frictional strength, a model is established utilizing a non-perfect clay mixing model based on fault displacement and host rock clay content. Using the derived frictional fault strength model as input, a fault stability analysis is performed for a selected NNW-SSE trending normal fault. The fault is characterized by mostly stable, horizontally elongated patches and subordinate unstable zones. An additional low fault cohesion results in overall stable conditions. Generally, the tested workflow offers a suitable approach to improve the representation of the frictional fault strength in the context of fault stability analysis.

For the Upper Rhine Graben rift basin (Germany), a better understanding of fault-controlled fluid flow is crucial for de-risking the subsurface utilization in the context of fault-related geothermal applications. The stress control on hydrocarbon migration along a fault is exemplary demonstrated by the case of the fault-controlled hydrocarbon migration that has charged the former Leopoldshafen oil field (central Upper Rhine Graben).

The Leopoldshafen fault is structurally composed of two NNE-SSW trending segment, linked by a NNW-SSE to N-S striking left-stepping fault bend segment. The fault formed during the Oligocene rifting phase, generally providing a potential pathway for vertical migration of hydrocarbons that were expulsed during the Miocene. During the strike-slip stress field that has been active since the Miocene, highest slip and dilation tendencies are observed along the fault bend segment, indicating the preferential alignment for fluid flow. The fault was likely reactivated by (oblique) sinistral strike slip kinematics during the Miocene,

inducing dilational strain concentrated along the bend segment, as indicated by geomechanical modeling. Therefore, the Leopoldshafen fault bend might have acted as releasing bend, providing vertical pathways for hydrocarbon migration. This understanding of stress control on structural fault configurations might benefit the de-risking of exploration for geothermal and lithium brine mining in the Upper Rhine Graben.

Kurzfassung

Störungen und Brüche sind wesentliche Kontrollfaktoren für den unterirdischen Fluidfluss in Sedimentbecken (Ruhrbecken und Oberrheingraben) in Deutschland und in ähnlichen Gebieten weltweit und daher für eine Reihe von Geoenergieanwendungen von Bedeutung. Darüber hinaus können Störungen aufgrund von reaktivierungs-induzierter Seismizität sozio-technische Herausforderungen darstellen und dadurch die Durchführbarkeit von Geoenergieprojekten beeinträchtigen. Ziel dieser Studie ist es, strukturgeologische Analysen mit geomechanischen Ansätzen zu kombinieren, um die strukturelle Kontrolle von Brüchen und Verwerfungen auf den Fluidfluss in zwei Sedimentbecken (Ruhrbecken und Oberrheingraben, Deutschland) zu bewerten. Darüber hinaus zielt diese Studie darauf ab, das potenzielle Risiko einer Störungsreaktivierung im Zusammenhang mit der nachbergbaulichen Flutung stillgelegter Steinkohlebergwerke (Ruhrbecken) zu bewerten.

Für die dichten oberkarbonischen Sandsteine des Ruhrbeckens (Deutschland) ist ein besseres Verständnis der Bruchnetzwerke von entscheidender Bedeutung, um die unterirdischen Strömungsmuster zu verstehen, was für die erfolgreiche Entwicklung der Geoenergienutzung von Vorteil ist.

Zwei Aufschlüsse oberkarbonischer Sandsteine (Namur C und Westfal A) im südlichen Teil des variszischen Ruhrbeckens werden mit Hilfe digitaler Aufschlussmodelle zur Bruchdetektion und Attributquantifizierung untersucht. Der Aufschluss des Namur C bei Hattingen liegt ca. 13 km westlich des Aufschlusses des Westfal A bei Witten. Darüber hinaus liefert die Bohrung Bork 10 einen auf Kernbeschreibungen basierenden Bruchdatensatz, mit dem die Vergleichbarkeit von Aufschluss und Untergrund beurteilt werden kann. Die Bohrung, die sich etwa 30 bis 40 km nordöstlich der Aufschlüsse befindet, dringt in das Oberkarbon (Westfal A) ein und liefert dabei Einblicke in das Bruchinventar des Untergrunds.

In beiden Aufschlüssen werden vergleichbare Bruchorientierungsstatistiken beobachtet, wobei drei dominante Bruchtrends festgestellt wurden: NNE-SSW bis NE-SW (Set 1), WNW-ESE (Set 2) und NNW-SSE bis N-S (Set 3). Für die zusätzliche Betrachtung der Orientierungsstatistik des Bruchdatensatz der Bork 10, ergibt sich eine akzeptable Übereinstimmung für Bruchorientierungen zwischen Aufschluss und Untergrund. Dabei treten in der Bork 10 zwei dominante N-S- und W-E-Trends nebst untergeordneten NNE-SSW- und NW-SE-streichenden Brüchen auf.

Die Terzaghi-korrigierte gemittelte Bruchintensität (P_{10}) weist für vergleichbare Bruchtrends Schwankungen zwischen beiden Aufschlüssen auf, die von 0,4 bis 3,1 m 1 reichen. Diese Bruchintensitätswerte sind 1,1 bis 4,5 Mal höher als die P_{10}-Werte für vergleichbare Bruchausrichtungen in der Bohrung Bork 10.

Die Aufschlussanalyse deutet darauf hin, dass die Bruchhöhe durch die Mächtigkeit der einzelnen Sandsteinschichten begrenzt ist, da der Großteil der detektierten Brüche schichtgebunden ist. In beiden Aufschlüssen dominieren Brüche mit hohem Winkel zur Schichtung, während der Bork 10 Datensatz durch

eine Mischung aus Brüchen mit mittlerem bis hohem Winkel (zur Schichtung) gekennzeichnet ist, was trotz vergleichbarer Orientierungsstatistiken auf Unterschiede im Bruchinventar hinweist. Diese Diskrepanz könnte auf die unterschiedliche Versenkungs- und Hebungsgeschichte zurückzuführen sein, da die Aufschlüsse eine hebungsbedingte Spannungsentlastung erfahren haben.

Die identifizierten Bruchtrends der Bork 10 werden geomechanisch nach dem Konzept der Gleit- und Dilatationstendenz analysiert, um ein besseres Verständnis der spannungsgesteuerten unterirdischen Fließmuster in dichten Sandsteinen des Oberkarbons zu gewinnen. Sowohl N-S als auch NW-SE verlaufende nahezu vertikale Brüche sind innerhalb des rezenten Spannungsfeldes günstig orientiert, um hydraulisch leitfähig zu sein. Die stärksten Dilatationstendenzen sind mit NNW-SSE streichenden Brüchen assoziiert.

Die nachbergbaubedingte Flutung stillgelegter Steinkohlebergwerke in der Wasserprovinz "Haus Aden" (Ruhrbecken, Deutschland) könnte die Stabilität von Störungen beeinflussen, da sich die Spannungsbedingungen ändern. Auf der Grundlage eines konstruierten 3D-Strukturmodells des nordöstlichen Teils der Wasserprovinz "Haus Aden" wurden NW-SE bis NNW-SSE streichende Abschiebungen als die für eine Reaktivierung am anfälligsten Störungstrends identifiziert.

Die probabilistische Störungsreaktivierungs-Analyse, mit Fokus auf NW-SE bis NNW-SSE streichende Abschiebungen, erfolgt für eine Tiefe von 1000 m unter Gelände, die dem ehemaligen Bergbauniveau entspricht. Für die Berücksichtigung eines Grubenwasserrückpralls bis zu einer Tiefe von 640 m unter Gelände wird kein Reaktivierungspotenzial nachgewiesen. Unter hydrostatischen Bedingungen wird ein geringes Reaktivierungspotenzial ermittelt, das hohe Differenzialspannungen erfordert, um die ausgewählten Haftreibungen der Störungen ($\mu = 0{,}5$, $\mu = 0{,}67$) zu überschreiten. Das insgesamt niedrige Potenzial für die Reaktivierung von Verwerfungen steht im Einklang mit dem Fehlen einer zu beobachteten natürlichen Seismizität im östlichen Ruhrbecken. Dies bietet ein vielversprechendes Umfeld für künftige geothermische Anwendungen, da die Instabilität von Störungen ein erhebliches Risiko darstellen kann.

Darüber hinaus wird ein Workflow getestet, der die räumliche Variabilität der Haftreibung von Störungen berücksichtigt. Um das Phänomen der Veränderungen der Reibungsfestigkeit entlang des Streichens und Einfallens von Störungen besser zu erfassen, wird ein Modell mit einem nicht-perfekten Tonmischungsmodell auf der Grundlage des Störungsversatzes sowie des Tongehalts des Wirtsgesteins erstellt. Unter Verwendung des abgeleiteten Modells für die Reibungsfestigkeit der Störung wird eine Analyse der Störungsstabilität für eine ausgewählte NNW-SSE verlaufende Abschiebung durchgeführt. Die Störung ist gekennzeichnet durch überwiegend stabile, horizontal gestreckte Bereiche und untergeordnete instabile Zonen. Eine zusätzliche geringe Störungskohäsion führt zu insgesamt stabilen Bedingungen. Generell bietet der getestete Workflow einen geeigneten Ansatz, um die Darstellung der Reibungsfestigkeit von Störungen im Rahmen von Stabilitätsanalysen zu verbessern.

Für das Oberrheingraben-Riftbecken (Deutschland) ist ein besseres Verständnis des Störungs-gesteuerten Fluidflusses von entscheidender Bedeutung, um das Risiko der Nutzung des Untergrundes im Zusammenhang mit Störungsbedingten geothermischen Anwendungen zu senken. Die Spannungskontrolle bei der Kohlenwasserstoffmigration entlang einer Verwerfung wird beispielhaft am Fall der Störungsgesteuerten Kohlenwasserstoffmigration demonstriert, die das ehemalige Leopoldshafen Ölfeld (mittlerer Oberrheingraben) gefüllt hat.

Die Leopoldshafen Störung besteht strukturell aus zwei NNE-SSW streichenden Segmenten, die durch ein NNW-SSE bis N-S streichendes, linksschreitendes Störungsbiegesegment verbunden sind. Die Störung bildete sich während der oligozänen Rifting-Phase und bietet im Allgemeinen eine potenzielle Wegsamkeit für die vertikale Migration von im Miozän freigesetzten Kohlenwasserstoffen. Während des seit dem Miozän aktiven Strike-Slip Spannungsfeldes werden entlang des Störungsbiegesegments die höchsten Gleit- und Dilatationstendenzen beobachtet, was auf eine bevorzugte Ausrichtung für die Fluidleitung hinweist. Die Störung wurde wahrscheinlich während des Miozäns durch eine (schräge) sinistrale Strike-Slip Kinematik reaktiviert, was zu Dehnung führte, die sich entlang des Bogensegments konzentrierte. Daher könnte das Biegesegment der Leopoldshafener Störung als sogenanntes Releasing Bend gewirkt haben, das Wegsamkeiten für die vertikale Migration von Kohlenwasserstoffen bietet. Dieses Verständnis der Kontrolle von Spannung auf strukturelle Störungskonfigurationen könnte sich positiv auf die Risikominderung bei der Exploration für die Geothermie und den Lithium-Sole-Abbau im Oberrheingraben auswirken.

Contents

Declaration of originality

Chapter 2: As first author, Felix Allgaier evaluated and combined the dataset. He collected field data with assistance from the co-authors Benjamin Busch and Dennis Quandt, which was highly appreciated. He performed data analysis with assistance by co-author Thomas Niederhuber. He wrote the entire article with inputs from Benjamin Busch, Thomas Niederhuber, Dennis Quandt, Birgit Müller and Christoph Hilgers. The discussion with all co-authors contributed to this manuscript.

Chapter 3: As first author, Felix Allgaier evaluated and analyzed the dataset. He performed the modeling with assistance by co-author Benjamin Busch. He wrote the entire article with inputs from Thomas Niederhuber, Benjamin Busch, Birgit Müller and Christoph Hilgers. The discussion with all co-authors contributed to this manuscript.

Chapter 4: As first author, Felix Allgaier evaluated, combined and analyzed the dataset. He performed modeling with assistance by co-author Benjamin Busch. He wrote the entire article with inputs from Benjamin Busch and Christoph Hilgers. The discussion with all co-authors contributed to this manuscript.

1 Introduction

1.1 Motivation

Faulted and/or fractured sedimentary basin settings, such as the Cenozoic Upper Rhine Graben rift basin or the Ruhr Basin as a Variscan foreland basin (Germany), host diverse geo-energy applications, encompassing geothermal energy extraction (Hanano 2004; Dezayes et al. 2010; Vidal and Genter 2018; Zucchi 2020), hydrocarbon production (Aydin 2000; Narr et al. 2006; Gale et al. 2014), CO_2 sequestration (Iding and Ringrose 2010; March et al. 2017; Vo Thanh et al. 2019), and hard coal mining (Drozdzewski 1993), underscoring their pivotal role in subsurface utilization. Beyond the influence of fractures and faults on subsurface fluid flow patterns (Moretti 1998; Ameen et al. 2010), fractures can control reservoir quality (Watkins et al. 2018; Bagni et al. 2020) and thus fluid injection and extraction rates (Bödvarsson and Tsang 1982; Questiaux et al. 2010), while faults can additionally pose socio-technical challenges in case of reactivation-induced seismicity (Streit and Hillis 2004; Moeck et al. 2009; Diehl et al. 2017). This applies to the Upper Rhine Graben, where faults impact deep geothermal systems (Bächler et al. 2003) as well as hydrocarbon migration and the formation of structural traps (Bruss 2000; Durst 1991; Reinhold et al. 2016). In the Ruhr area, fractured and/or faulted lithologies offer opportunities for geothermal applications; moreover, fault stability can be influenced by stress changes associated with post-mining activities following the cessation of coal mining in 2018.

To study fracture networks, outcrops provide opportunities to overcome limitations associated with sampling challenges and the directional bias of one-dimensional well data (Terzaghi 1965; La Pointe et al. 1993; Laubach et al. 2000; Laubach et al. 2019) as well as the resolution limitations of seismic surveys (Wennberg et al. 2006; Leckenby et al. 2007; Gillespie et al. 2011). Digital outcrop models enable fracture detection and automated measurement of geometric attributes (Figure 1.1) (Becker et al. 2018; Larssen et al. 2020). A strategic combination of outcrop and subsurface data provides a promising approach for a refined fracture network characterization. However, the general suitability of outcrops to serve as reservoir analogues needs to be validated by comparison with subsurface datasets (Figure 1.1) (Becker et al. 2018). Fracture pattern can form due to tectonic stresses (inducing folding and faulting), fluid overpressure or uplift and erosion (Laubach 1988; Cosgrove 2015), which can result in characteristic differences between outcrop and subsurface datasets that have undergone different burial and/or uplift histories. Fracture network characterization involves the quantification of key characteristic parameters such as orientation statistics, intensities, and geometric attributes, required for subsequent fractured reservoir (DFN) modeling (Figure 1.1). The potential of fractures to conduct fluid is commonly assumed to be primarily controlled by the present-day stress field (Barton et al. 1995; Becker et al.

2019b; Mattila and Tammisto 2012). However, chemical alterations, including precipitation or dissolution, can serve as additional controls (Hilgers et al. 2004), such as cement bridges providing resistance to fracture closure (Laubach et al. 2004).

Faults, generally considered as larger-scale shear fractures, control subsurface fluid flow pattern along as well as across-fault by either acting as seals (Bredehoeft and Belitz 1992; Wibberley et al. 2017; Ogilvie et al. 2020), conduits (Moretti 1998; Alexander and Handschy 1998; Smeraglia et al. 2022) or as a combination of both (Bense and Person 2006). Along-fault hydrocarbon migration occurs as cyclic fluid pulses along tectonically active faults, with fluid pathways temporarily opened by seismic fault activity (Hooper 1991; Haney et al. 2005; Smeraglia et al. 2022). Based on across-fault thickening of the synrift sequence, fault activity can be identified by calculating the Expansion Index (Figure 1.1) (Thorsen 1963; Jackson and Rotevatn 2013). Barton et al. (1995) demonstrated the relationship between in-situ stress and fluid flow in faulted rock, indicating that the permeability is highest for preferentially oriented faults. Therefore, the slip tendency concept assists as a geomechanical proxy to identify fault segments which are prone to slip and, thus, potentially conductive (Figure 1.1) (Morris et al. 1996; Worum et al. 2004)**.**

The spatial deformation distribution within fault damage zones varies along-strike and dip (Nixon et al. 2020), with sites of elevated structural complexity (e.g. relay zones, fault bends) associated with higher fracture intensities (Rotevatn and Bastesen 2014; Nixon et al. 2019). To investigate the spatial distribution of fault slip-induced strain around active faults, the Fault Response Modelling tool (MOVE software suite) provides a promising modeling approach (Figure 1.1). Therefore, linking geometric fault characteristics, fault activity history, and geomechanical proxies, as well as with a geomechanical modeling approach can provide a refined understanding of structural-control on fluid flow patterns.

Active faults can slip in response to stress or pore pressure alterations, either naturally or anthropogenically induced. Beside impacting fault-controlled fluid migration, this can challenge seal integrity of subsurface storage applications (Orlic et al. 2011; Kaldi et al. 2013), put the development of geothermal projects at risk (Edwards et al. 2015) or lead to post-mining related microseismicity (Donnelly 2006; Donnelly et al. 2008). Estimating the stress state of faults prior to any subsurface operation is key, either using a deterministic or probabilistic approach (Healy and Hicks 2022) by applying measures to quantify the tendency of faults to slip under given stress conditions (Figure 1.1) (Morris et al. 1996).

Fault slip analyses usually consider the Mohr-Coulomb frictional failure theory and use a single frictional strength threshold (μ) in order to assess the static situation prior to the onset of potential fault slip (Moeck et al. 2009; López 2012; Vadacca et al. 2021; Ekpo Johnson et al. 2023; Zhang et al. 2023). Therefore, μ is referred to as the static friction coefficient, in contrast to dynamic friction which acts during fault slip. However, the geological complexity of fault zones and the associated spatial heterogeneity of the fault rock composition, challenges the representation of the faults' frictional strength by a single static friction coefficient (μ). This is indicated by outcrop studies, demonstrating along-strike and

dip variations of the frictional fault strength (μ) (Childs et al. 1997), which is controlled by e.g. fault displacement and host rock lithology. This spatial heterogeneity cannot be measured or captured for subsurface faults, so a modeling approach might provide the best possible estimate. Extending the common fault slip analysis approach by utilizing the modeling of the spatial variability of the friction coefficient (μ) might provide useful insights into the spatial variation of fault stability (Meng et al. 2017; Jin et al. 2023).

Geo-engineering challenges associated with the naturally fractured Upper Carboniferous tight sandstones (Ruhr Basin), such as mine-flooding related microseismicity, post-mining management and geothermal utilization require a profound understanding of the fracture network in terms of its impact on structurally-controlled reservoir quality as well as on fluid flow patterns. Due to the generally poor reservoir qualities of the Upper Carboniferous tight sandstone matrix (mean porosity: 6.8 %, mean permeability: 0.18 mD) (Greve et al. 2023), fractures are the primary control on subsurface fluid flow, besides the subsurface mining infrastructure (shafts and drifts). The study of the fracture network hosted in Upper Carboniferous sandstones contributes to establish a fracture data basis for future geo-engineering challenges, such as deep geothermal heat production or post-mining-related flooding of abandoned hard coal mines.

Post-mining-related flooding of abandoned hard coal mines applies to the eastern Ruhr Basin, which entered the post-mining phase in 2018, and where changes in subsurface stress conditions are induced by the increase in pore pressure due to the mine water rebound. This may affect fault stability, since hard coal mining has been concentrated in areas between major fault zones. The detailed assessment of fault reactivation potential may also be beneficial to reduce risk for the roll-out of deep geothermal in the Ruhr Basin targeting fault zones. Thus, the water province “Haus Aden”, which hosts the former “Bergwerk Ost” colliery (near Bergkamen, Germany), serves as a case study since legacy data is available for structurally modeling the Upper Carboniferous subsurface.

Fluid migration in the Upper Rhine Graben is generally described as fault-controlled (Bruss 2000; Bächler et al. 2003; Schleicher et al. 2006). In addition to intra-basin faults being linked to geothermal anomalies (Bächler et al. 2003), Bruss (2000) suggests that faults may have played a significant role as pathways for hydrocarbon migration in the central Upper Rhine Graben. This is supported by the presence of hydrocarbon inclusions in fault-related ore mineralization along the eastern graben shoulder (Werner and Dennert 2004). However, a detailed structural-geomechanical study for identifying structural configuration of hydraulically conductive faults is missing. Especially in the context of deep geothermal exploration and production in the Upper Rhine Graben, a detailed understanding of hydraulically conductive fault settings is required before drilling for reducing overall project risk by successfully targeting permeable fault zones. Thus, published data of the fault-bounded Leopoldshafen oil field (near Karlsruhe-Leopoldshafen, Germany) enable the assessment of fault-controlled fluid migration, which charged the Cenozoic clastic reservoir that was in production from 1957 until 1986 (Reinhold et al. 2016).

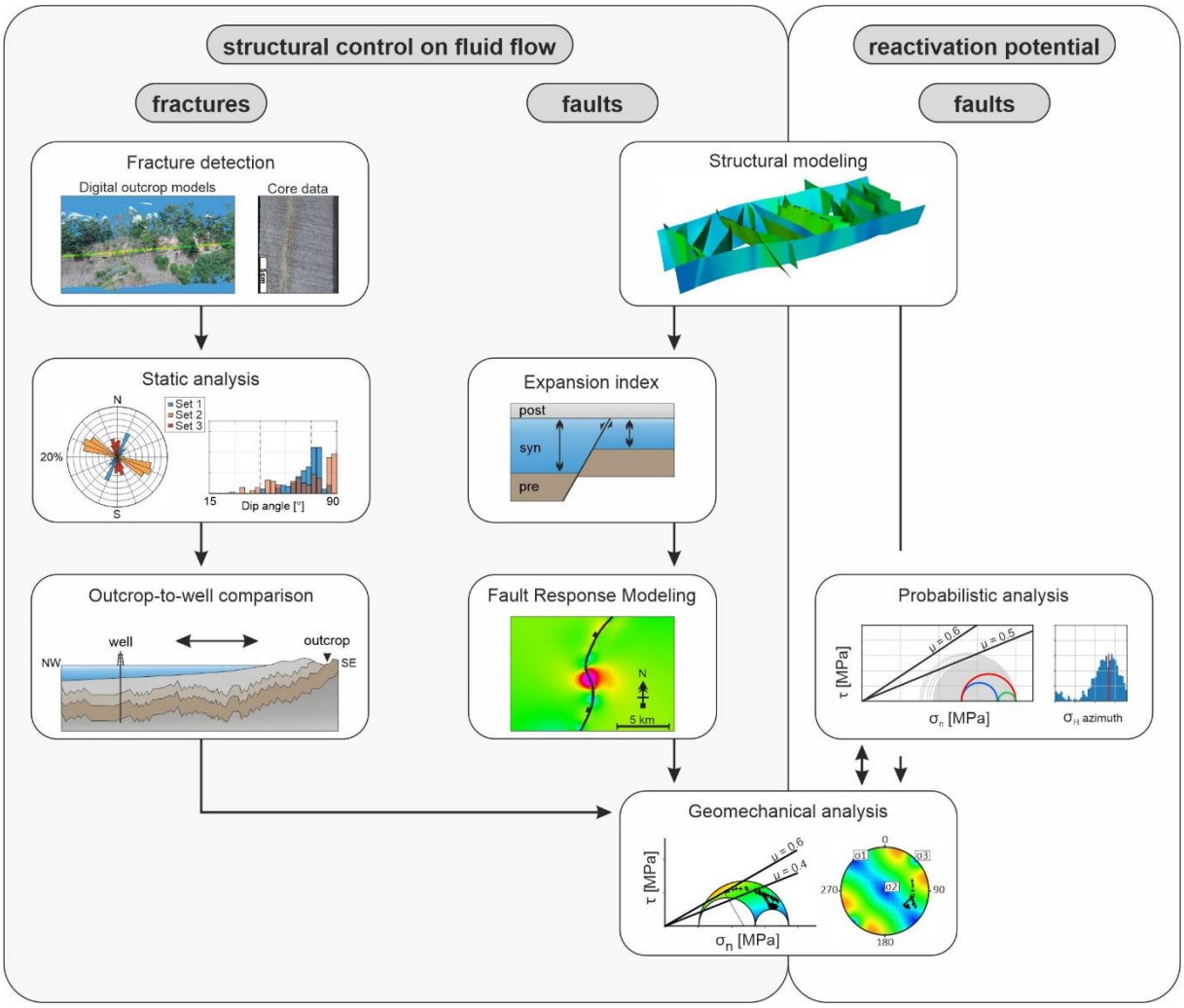

Figure 1.1: The methodical approach of this study aims to detect and describe fracture networks as well as to assess fractures and faults in terms of their impact on structurally controlled fluid flow and reactivation potential.

1.2 Aims and objectives

This study aims to enhance the understanding of the structural control on subsurface fluid flow in two sedimentary basin settings, in the Ruhr Basin as a Variscan foreland basin and the Cenozoic Upper Rhine Graben rift basin, alongside assessing the potential of mine-flooding induced fault reactivation (Ruhr Basin).

Naturally fractured outcrops are analyzed and linked to an evaluated subsurface dataset to analyze the suitability of Upper Carboniferous sandstone outcrops to serve as reservoir analogues in the Ruhr Basin. Geomechanical proxies are applied to identify directional preferences for present-day stress-controlled fluid flow in fractures. In order to refine the understanding of fault-controlled fluid migration, a proven fault-related hydrocarbon accumulation in the Upper Rhine Graben is studied to assess the fluid pathway potential along the Leopoldshafen fault. Legacy data is utilized for reservoir modeling in order to assess the potential of fault reactivation due to rising mine water levels in currently flooded hard coal mines (water province “Haus Aden”, eastern Ruhr Basin).

The works’ focus results in five major aspects:

- The fracture detection and characterization based on digital outcrop models as well as the fracture attribute comparison with wellbore data to investigate the outcrops’ suitability to serve as reservoir analogues.
- The assessment of stress control on fluid flow potential by applying geomechanical proxies and/or simulation.
- The construction of a 3D structural model utilizing hard coal mining legacy data.
- The probabilistic assessment of fault reactivation potential in the context of mine-flooding.
- Additionally, a workflow is developed to capture the heterogeneity of the frictional strength of faults in the context of analyzing fault stability.

1.3 Overview of thesis

1.3.1 Fracture network characterisation of the naturally fractured Upper Carboniferous sandstones combining outcrop and wellbore data, Ruhr Basin, Germany (chapter 2)

In this chapter, the fracture network attributes of the naturally fractured Upper Carboniferous sandstones (Ruhr Basin) are characterized and quantified through an integrated approach that utilizes outcrop data in combination with wellbore data (core description, dipmeter log). Two outcrop locations along the southern edge of the Ruhr Basin (exposing the Namurian C and Westphalian A) are studied by utilizing UAV derived 3D digital outcrop models and compared to subsurface data from the basin center.

Digital outcrop model based fracture detection of two Upper Carboniferous tight sandstone outcrops (Kaisberg Sandstone, Namurian C; Finefrau Sandstone, Westphalian A) revealed three prominent fracture orientations: NNE-SSW to NE-SW (set 1), WNW-ESE (set 2), and NNW-SSE to N-S (set 3). We show that bed thickness is the primary factor limiting fracture height, as outcrop fractures are mostly bed-restricted. We compare two fracture detection approaches based on well data (core description and dipmeter log), with dipmeter log fracture interpretation and fractures from core description showing a poor match for depth location (± 6m) and dip azimuth (± 25°). Analysis of oriented Upper Carboniferous sandstone core material indicates N-S and W-E trends as dominant fracture orientations.

We compare fracture attributes (strike, dip) and intensity (P_{10}) between outcrops and well to assess the outcrops suitability to serve as reservoir analogue. The strike direction of outcrop-derived fractures is broadly consistent with subsurface fractures, while differences in dip angles (bedding dip removed) are evident. Fracture intensity (P_{10}) is 1.1 to 4.5 times higher for both outcrops than for comparable fracture orientations observed in the wellbore dataset. By performing a critically stressed fracture analysis using the MATLAB software, we identify N-S and NW-SE trending fractures as potentially conductive under present-day stress conditions, assuming stress-controlled fluid flow in fractures.

1.3.2 Post-mining related reactivation potential of faults hosted in tight reservoir rocks around flooded coal mines, eastern Ruhr Basin, Germany (chapter 3)

This chapter introduces a probabilistic assessment of the fault reactivation potential in order to study how rising mine water levels in a flooded hard coal mine affect fault stability in the eastern Ruhr Basin. In addition, a workflow is proposed to incorporate the spatially heterogeneous character of the frictional fault strength into the assessment of fault stability, in order to better represent the fault's frictional strength.

Based on 2.5 dimensional legacy data, a workflow is developed to construct a structural 3D model of the study area to evaluate the structural inventory as well as to serve as methodological basis for the FloodRisk project partner. The complex fault zone architecture of one of the graben-bounding normal faults (Fliericher Sprung) is resolved by depth structure map data, indicating resolution limitations of the structural 3D model.

We identified NW-SE to NNW-SSE trending normal faults to be the most susceptible fault trend for reactivation under normal faulting stress conditions. We perform a probabilistic assessment (using Python) of the fault reactivation potential of these NW-SE to NNW-SSE trending normal faults, accounting for input parameter uncertainty regarding the stress field as well as geometric fault attributes. Assuming a mine water rebound up to a level of 640 m below ground affecting the pore pressure conditions around the faults, reactivation is unlikely. Considering hydrostatic pore pressure conditions in the faults' vicinity, slip tendencies of NW-SE to NNW-SSE trending normal faults rarely exceed the failure thresholds,

only under high differential stresses ($T_S > \mu = 0.67$ in 5 % of the realizations; $T_S > \mu = 0.5$ in 19 % of the realizations), indicating that fault reactivation is rather unlikely.

This is supported by the results of the fault stability analysis, exemplarily preformed for a chosen NNW-SSE trending normal fault, utilizing the modelled frictional fault strength property. Quantified Failure Criterion Stress (FCS) varies along the analyzed fault, which is characterized by stable patches (FCS < 0) associated to zones of intermediate to high frictional fault strength as well as by unstable patches (FCS > 0) linked to zones of lower friction coefficients. This might challenge the general application of a single friction coefficient for the analysis of fault stability.

1.3.3 Understanding fault leakage and reservoir charging in the Upper Rhine Graben, Germany – Assessment of the Leopoldshafen fault bend (chapter 4)

This study focuses on the hydrocarbon migration in case of the fault-related, abandoned Leopoldshafen oil field to refine the understanding of how faults control fluid flow in the central Upper Rhine Graben. The concepts of slip and dilation tendency are used as geomechanical proxies for stress-controlled fault conductivity. The Fault Response Modelling module (MOVE^{TM}), a geomechanical tool to model fault-related deformation, is utilized to derive faulting-induced subsurface strain distributions for fault activity during the Miocene phase of basin development. Fundamental 3D structural modeling is based on the regional-scale, publicly available GeORG data set, which provides a 3D geomodel constructed using on 1-, 2-, and 3-dimensional subsurface data.

Along-strike geometry changes are observed for the Leopoldshafen fault, which consists of two major NNE-SSW striking fault segments linked by a NNW-SSE to N-S trending left-stepping fault bend segment. The onset of fault activity, as confirmed by the Expansion Index analysis, can be linked to the Oligocene phase of graben formation. It is likely that fault activity extended during the main phase of hydrocarbon expulsion in the Miocene. We show that, within the strike-slip faulting regime since the Miocene, highest slip and dilation tendencies are located along the left-stepping fault bend segment.

Fault Response Modelling provided insights into the spatial strain distribution caused by (obliquely) sinistral fault slip. The results indicate the fault bend segment to have acted as releasing bend during Miocene fault activity, enabling vertical hydrocarbon migration along the Leopoldshafen fault to charge the Cenozoic Leopoldshafen oil field from deeper parts of the basin.

1.4 Parts of this thesis which have been published

Articles

Allgaier, F., Busch, B., Niederhuber, T., Quandt, D., Müller, B., Hilgers, C., 2023. Fracture network characterisation of the naturally fractured Upper Carboniferous sandstones combining outcrop and wellbore data, Ruhr Basin, Germany, Z. Dt. Ges. Geowiss. (J. Appl. Reg. Geol.), Vol. 173(4), p. 559-623

Allgaier, F., Busch, B., Hilgers, C., 2023. Fault leakage and reservoir charging in the Upper Rhine Graben, Germany – Assessment of the Leopoldshafen fault bend, Journal of Marine and Petroleum Geology, Vol. 153, p. 106428.

Allgaier, F., Niederhuber, T., Busch, B., Müller, B., Hilgers, C., 2024. Post-mining related reactivation potential of faults hosted in tight reservoir rocks around flooded coal mines, eastern Ruhr Basin, Germany, Geomechanics for Energy and the Environment, Vol. 38, p. 100560.

Conference contributions

Allgaier, F., Niederhuber, T., Quandt, D., Busch, B., Müller, B., Hilgers, C., 2021. Integrating digitized fracture data in geological 3D models, Upper Carboniferous, Ruhr Area, Germany. DGMK/ÖGEW Frühjahrstagung 2021, Celle.

Allgaier, F., Busch, B., Niederhuber, T., Müller, B., Hilgers, C., 2021. Fracture network characterization and DFN modelling of the Upper Carboniferous, Ruhr Area, Germany. Annual Conference of the German Geological Society (DGGV), Karlsruhe.

Allgaier, F., Busch, B., Quandt, D., Hilgers, C., 2022. Fracture network characterization and critically stressed fracture analysis in a naturally fractured tight gas sandstone analogue. DGMK/ÖGEW Frühjahrstagung 2022, Celle.

Allgaier, F., Busch, B., Quandt, D., Hilgers, C., 2022. Fracture network characterization of a naturally fractured tight gas reservoir analogue. 83rd EAGE Annual Conference & Exhibition, Madrid.

Allgaier, F., Busch, B., Hilgers, C., 2022. Transtensional fault segments and fluid migration in the Upper Rhine Graben. Annual Conference of the German Geological Society (DGGV), Cologne.

Contributions to other published works

Rische, M., Fischer, K. D., Allgaier, F., Friederich, W., 2021. Induced micro seismicity due to raising mine water level in former coal mines in the eastern Ruhr area (Germany). European Geosciences Union General Assembly (EGU 2021), Online.

Sawant, A. D., Allgaier, F., Busch, B., Hilgers, C., 2021. Refining workflow for obtaining subseismic-scale fracture density along scan lines (P10) in reservoir analogs. Annual Conference of the German Geological Society (DGGV), Karlsruhe.

Niederhuber, T., Müller, B., Müller, L., Röckel, T., Schilling, F., Allgaier, F., Rische, M., 2021. Slip tendency of faults and pore pressure evolution in the “Wasserprovinz Haus Aden” – Ruhr area. Annual Conference of the German Geological Society (DGGV), Karlsruhe.

Ukelis, O., Allgaier, F., Niederhuber, T., Rettenmaier, D., Zorn, R., 2022. Soil gas surveys for post-mining flooding monitoring. Annual Conference of the German Geological Society (DGGV), Cologne.

Ukelis, O., Allgaier, F., Niederhuber, T., Rettenmaier, D., Zorn, R., 2023. Short-term soil gas measurements for fault detection – Step 1 for post-mining flooding monitoring [Kurzzeit-Bodengasmessungen zur Störungsdetektion – Schritt 1 für das nachbergbauliche Flutungsmonitoring], Z. Dt. Ges. Geowiss. (J. Appl. Reg. Geol.), Vol. 173(4), p. 637-651.

Niederhuber, T., Rische, M., Müller, B., Röckel, T., Allgaier, F., Fischer, D. F., Schilling, F., Friederich, W., Geomechanics of Flooding-Induced Microseismicity – A Case Study from the Ruhr Coal Mining District in Germany (Submitted)

2 Fracture network characterisation of the naturally fractured Upper Carboniferous sandstones combining outcrop and wellbore data, Ruhr Basin, Germany

2.1 Abstract

Fractures in subsurface lithologies globally host economically significant energy resources and can be preferential fluid migration pathways. With the naturally fractured Upper Carboniferous sandstones of the Ruhr basin located within Germany's most densely populated area, the utilization for powering one of Europe's largest district heating infrastructure can be an option. Since the Upper Carboniferous sandstone matrix exhibits poor reservoir quality (average porosity: 8 %, permeability: up to 3 mD), fractures are believed to primarily control fluid flow. By combining data from two outcrops (exposing the Namurian C and Westphalian A) with a wellbore data set (penetrating the Westphalian A), this study aims to develop a refined understanding of the fracture network. The present-day stress control on hydraulically conductive fracture orientations is studied by performing critically stressed fracture analysis for three different S_{Hmax} orientation scenarios.

Kaisberg (Namurian C) and Finefrau (Westphalian A) sandstone outcrops show three dominant fracture trends: NNW-SSE to N-S, NNE-SSW to NE-SW and WNW-ESE. The characterized fracture networks of both outcrops follow a top-bounded height distribution pattern, with fractures being mostly bed restricted. Therefore, bed thickness is identified as a controlling factor limiting fracture height.

Based on 600 m of oriented core material from the Upper Carboniferous strata (Bork 10 wellbore), the analysis of the in-situ fracture network revealed two dominant fracture orientations: N-S and W-E. Fracture intensity indicates a varying degree of fracturing of the drilled sandstone layers for both trends (N-S: 0 to 9.1 m^{-1}, W-E: 0 to 8.8 m^{-1}). Comparison of dipmeter log fracture interpretations with reliable core description data shows a poor match (11 %) for depth location (± 6 m) and dip azimuth (± 25°).

Slip tendency analysis highlighted near-vertical N-S and NW-SE striking fractures to be generally favorably oriented for reactivation within the active stress field. In total, 10 % of the detected fracture population (Bork 10 wellbore) are critically stressed under present-day stress conditions and may contribute to large scale fluid flow in the subsurface.

2.2 Introduction

Fractured reservoirs host many economically significant geothermal, petroleum and water resources worldwide (Nelson 1985; Committee on Fracture Characterization and Fluid Flow 1996; Berkowitz 2002; Vidal and Genter 2018; Glaas et al. 2021). In the context of geothermal energy and CO_2 sequestration as a contribution for a low carbon energy future, fractured reservoirs may play an important role to reach national and global climate targets (Finkbeiner et al. 2019).

Fractured reservoirs are generally characterized by the rock matrix providing storage capacity, while fractures at different scales are controlling hydraulic connectivity (Ramsay J. G. and Huber M. I. 1987; Barton et al. 1995; Berkowitz 2002; Leckenby et al. 2007). To understand fluid flow in naturally fractured lithologies, detailed knowledge about the fracture network's geometric attributes and the applied stress state are crucial, as they can control fracture permeability (Zhang et al. 1996; Berkowitz 2002). All these information feed into a detailed model of the natural fracture network, required to minimize exploration risk and improve production performance (Harstad et al. 1995; Weijermars et al. 2011).

Fracture network characterization is a challenging task due to the sparse amount of available subsurface data (Leckenby et al. 2007; Laubach et al. 2019). Wellbore data provide 1D in-situ information, but are often limited for obtaining fracture attributes (La Pointe et al. 1993; Laubach et al. 2019). Fractures and their properties can only be studied directly in core material, which is often subject to limited availability (Gholipour et al. 2016). Seismic surveys as an indirect sampling method are also limited, since fractures generally are on the sub-seismic scale (Leckenby et al. 2007). Outcrops generally provide additional information on fracture attributes avoiding the limitations of wellbore data and seismics (Bisdom et al. 2014; Wüstefeld et al. 2018; Becker et al. 2018; Laubach et al. 2019). Therefore, integrating outcrop studies into fracture network characterization workflows may be strategically important (Laubach et al. 2019).

To understand the anisotropic character of fracture permeability, its stress sensitivity has to be studied in addition to the characterization of fracture orientation. Barton et al. (1995) demonstrated the dependency of fracture permeability on orientation under present-day stress conditions by correlating critically stressed fractures with hydraulic conductivity. Therefore, geomechanical analyses reveal that critically stressed fractures are more likely to be hydraulically conductive (Zoback 2007), which has implications for wellbore trajectory design (Ehlig-Economides et al. 2000; Verma et al. 2007; Franquet et al. 2008; Aghajanpour et al. 2018).

Detailed knowledge about pre-existing natural fractures is crucial for hydraulic stimulation operations in the context of permeability enhancement (McClure and Horne 2014; Wang et al. 2018). Shear stimulation is often considered for geothermal EGS projects (McClure and Horne 2014), hosted in naturally fractured lithologies in order to improve hydraulic inter-well connectivity (Committee on Fracture Characterization and Fluid Flow 1996; Zimmermann et al. 2010; Chabora et al. 2012).

The Ruhr region with a population of 5.1 million, is the most densely populated area in Germany, being part of Europe's largest district heating infrastructure (EnergieAgentur.NRW 2014). With the German heat demand largely covered by fossil fuels (Büsche 2014; IEA 2020), the decarbonization of the heat system is urgently needed in the context of reaching the European Green Deal and the German climate protection targets (Bundesministerium der Justiz 2019; European Commission 2020; IEA 2020).

Utilizing geothermal heat to cover the heat demand with renewable energies, is demonstrated by the City of Munich as a leading example (Büsche 2014; Weber et al. 2019). Following this concept, the City of Vienna is planning to use geothermal heat production with the aim to reach its decarbonization targets by 2040 (Pramer 2021). In addition to cities such as Paris and Hamburg (Antics et al. 2005; Büsche 2014; Richter 2021, 2022), the Ruhr area is planning to rely increasingly on heat from deep geothermal energy (Richter 2019). Utilization of karstified and locally dolomitizied and fractured carbonates of the Lower Carboniferous (Becker et al. 2014) and Middle to Upper Devonian (Balcewicz et al. 2020) for geothermal heat production in the Ruhr area are explored (Arndt et al. 2020; Oswald et al. 2021; geomecon GmbH 2022). Future exploration strategies may also incorporate the naturally fractured Upper Carboniferous sandstones as a potential target (rubitec GmbH 2003), but should also consider subsurface galleries from hard coal mining in the region (Bussmann et al. 2019; Bücken et al. 2022).

Since the rock matrix of these Upper Carboniferous sandstones is generally characterized by poor reservoir qualities (Wüstefeld et al. 2017; Becker et al. 2019a; Greve et al. 2023), permeability is primarily controlled by fractures (Busch et al. 2019). Kruszewski et al. (2021) analyzed discontinuities on dipmeter logs of wellbores located in the Ruhr basin, considering all discontinuities such as bedding and fractures. In contrast, this work uses dipmeter log filtering for near-vertical fractures, to exclude bedding planes and sedimentary structures. Additional filtering for only sandstone hosted fractures will be applied.

This study aims to characterize the attributes of the natural fracture network of Upper Carboniferous sandstones (Namurian C and Westphalian A) by using an integrated approach combining outcrop data (digitized 3D outcrop models from drone imagery) and wellbore data (dipmeter log, core description). Critical stressed fracture analysis is performed for fractures detected in a 1211.58 m TVD deep wellbore in order to identify potentially hydraulically conductive fractures under present day stress conditions. All these results will feed into a detailed fracture model of the Upper Carboniferous sandstone units, providing a data base for future discrete fracture network modelling as well as geothermal exploration and design of stimulation operations.

2.3 Geological Setting

The Ruhr Basin is part of the Variscan external fold and thrust belt and stretches over 150 km by 80 km (Drozdzewski 1993; Ziegler 1982; Drozdzewski et al. 2009). The Ruhr basin hosts the major German hard coal mining area, with the last mine dismantled in 2018 (Drozdzewski 1993; Meschede and Warr 2019).

Upper Carboniferous clastic sequences were deposited in the Subvariscan foreland retroarc basin north of the NW-migrating Variscan orogeny. Sedimentary rocks were deformed by the Variscan fold-and-thrust belt (Drozdzewski et al. 2009; Meschede and Warr 2019). The Upper Carboniferous sedimentary rock sequences reaches maximum thicknesses of over 4000 m in the Ruhr basin (Meschede and Warr 2019), with up to 3500 m of coal-bearing horizons (Schäfer 2019). Cyclically occurring sandstones, siltstones, shales and coal seams building up the Upper Carboniferous succession (Richter 1971; Hampson et al. 1999; Suess et al. 2007). Coal formation occurred from Namur C to Westphalian D (Bashkirian – Moscovian, 320 – 300 Ma) in a depositional environment that changed from marine deltas to alluvial plains (Schäfer 2019). The Upper Carboniferous is unconformably overlain by subhorizontal Cretaceous marine sediments. The thickness of the Cretaceous succession increases towards the NW with a maximum of 2000 m in the Münsterland region (Richter 1971; Drozdzewski 1993).

The Upper Carboniferous Variscan fold and thrust belt in the Ruhr basin hosts NW-verging folds and overall SE-dipping thrust planes (Drozdzewski 1993; Drozdzewski et al. 2009). The Carboniferous was later displaced into horst and graben structures by mainly NW-SE striking normal faults (Drozdzewski et al. 1980). Vertical fault displacements in the order of several 100 m can be observed with a maximum of up to 1000 m (Pilger 1956; Richter 1971; Drozdzewski et al. 1980).

WNW-ESE and N-S oriented strike-slip faults are additional features of the structural inventory of the Ruhr basin (Richter 1971; Drozdzewski et al. 1980; Hilden 1995). Normal faults are reported to have a maximum fault activity during the Triassic (Drozdzewski and Wrede 1994). After the extensional phase between the Permian and the Jurassic (Lohr et al. 2007), the Mid-Cretaceous inversion led to the reactivation of the normal and strike-slip faults (Wolansky 1950; Drozdzewski et al. 1980).

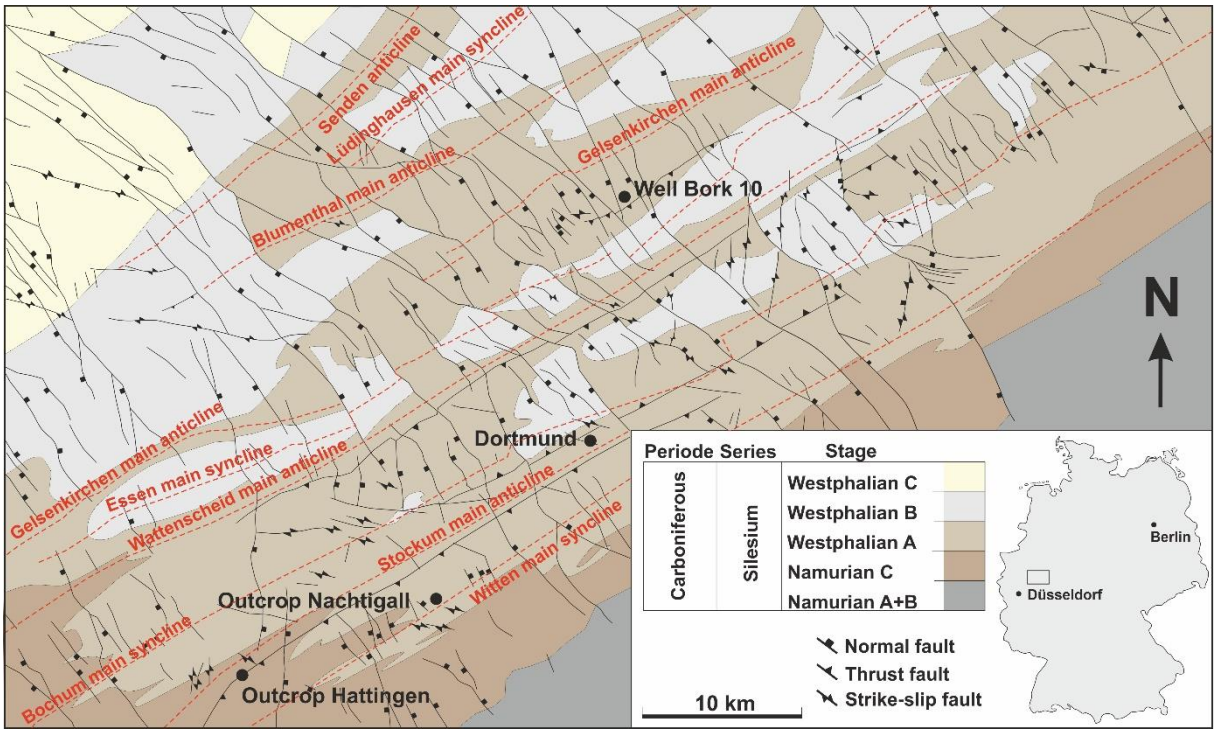

Figure 2.1: Geological map of the Ruhr basin in Germany representing the Top Carboniferous. Tectonic inventory comprises normal, thrust and strike-slip faults. Anticlines and synclines strike perpendicular to NW-SE oriented normal faults. The locations of the outcrop Nachtigall and Hattingen as well as the Bork 10 wellbore are highlighted (modified after Drozdzewski et al. 1982).

2.4 Methods

Fracture analysis was conducted on two digitized outcrops and subsurface data from one wellbore. Due to the high vegetation density within the Ruhr basin, there are only a few Upper Carboniferous outcrops, which additionally are suitable for fracture detection. The chosen outcrops are located in the southern part of the Ruhr Basin, as the Upper Carboniferous in the rest of the basin is unconformably overlain by the Cretaceous series (Richter 1971; Drozdzewski 1993). (i) The Kaisberg sandstone of the Kaisberg formation (Namurian C) exposed in Hattingen (WGS84: 51.379228, 7.141390) with the outcrop being located on the southeastern limb of the Stockum main anticline (Figure 2.1). (ii) The Finefrau sandstone of the Witten formation (Westphalian A) exposed at the site of the former coal mine Nachtigall (WGS84: 51.426775, 7.312662). Located within the Witten main syncline, the outcrop is part of the northwestern limb of the lower order Herbeder anticline (Figure 2.1).

The Bork 10 is a vertical coal exploration wellbore targeting the Upper Carboniferous, located on the south-eastern flank of the Gelsenkirchen main anticline (Figure 2.1). The wellbore, drilled in 1980, penetrates the Cretaceous strata before encountering the Upper Carboniferous at 575.55 m TVD. The Bork 10 wellbore reaches a final depth of 1211.58 m TVD with a deviation in the Upper Carboniferous of 38.13 m at an azimuth of 359°. The entire Upper Carboniferous drill section was cored and covers the Bochum and Witten Formations (Westphalian A). Bedding observed within the Bork 10 varies, with dip

angles ranging from 9 to 22.5° in depths shallower than 1155 m MD, before increasing to 22.5 – 27° for the deeper sections.

Digitized 3D outcrop models were created using a DJI Mavic 2 Enterprise as well as a DJI Phantom 4 Advanced to collect aerial images for point cloud generation using Agisoft PhotoScan (now MetaShape). During point cloud generation the desired quality was set to *very high* and the depth filtering was set to *mild*. Further point cloud processing following export from PhotoScan is done with CloudCompare for subsampling and manual fracture detection (Girardeau-Montaut 2017). Manual fracture detection is performed by fitting a plane on the exposed fracture surface using CloudCompare's compass tool. In this way, geometric attributes such as dip azimuth, dip angle as well as the exact spatial position are determined. The outcrop fracture networks are characterized with regard to their fracture geometry, orientation and frequency (Odling et al. 1999; Zhang et al. 2013; Lei et al. 2017). Orientation data is processed by using Stereonet 11 to subdivide the fractures into different sets. Each fracture set is described by a mean strike direction and average dip angle as well as associated standard deviations.

Fracture geometry is obtained in theory by measuring the length and height in dismantled outcrops (Priest 1993). Since reservoir analogs used in this study are only laterally exposed, fracture length must be derived from measuring fracture height and assuming a constant aspect ratio (height-to-length ratio) (Wüstefeld et al. 2018; Milad et al. 2018). Bed-boundedness is studied by distinguishing between unbounded, perfect bed-bounded, top- or base-bounded and confined fractures following Wang and Grammer (2019) (Figure 2.2). However, the assessment of bed boundedness is also affected by the position along a fracture in 3D, as cutting effects may not expose the centroid of the fracture. Topological information cannot be obtained due to the absence of lateral exposure of the reservoir analogs.

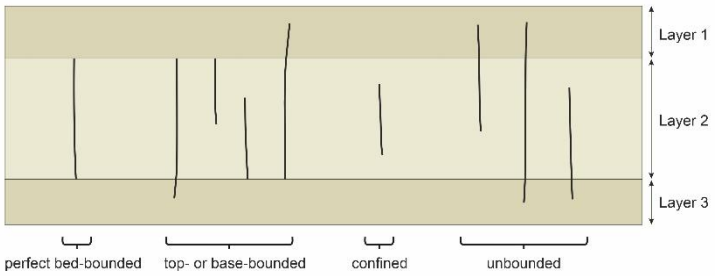

Figure 2.2: Relationship between near-vertical fractures and layer interfaces describes the bed boundedness type (modified after Wang and Grammer 2019).

Fracture intensity is derived for each set individually by following the P_{XY} scheme, where X represents the dimension of the sample and Y the measurement dimension (Dershowitz 1985; Dershowitz and Herda 1992). The linear fracture intensity (P_{10}) describes the number of fracture intersections per length unit along a scanline or wellbore. To account for the underrepresentation of scanline-parallel fractures, the Terzaghi correction is applied (Terzaghi 1965; Sanderson and Nixon 2015). Due to the alignment of both outcrops, it is not possible to place orthogonal scanlines in order to cover the full set of possible

fracture orientations. Therefore, one scanline is placed for each outcrop. In addition to outcrop studies, data of the Bork 10 wellbore were taken from core description and tadpole information from a dipmeter log. Since dipmeter logging measures structural and sedimentary features, it is challenging to distinguish only structural features during data interpretation (Rider and Kennedy 2011). The term fracture used for this study encompasses joints, veins and shear fractures representing faults with minor offset (Fossen 2010). In order to identify fractures in the set of dipmeter measurements, we searched for well-defined tadpole patterns. Within a section of constant shallow dipping bedding tadpoles, an abruptly steeply dipping feature is classified as a fracture. For this, following the approach of Samantray et al. (2010), only tadpoles with dip angles greater than 45° are considered. Dip tadpoles are available for a step width of 50 cm, leading to an underestimation of the fracture quantity. In addition, if fractures and bedding planes spatially coincide, the feature with the lower dip is automatically selected for the dip calculation, causing certain fractures to be missed out (Rider and Kennedy 2011) (Figure 2.3). In addition, a detailed description of approximately 600 m of oriented core material is available for wellbore Bork 10 providing a promising data base to study fractures and their properties. The core description does not provide any information on fracture types or aperture.

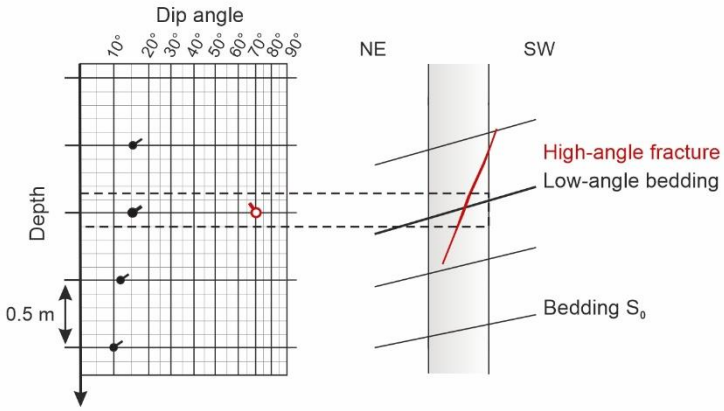

Figure 2.3: In case of spatially simultaneous occurrence of a low-angle (bedding) and a high-angle (fracture) structural feature, the dipmeter log will only detect the low-angle feature (based on description by Rider and Kennedy (2011)).

Fracture intensity (P_{10}) calculation for the Bork 10 wellbore fracture population was conducted in accordance to van der Voet et al. (2020). To avoid the large proportional errors of the Terzaghi correction factor for wellbore-parallel fracture configurations, angles greater than 80° between the vertical wellbore and the fracture normals are neglected (Wang and Mauldon 2006). No correction for the azimuthal sampling bias is applied for the vertical wellbore configuration following Barr (2007).

In order to identify fractures favorably aligned for reactivation in the present-day stress field, slip and dilation tendency values are used as proxies (Morris et al. 1996; Ferrill et al. 1999; Moeck et al. 2009; Becker et al. 2019b). Slip tendency can be utilized to identify potentially conductive fracture orientations at present-day stress conditions following the concept of critically stressed fractures. A critically stressed

fracture analysis (CSF analysis) is conducted to identify fractures with its ratio of shear (τ) to effective normal stress (σ_n) exceeding the frictional strength of the fracture (μ) (1). These fractures are considered as critically stressed and therefore to be mechanically active, having an increased likelihood to be hydraulically conductive (Barton et al. 1995; Zoback and Kohli 2019). The slip tendency T_S gives the likelihood for a fracture to be reactivated in shear mode assuming no cohesion (Morris et al. 1996):

$$T_s = \frac{\tau}{\sigma_n} \geq \mu \tag{1}$$

The likelihood of a plane to open (to dilate) in tensile mode is given by the dilation tendency T_D defined by following equation (2) (Ferrill et al. 1999):

$$T_d = \frac{(\sigma_1 - \sigma_n)}{(\sigma_1 - \sigma_3)} \tag{2}$$

Where σ_1 is the maximum principal stress, σ_3 is the minimum principal stress and σ_n is the resolved normal stress (Ferrill et al. 1999).

Slip tendency versus dilation tendency patterns are useful proxies to assess fracture behavior under present-day stress conditions (Ferrill et al. 2020a). Reactivation in shear mode is generally linked to high slip tendency and moderate to high dilation tendency (Ferrill et al. 2020a). Shear slip on pre-existing fractures can cause permanent permeability enhancement, since the misalignment of the fracture walls can lead to a sort of self-propped fracture (Zoback and Kohli 2019; Zimmermann et al. 2019; Cheng and Milsch 2021).

Published stress data are taken from Kruszewski et al. (2021), since no stress measurements were available for the Bork 10 wellbore. Based on re-evaluation of published data and results from several wells drilled in the Ruhr basin, Kruszewski et al. (2021) determined following linearized stress gradients: i) a maximum horizontal stress gradient (S_{Hmax}) of 33.6 ± 9.6 MPa km^{-1}, ii) a vertical stress gradient (S_V) of 23.1 ± 1.3 MPa km^{-1} and iii) a minimum horizontal stress gradient (S_{hmin}) of 16.1 ± 4.3 MPa km^{-1}. The pore pressure gradient accounts for 10.8 ± 1.0 MPa km^{-1} (Kruszewski et al. 2021). Kruszewski et al. (2021) observed a transition from a transpressional to a strike-slip faulting regime within 600 to 1000 m depth, with data suggest a strike-slip regime present up to a depth level of around 2000 m. The stress state of the Ruhr basin is generally derived from stress measurements conducted in coal exploration wells, which typically do not exceed depths of more than 1500 m, limited by the depth of interests

for hard coal mining. Hence, depth-dependent changes of the stress field are not determined for depth levels below approximately 2000 m.

Today's maximum horizontal stress orientation is taken from Niederhuber et al. (2023a) given as S_{Hmax} = 154° ± 33°. To account for the relatively high standard deviation of 33°, three orientation scenarios are calculated to cover the possible S_{Hmax} orientation range: scenario 1 (S_{Hmax} = 154°), scenario 2 (S_{Hmax} = 121°) and scenario 3 (S_{Hmax} = 187°).

Slip tendency analysis often assuming a coefficient of friction of μ = 0.6 (Worum et al. 2004; Becker et al. 2019b; Kinoshita et al. 2019; Ferrill et al. 2020b) following Byerlee (1978). Since detected fractures are hosted in Upper Carboniferous sandstone units, a coefficient of friction (μ) of 0.67 for fractured Ruhr sandstone is used (Kruszewski et al. 2021).

2.5 Results

2.5.1 Upper Carboniferous sandstones

The Kaisberg sandstone unit (Namurian C) in Hattingen is exposed in NNE-SSW direction over a length of approximately 60 m and a vertical extend of 17 m (Figure 2.4a). The exposed sandstone unit is dipping towards ESE (117°) with 31°, representing the base of the coal-bearing Upper Carboniferous. Sandstone layers up to 7.2 m thick are building up the fluvio-deltaic sandstone unit.

The outcrop exposing the Finefrau sandstone of the Witten formation (Westphalian A) is oriented in W-E direction with a horizontal extent of approximately 100 m (Figure 2.4b). The bedding dips towards NNW (331°) at a dip angle of approximately 12°. The fluvio-deltaic Finefrau sandstone is up to 7 m thick and characterized by its channel architecture with interbedded fine-grained material.

Thickness comparison of the Finefrau sandstone (Westphalian A) exposed in the outcrop as well as drilled by the Bork 10 wellbore indicates lateral thickness variations across the Ruhr basin. While the sandstone unit exposed in the outcrop is at least 7.2 m thick, the Finefrau sandstone drilled in the Bork 10 wellbore at 1029.25 m TVD decreases towards 1.3 m. Analysis of the 638.10 m of Westphalian A strata (Bochum and Witten Formation) drilled by the Bork 10 wellbore revealed a net-to-gross ratio of 33 % with 210.33 m of sandstone.

2.5.2 Fracture network characterization

2.5.2.1 Outcrops

Orientations derived from scanline fracture detection performed on the digital outcrop model for the Kaisberg sandstone (138 fractures) (Figure 2.4a) can be divided into three main sets. Set 1 strikes NNE-SSW to NE-SW (Figure 2.5a, b) (n = 39 fractures, mean strike of 35° ± 17°) at a mean dip angle of 70° ± 13° (Table 2.1). The fracture set 1 represents 28 % of the entire fracture population. Fracture set 2 trends WNW-ESE (Figure 2.5a, b) (n = 63 fractures, mean strike of 114° ± 10°) at a mean dip angle

of 82° ± 6° (Table 2.1). Fracture set 2 is the largest set, accounting for 46 % of the detected fracture population. Fracture set 3 strikes NNW-SSE to N-S (Figure 2.5a, b) (n = 36 fractures, mean strike of 168° ± 13°) at a mean dip angle of 78° ± 10°, representing 26 % of the fracture population (Table 2.1).

Table 2.1: Summarized orientation statistics of the fracture detection run on the Kaisberg sandstone exposed in Hattingen.

Data set		n	%	Mean strike [°]	Stdev. [°]	Mean dip [°]	Stdev. [°]
Hattingen, Kaisberg sandstone	Set 1	39	28	35	17	70	13
	Set 2	63	46	114	10	82	6
	Set 3	36	26	168	13	78	10

The mean fracture height accounting for all detected fractures is 2.09 m, with mean heights per fracture set of 1.71 m, 2.45 m and 1.91 m for set 1 to 3 respectively (Figure 2.5 c – f). Fracture height is controlled by the thickness of the sandstone layer ranging from 3.4 up to 7.2 m. The maximum fracture heights per set never exceed 9 m with maximum values of 6.2 m (set 1), 9 m (set 2) and 6.1 m (set 3) (Figure 2.5c - f).

Bed boundedness investigations for the scanline derived fractures indicate 73 % of the detected fracture population to be of confined character (Figure 2.6). Approximately 20 % are bounded at the top or base by bedding interfaces (Figure 2.6). Perfect bed-bounded (1 %) and unbounded fractures (5 %) are only rarely observed. No significant differences in the bed boundedness type between all three fracture sets is observed (Figure 2.6).

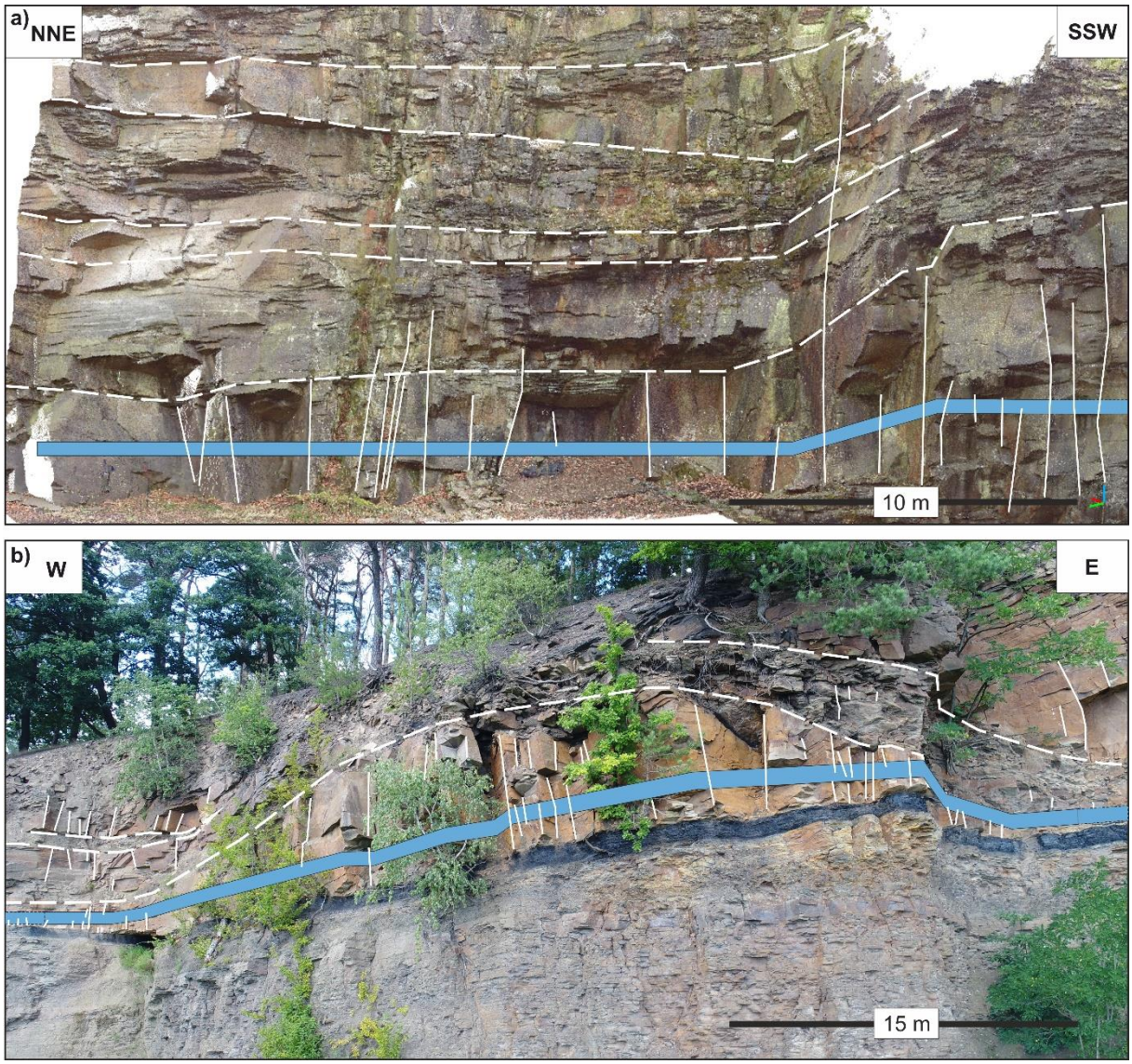

Figure 2.4: a) Section of the 3D model of the Hattingen outcrop (Kaisberg sandstone, Namurian C). The NNE-SSW trending scanline was placed in the lower part of the outcrop. White fracture traces demonstrate their vertical extend and do not represent the actual picked fracture surfaces. Also the quantity of detected fractures cannot be deduced from the shown fracture traces. b) The Finefrau sandstone (Westphalian A), exposed in the Nachtigall outcrop, is build up by fluvial channels. The vertical fracture extend is indicated by white traces, which do not represent the detected fracture data set. Dashed line – bedding, blue line – scanline.

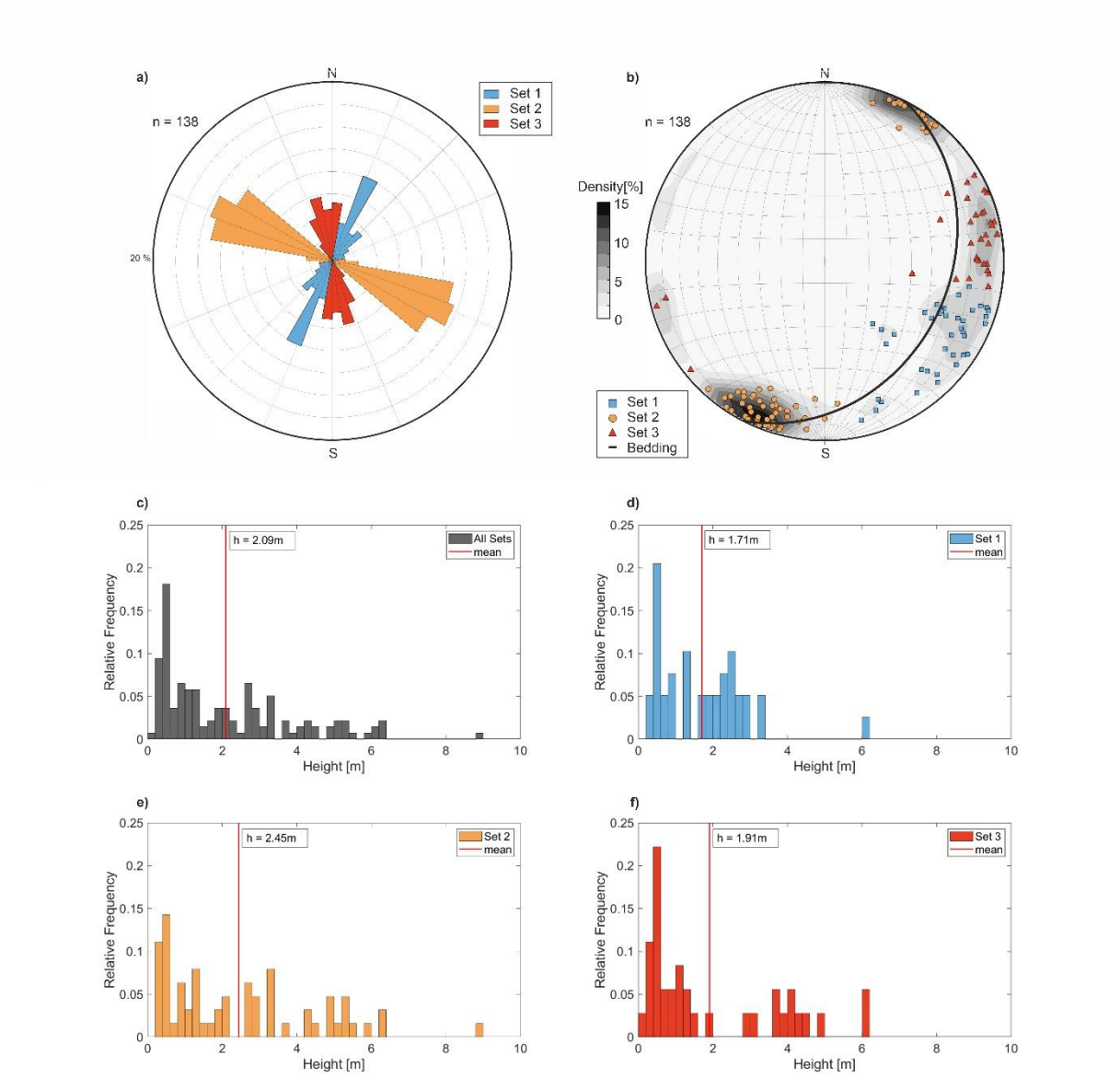

Figure 2.5: a) Scanline detection conducted for the Kaisberg sandstone (Namurian C, outrop Hattingen) revealed 138 fractures subdivided into sets based on strike orientation. Data presented on a rose diagram showing three major fracture sets. b) Stereographic projection on a Schmidt net (lower hemisphere) comprising fracture poles and outcrop bedding S_0 (117/31). c) Fracture height distribution accounting for all detected fractures at the outcrop. Data presented using 0.2 m bin width. d) Fracture height distribution of set 1 showing a mean height of 1.71m. e) Largest mean height is observed for set 2. f) Fracture set 3 is characterized by a mean height of 1.91 m.

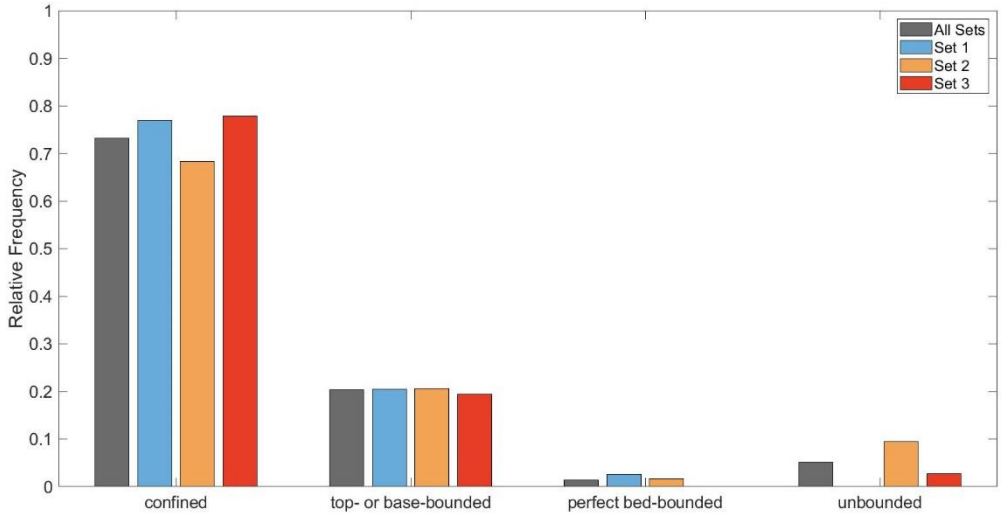

Figure 2.6: Confined fractures dominate within the placed scanline at the Kaisberg sandstone outcrop (Namurian C). No clear differences in bed boundedness are observed between all three fracture sets.

Fracture detection of the Finefrau sandstone (Westphalian A) (Figure 2.4b) revealed 151 fractures, which can be subdivided into three sets (Figure 2.7a). Fracture set 1 strikes NE-SW (Figure 2.7a, b) (n = 43 fractures, mean strike of 40° ± 11°) at a mean dip angle of 74° ± 9°, representing 28 % of the entire fracture population (Table 2.2). Fracture set 2 strikes WNW-ESE (Figure 2.7a, b) (n = 76, mean strike of 113° ± 16°) with a distinct additional NW-SE trend, making up 50 % of the detected fracture population. The observed mean dip angle is 81° ± 6° (Table 2.2). The N-S trending fracture set 3 (Figure 2.7a, b) is described by a mean dip angle of 81° ± 7° (n = 32 fractures, mean strike of 180° ± 11°) (Table 2.2). Fracture set 3 represents 21 % of the Finefrau sandstone outcrop fracture population.

Table 2.2: Orientation statistics of the fracture network detected within the exposed Finefrau sandstone at the outcrop Nachtigall.

Data set		n	%	Mean strike [°]	Stdev. [°]	Mean dip [°]	Stdev. [°]
Nachtigall, Finefrau sandstone	Set 1	43	28	40	11	74	9
	Set 2	76	50	113	16	81	6
	Set 3	32	21	180	11	81	7

Fracture height measurements show a mean height of 0.95 m for all detected fractures (Figure 2.7c). Set 1 is characterized by a mean height of 0.86 m with a maximum value of 3.4 m (Figure 2.7d). The largest fractures are observed within fracture set 2 with a maximum of 3.7 m and a mean of 1.03 m

(Figure 2.7e). The mean height of fracture set 3 is 0.88 m with a maximum of 2.5 m (Figure 2.7d). Variation in fracture height of strata-bound fractures is partially controlled by the sedimentary architecture of the fluvial channels building up the Finefrau sandstone (Figure 2.4b). Generally, larger fractures are observed in the thickest central part of the several channels building up the Finefrau sandstone in the Nachtigall outcrop.

Accounting for the Finefrau sandstones fracture networks relation to bed interfaces, 49 % of the detected fractures are of confined character (Figure 2.8). Top- or base-bounded fractures account for 30 % with 17 % being perfectly bed-bounded (Figure 2.8). Roughly 4 % of the fractures are unbounded. Differences in the bed boundedness type between the three fracture sets are observed for perfect bed-bounded endmember types, with fracture set 3 being approximately 10 % higher compared to fracture set 2 and 3 (Figure 2.8).

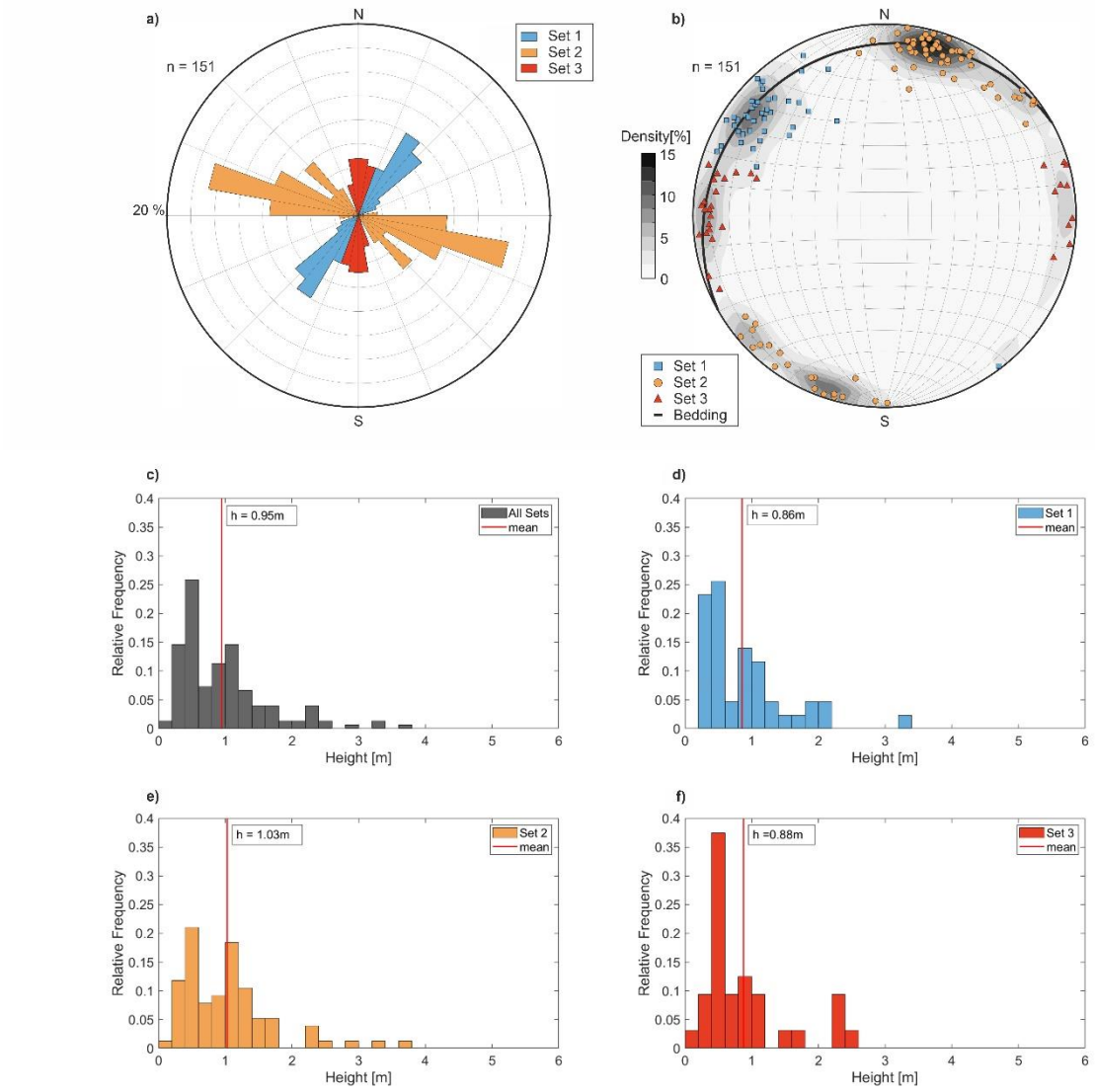

Figure 2.7: a) Scanline detection of the Finefrau sandstone (Westphalian A, outcrop Nachtigall) resulted in 151 detected fractures, subdivided into fracture sets. Fracture strike orientation shows three major fracture sets, highlighted by blue, red and orange colors. b) Fracture poles and outcrop bedding plotted on a Schmidt net. c) Fracture height distribution for the outcrop Nachtigall presented using a bin width of 0.2 m. Measured mean height accounting for all detected fractures is 0.95 m. d) Fracture set 1 is characterized by a mean height of 0.86 m and a maximum of 3.4 m. e) Fracture height distribution for fracture set 2 showing a mean height of 1.03 m. f) Mean fracture height of fracture set 3 is 0.88 m.

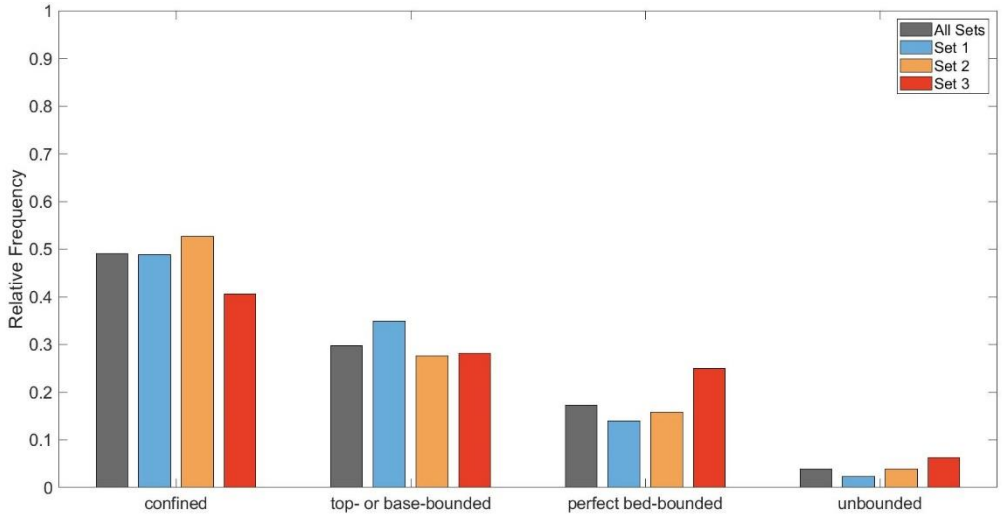

Figure 2.8: Bed boundedness of all detected fractures of the the Finefrau sandstone (Westphalian A). Confined and top- or base-bounded fractures are dominant.

Measured average fracture density (P_{10}) along the scanlines indicates differences between the three fracture sets within both outcrops. Average fracture densities (P_{10}) vary dependent on the fracture set orientation. Accounting for the Kaisberg sandstone (Namurian C), fracture set 1 exhibits the highest Terzaghi corrected fracture density with $P_{10} = 2.02\ m^{-1}$ (uncorrected $P_{10} = 0.67\ m^{-1}$). Terzaghi corrected densities for fracture set 2 and 3 are $P_{10} = 1.21\ m^{-1}$ (uncorrected $P_{10} = 1.08\ m^{-1}$) and $P_{10} = 0.73\ m^{-1}$ (uncorrected $P_{10} = 0.62\ m^{-1}$), respectively.

Highest average fracture density for the Finefrau sandstone (Westphalian A) is observed for fracture set 2 with Terzaghi corrected $P_{10} = 3.12\ m^{-1}$ (uncorrected $P_{10} = 0.90\ m^{-1}$). The fracture sets 1 and 3 exhibit generally lower Terzaghi corrected average fracture densities with $P_{10} = 0.58\ m^{-1}$ (uncorrected $P_{10} = 0.51\ m^{-1}$) and $P_{10} = 0.40\ m^{-1}$ (uncorrected $P_{10} = 0.38\ m^{-1}$).

2.5.2.2 Bork 10 wellbore

Dipmeter log interpretation revealed 62 fractures hosted in Upper Carboniferous sandstone units of the Westphalian A (Figure 2.9a, b). The derived fracture orientation statistics show a dominant N-S to NW-SE striking fracture set (Figure 2.9a, b). While the WSW-ENE strike direction is distinctively pronounced, a NE-SW set is only subordinately developed (Figure 2.9a, b). A comparison of the fracture orientation statistics between the detected subsurface fracture network from dipmeter log interpretation

(n = 62) vs. core description (n = 119) indicates differences. The core description derived fracture population shows a dominant W-E fracture set alongside N-S striking fractures and only subordinately developed NW-SE as well as NNE-SSW trending fractures (Figure 2.9c, d).

The dominant N-S striking (± 20°) fracture set (n = 29) is characterized by a mean strike of 179° ± 9° and a mean dip angle of 66° ± 8° (Table 2.3). The N-S striking set accounts for 24% of the entire fracture population. The W-E striking (± 20°) fracture set is made up of 64 fractures representing 54 % of the Bork 10's fracture population, described by a mean strike of 91° ± 5° and a mean dip angle of 60° ± 11° (Table 2.3). The weakly developed NNE-SSW trending fracture set (n = 11) corresponds to 9 % of the entire fracture population. It is characzterized by a mean strike of 36° ± 14° and a mean dip angle of 56° ± 13° (Table 2.3). With representing 13 % of the Bork 10's fracture population, the NW-SE fracture set (n = 15) is also only weakly developed. This fracture set shows a mean strike of 140° ± 13° and a mean dip angle of 58° ± 13° (Table 2.3).

Table 2.3: Fracture set orientation statistics for fractures detected via core description of the Bork 10 wellbore.

Data set		**n**	**%**	**Mean strike [°]**	**Stdev. [°]**	**Mean dip [°]**	**Stdev. [°]**
Bork 10 wellbore	N-S set	29	24	179	9	66	8
	NNE-SSW set	11	9	36	14	56	13
	W-E set	64	54	91	5	60	11
	NE-SE set	15	13	140	13	58	13

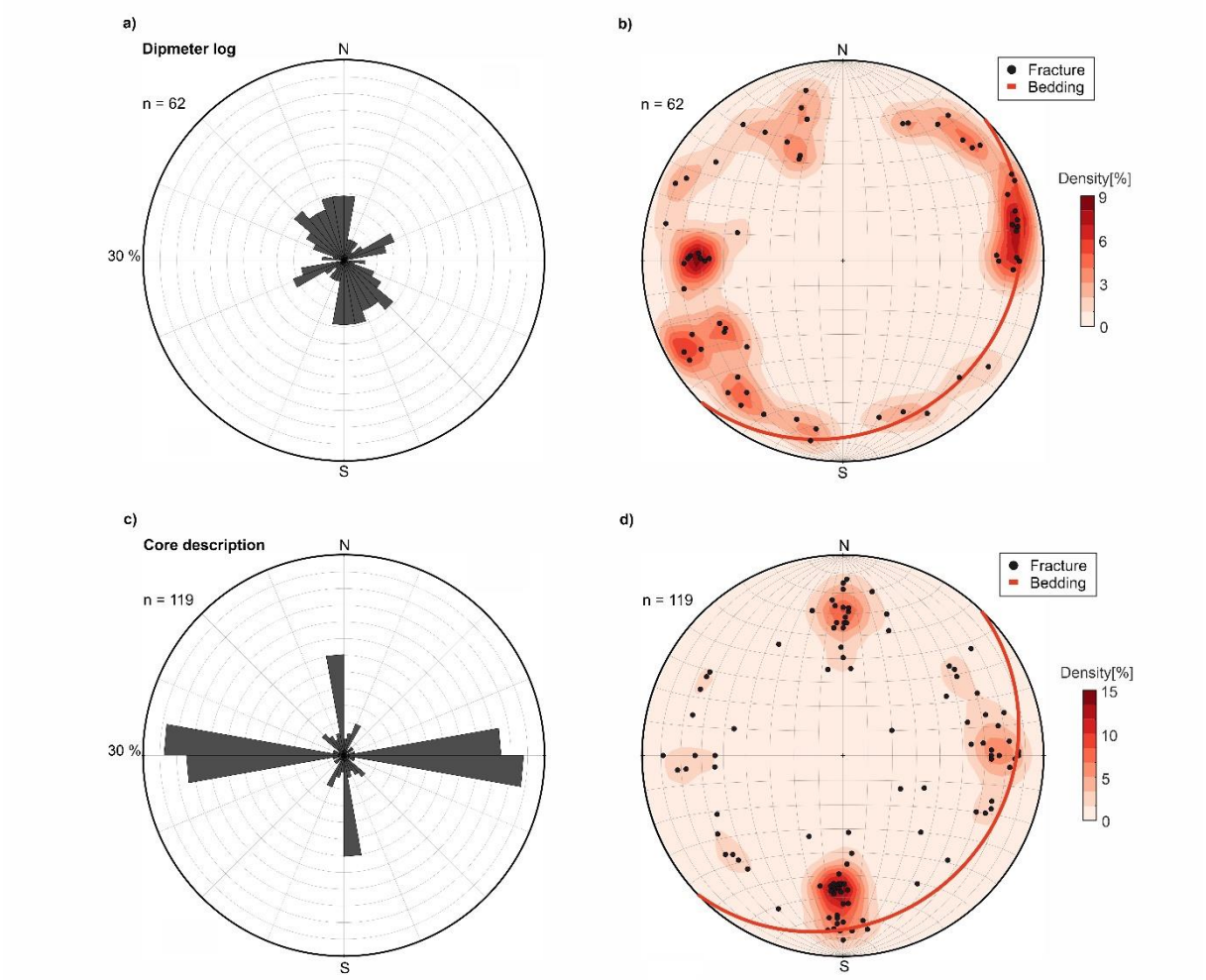

Figure 2.9: a) The dipmeter log interpretation revealed 62 fractures. Data plotted in 10° classes on a rose diagram indicating fracture strike orientation. b) Poles of dipmeter log derived fractures plotted on a Schmidt net. c) Core description analysis of the Bork 10 wellbore revealed 119 fractures with dominant N-S and W-E strike orientations. d) Fracture poles and average bedding (135/18) plotted on a Schmidt net

Dipmeter log derived fractures match core description derived fractures in depth location (± 6 m) and dip azimuth (± 25°) in 7 cases. This corresponds to a match of 11 %, while the remaining 89 % of the fractures from the dipmeter log interpretation fall outside this matching range (Figure 2.10a). In addition, the quantity of detected fractures is significantly lower in the case of the dipmeter log interpretation (n = 62) compared to the number of fractures from core description (n = 119). The depth distribution of core derived fractures show differences, with most of the reported fractures being located within the depth interval from 650 m to approximately 1025 m (Figure 2.10, a). Below that depth, the core description becomes incomplete and sandstone units drilled by the Bork 10 wellbore generally decrease in thickness and frequency.

Fracture intensity (P_{10}) along the wellbore is calculated for the two dominant N-S (± 20°) (n = 29 fractures, mean strike of 179°) and W-E (± 20°) (n = 64 fractures, mean strike of 91°) trending sets, taking only fractures hosted in sandstones into account. P_{10} varies with depth with the highest intensity observed for the W-E set at a depth interval from 794 to 831 m MD, where a maximum of 4 m^{-1} is reached

(Figure 2.10c). Fracture densities of the N-S set is in the range of 0 to 3 m^{-1} (Figure 2.10b). Terzaghi corrected fracture intensities P_{10} show generally higher values in the range of 0 to 9.1 m^{-1} (N-S set) and 0 to 8.8 m^{-1} (W-E set) (Figure 2.10d, e). Fracture intensity (P_{10}) averaged over the total thickness of Upper Carboniferous sandstone units (210.33 m) amounts to 0.14 m^{-1} (N-S set) and 0.30 m^{-1} (W-E set) respectively after Terzaghi correction to 0.38 m^{-1} (N-S set) and 0.70 m^{-1} (W-E set).

Fracture intensity data could not be derived for the Finefrau sandstone drilled at 1095 m MD, respectively 1029.25 m TVD. No fractures are reported in core material for the approximately 1.3 m thick sandstone, with dipmeter log interpretations only hosted in the silt- and claystones above and below the Finefrau sandstone.

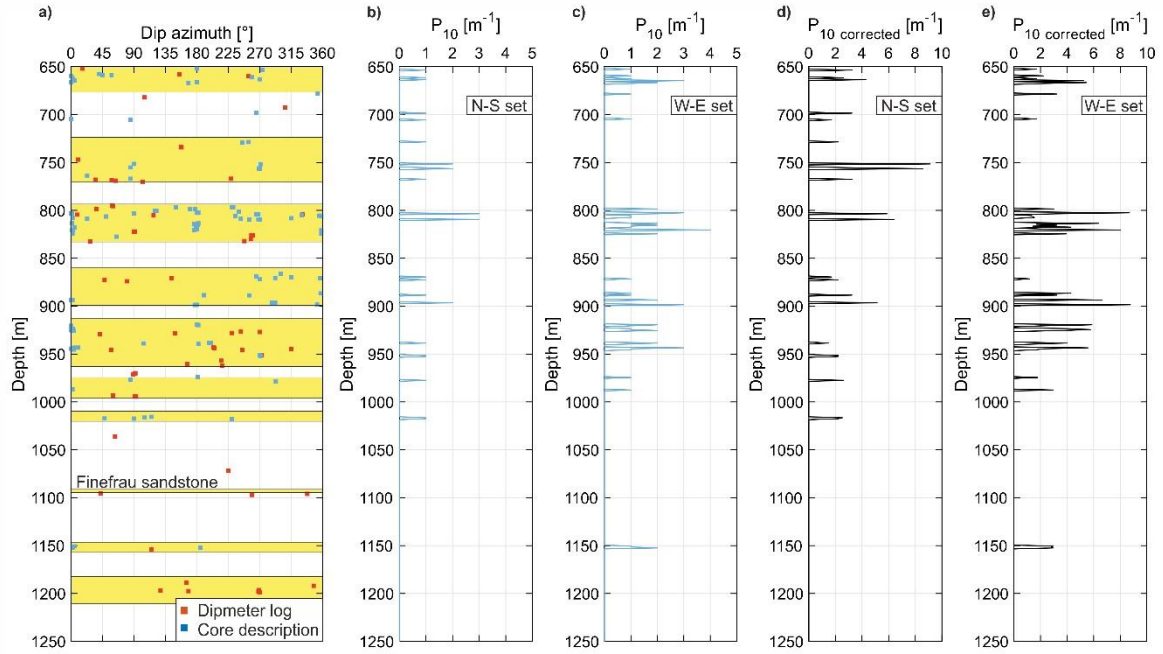

Figure 2.10: a) Comparison of detected fractures from dipmeter log and core description show a poor match regarding depth location and dip azimuth. The zones marked in yellow refer to sections composed mostly to exclusively of sandstone, while low thickness sandstone layers are neglected in this figure. b) Fracture intensity (P_{10}) along the cored wellbore section for the N-S set reaches a maximum of 3 m^{-1}. c) P_{10} representing the W-E fracture set varies with depth. d) Terzaghi corrected fracture intensity (N-S set) reaches a maximum of 9.1 m^{-1}. e) Highest Terzaghi corrected P_{10} observed at 8.8 m^{-1} for the W-E set.

2.5.3 Geomechanical fracture analysis

The critically stressed fracture (CSF) analysis was performed for fractures detected in the Bork 10 wellbore, hosted in Upper Carboniferous sandstone units. While fractures were detected within a depth ranging from 650 m to 1278 m MD, the stress magnitudes considered for the CSF analysis correspond to a depth of 1000 m.

Scenario 1

The slip tendency calculated for scenario 1 (S_{Hmax} = 154°) is highly variable, with values ranging from T_{Smin} = 0.22 to T_{Smax} = 0.77 (Figure 2.11d, e). Higher slip tendencies are associated with fractures oriented at an angle of approximately 30° to S_{Hmax} (154°) and subjected to higher shear stresses (Figure 2.11b). Critically stressed fracture analysis identified 10 % (n = 12) of the detected fractures (n = 119) to be critically stressed with slip tendencies exceeding the coefficient of friction $\mu = 0.67$ (Figure 2.11a, Figure 2.14a). N-S as well as NW-SE striking fractures exhibit highest slip tendencies, partially being critically stressed. These strike directions are likely to be mechanically active and therefore hydraulically conductive.

Fractures striking perpendicular to S_{Hmax} are characterized by low dilatation tendencies. 31 % (n = 37) of the detected fractures (n = 119) exhibit high dilation tendencies with T_D exceeding 0.7. Only 3 % (n = 4) of the fractures are subject to highest dilation tendencies of $T_D > 0.9$ (Figure 2.11d).

The combination of slip and dilation tendency results highlights following: (i) W-E to WSW-ENE striking fractures (green to turquoise points, Figure 2.11d) exhibit low to moderate slip and dilation tendencies, making them unfavorably oriented for reactivation in the contemporary tectonic stress field. An increase in dip angle for W-E trending fractures results in lower dilation tendencies (Figure 2.11e). (ii) WNW- ESE and NNE-SSW to NE-SW striking fractures (yellow and blue points, Figure 2.11d) are subject to moderate to high slip tendencies and moderate dilation tendencies. (iii) N-S, NNW-SSE to NW-SE trending fractures exhibit medium to high slip tendencies combined with high dilation tendencies (dark blue and orange to red points, Figure 2.11d). NNW-SSE striking fractures exhibit the highest dilation tendencies since being oriented approximately parallel to S_{Hmax}, while experiencing only moderate slip tendencies.

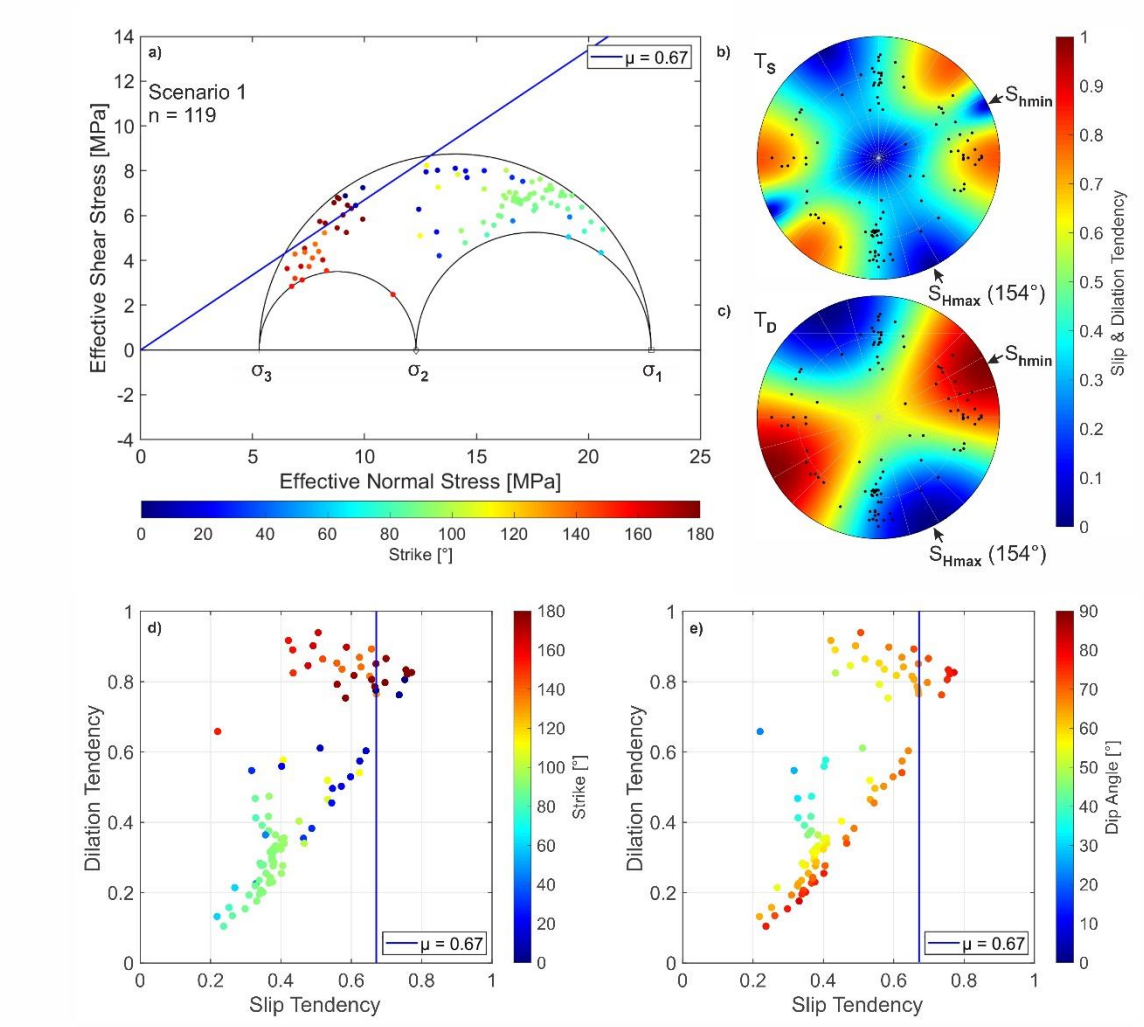

Figure 2.11: a) Critically stressed fracture analysis conducted for fractures hosted in sandstone detected in the Bork 10. Fractures with shear to effective normal stress ratios exceeding 0.67 plot above the failure envelope ($\mu = 0.67$) and are considered to be critically stressed. The colour code denotes the strike of the fractures in the Bork 10 wellbore. b) Slip tendency as color code indicating fracture poles exceeding $T_S = 0.67$ to be in a critically stressed state, plotted as poles in lower hemisphere stereographic projections. c) Dilation tendencies for the detected fractures of the Bork 10 displayed in stereographic projection identifying NNE-SSW trending fractures to be associated with highest dilation tendencies. d) Slip versus dilation tendency plot with associated strike orientation highlights N-S striking fractures to experience high T_D while being partially critically stressed. e) Influence of the dip angle on T_S versus T_D pattern depends on strike direction.

Scenario 2

Scenario 2 accounts for the lower bound of possible S_{Hmax}-directions (S_{Hmax} = 121°) with slip tendencies ranging from T_{Smin} = 0.18 to T_{Smax} = 0.76. CSF analysis revealed 16.8 % of the fractures to be critically stressed with slip tendencies exceeding the coefficient of friction (Figure 2.12a).

Maximum dilation tendencies for scenario 2 are associated with WNW-ESE to NW-SE strike directions (Figure 2.12c). Values show a range from T_{Dmin} = 0.09 to T_{Dmax} = 0.94 with 44 % (n = 52) of the fractures exceeding T_D = 0.7, respectively 0.8 % (n = 1) exceeding T_D = 0.9 (Figure 2.12c).

Analysis of slip versus dilation tendency results highlights, that (i) N-S to WSW-ENE striking fractures exhibit low to moderate slip and dilation tendencies (dark blue to light blue and dark red points, Figure 2.12d), with the combination of the lowest slip and dilation tendencies observed for the NNE-SSW strike direction. (ii) NW-SE to NNW-SSE as well as W-E to WNW-ESE striking fractures are subject to highest slip tendencies, partially exceeding TS = 0.67 (orange to light red and green to yellow, Figure 2.12d). Highest dilation tendencies are linked to WNW- ESE trending fractures. The dip angle controls the slip tendency for W-E and NW-SE striking fractures, with steeply dipping ones experience higher slip tendencies (Figure 2.12d and e).

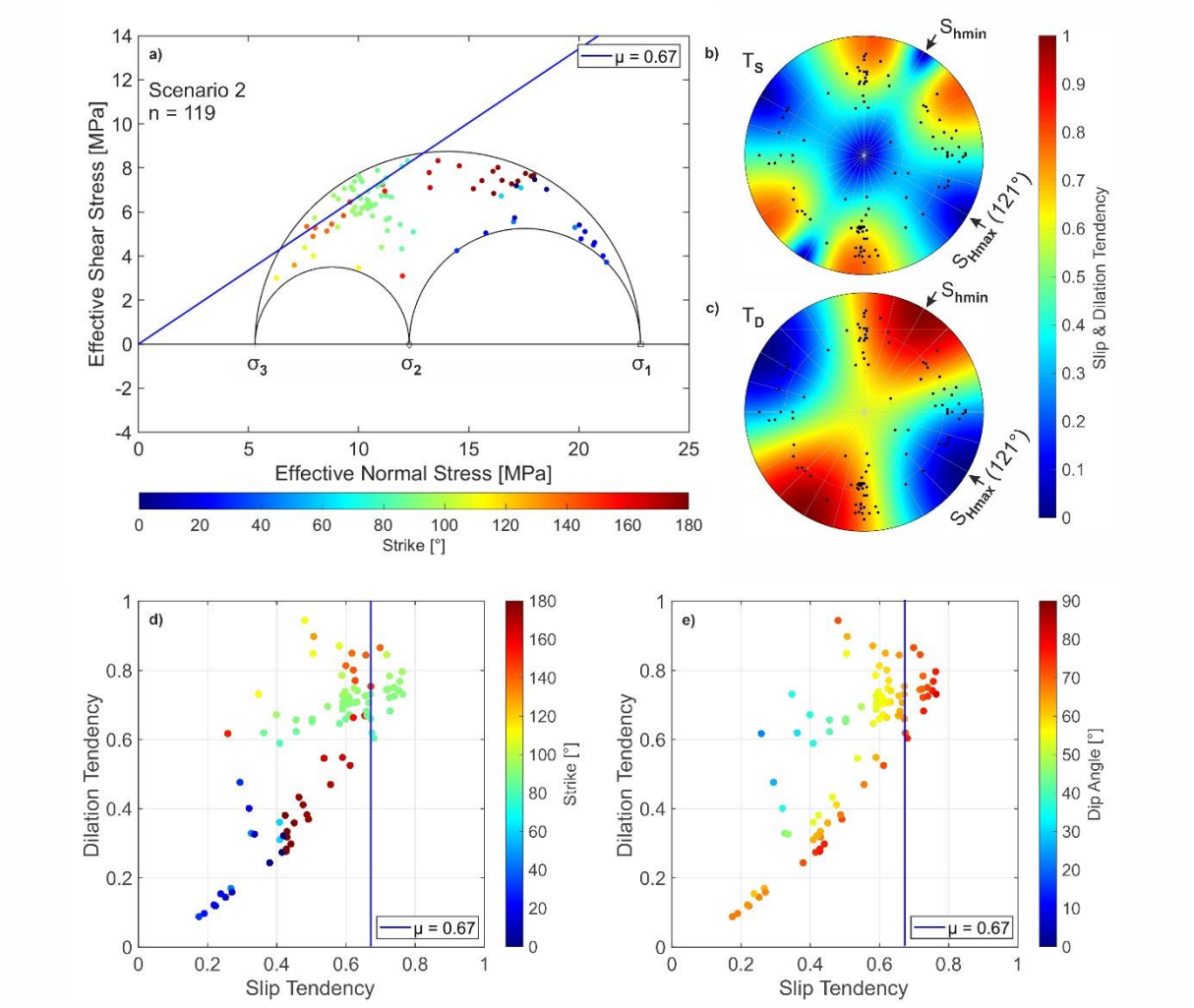

Figure 2.12: a) CSF analysis for scenario 2 indicates W-E and NNW-SSE striking fractures to be partially critically stressed. b) Stereo diagram for scenario 2 with 16.8 % of the detected fractures to be critically stressed. c) WNW-ESE to NW-SE strike direction is associated with highest dilation tendencies. d) TS-TD pattern highlight W-E and NNW-SSE strike direction to be associated with medium to high dilation tendencies. e) Dip angle controls TS-TD pattern in dependency of the strike orientation.

Scenario 3

With scenario 3 defined by the upper bound of possible S_{Hmax} orientations (S_{Hmax} = 187°), slip tendencies fall into a range from T_{Smin} = 0.11 to T_{Smax} = 0.72. With only 2.5 % of the detected fractures being critically stressed, NNW-SSE and NE-SW to NNE-SSW striking fractures exhibit the highest slip tendencies (Figure 2.13b).

N-S striking fractures experience the highest dilation tendencies under scenario 3 stress conditions (Figure 2.13c). Calculated dilation tendencies show a spread from T_{Dmin} = 0.03 to T_{Dmax} = 0.97 with 29.4 % (n = 35) of the fractures having dilation tendency exceeding T_D = 0.7, respectively 14.3 % (n = 17) exceeding T_D = 0.9.

Slip versus dilation tendency analysis reveal, that (i) W-E to WNW-ESE striking fractures are characterized by low to moderate slip and dilation tendencies (green to yellow points, Figure 2.13d), whereby the lowest slip and dilation tendencies are observed for near-vertical W-E trending fractures (Figure 2.13d, e). (ii) NE-SW to WSW-ENE and NW-SE striking fractures exhibit moderate to high slip tendencies in combination with moderate dilation tendencies (medium blue to light blue and medium red to light red points, Figure 2.13d). Shallowly dipping fractures generally show lower slip tendencies (Figure 2.13e). (iii) NNW-SSE over N-S to NNE-SSW striking fractures are subject to moderate to high slip tendencies along with high dilation tendencies (dark red and dark blue points, Figure 2.13d). NNW-SSE and NNE-SSW striking fractures are characterized by the highest slip tendencies combined with moderate dilatation tendencies. N-S striking fractures show moderate slip tendencies but highest dilatation tendencies (Figure 2.13d). An increase in dip angle comes along with higher dilation tendencies for N-S trending fractures (Figure 2.13e).

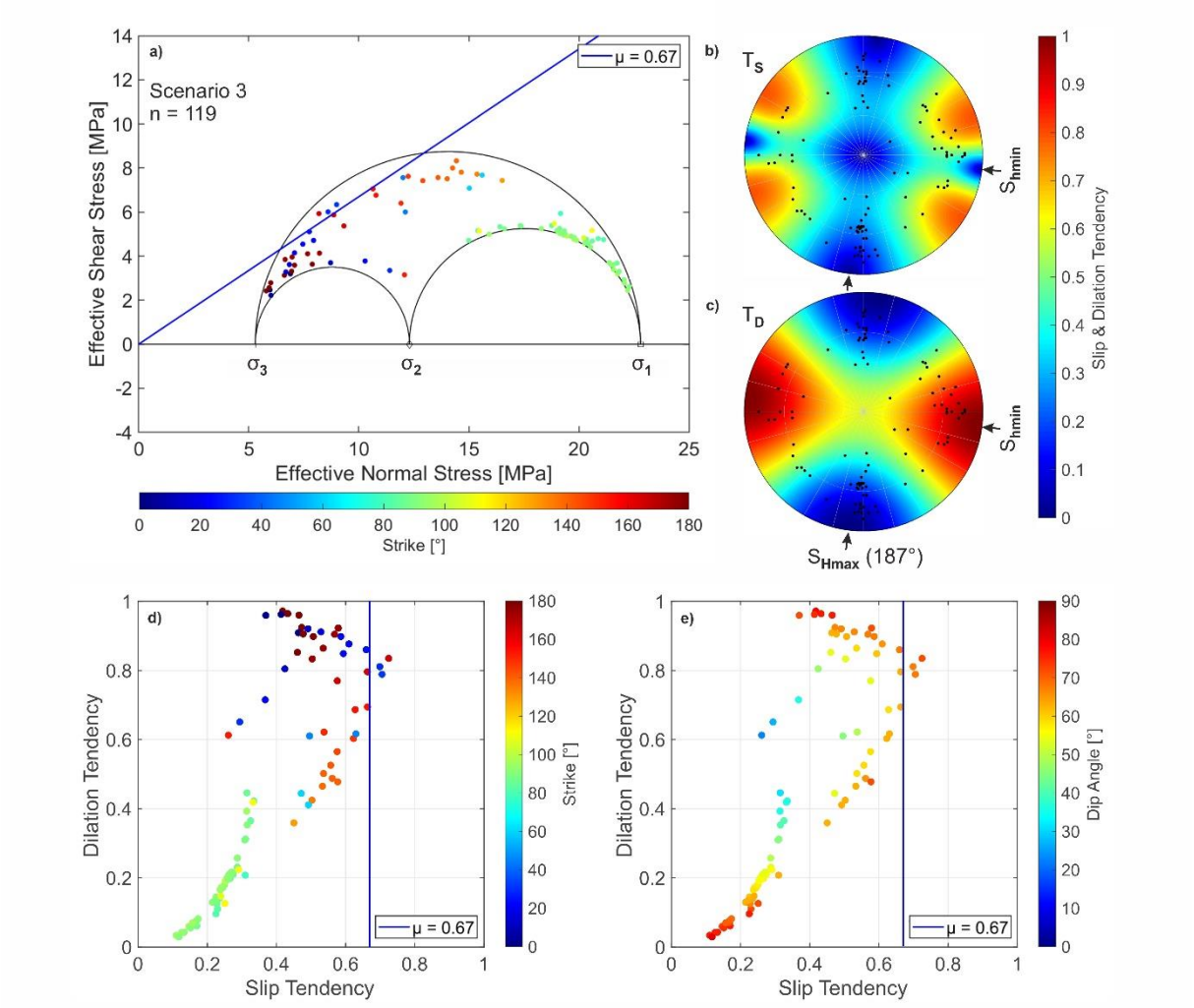

Figure 2.13: a) CSF analysis revealed only 2.5 % of the detected fractures to be in a critically stressed state. b) Assuming scenario 3 S_{Hmax}-direction, NNW-SSE and NE-SW to NNE-SSW strike direction is subject to highest slip tendencies. c) Fractures perpendicular to S_{Hmax} exhibit highest dilation tendencies d) T_S-T_D pattern reveals medium to high dilation tendencies for critically stressed fractures. e) Influence of dip angle on T_S and T_D is controlled by the strike orientation.

2.6 Discussion

2.6.1 Fracture orientations

Valuable information on the suitability of outcrops as reservoir analogs can be derived from outcrop-to-wellbore comparisons of fracture orientation statistics (Becker et al. 2018). Fracture set 1 matches for the Kaisberg (mean strike of 35° ± 17°) and Finefrau sandstone (mean strike 40° ± 11°) and is additionally present as weakly developed NNE-SSW striking fractures in the Bork 10 data set (mean strike of 36° ± 14°) (Table 2.4). Fracture set 2 shows comparable orientation statistics for the Kaisberg (mean strike 114° ± 10°) and Finefrau sandstone (mean strike 113° ± 16°) and can be compared with the W-E striking fractures (mean strike 91° ± 5°) of the Bork 10 wellbore, assuming an angular core measurement error of 25° (Table 2.4). Therefore, also the fracture set 3 of both outcrops (Kaisberg sandstone: mean strike 168° ± 13°, Finefrau sandstone: mean strike 180° ± 11°) can be linked to the N-S striking fractures

(mean strike 179° ± 9°) of the Bork 10 dataset (Table 2.4). Solely the NW-SE trending fracture subset of fracture set 3 present in the Finefrau dataset are missing in the Kaisberg sandstone fracture population. However, this fracture orientation is weakly developed in the fracture population of the Bork 10 wellbore as NW-SE set (mean strike 140° ± 13°). Detected outcrop fracture data show similarities in their orientation distributions, despite the different positions within the southern margin of the Ruhr basin (see Figure 2.1) as well as different stratigraphic levels (Hattingen: Stockum anticline, Namurian C, Kaisberg sandstone; Nachtigall: Witten syncline, Westphalian A, Finefrau sandstone). Only the NW-SE trending fractures of the Finefrau sandstone outcrop are absent at the Kaisberg sandstone outcrop.

Fracture orientation and variations in dip may generally indicate different fracture generations ranging from those formed normal to bedding to inclined fracture sets.

Table 2.4: Summarized orientation statistics (strike, dip) and associated standard deviations for the fracture sets 1 – 3 of both outcrops as well as the fracture sets of the Bork 10 wellbore.

Data set		n	%	Mean strike [°]	Stdev. [°]	Mean dip [°]	Stdev. [°]
Hattingen, Kaisberg sandstone	Set 1	39	28	35	17	70	13
	Set 2	63	46	114	10	82	6
	Set 3	36	26	168	13	78	10
Nachtigall, Finefrau sandstone	Set 1	43	28	40	11	74	9
	Set 2	76	50	113	16	81	6
	Set 3	32	21	180	11	81	7
Bork 10 wellbore	N-S set	29	24	179	9	66	8
	NNE-SSW set	11	9	36	14	56	14
	W-E set	64	54	91	5	60	11
	NW-SE set	15	13	140	13	58	13

2.6.2 Fracture intensity

To derive outcrop-to-reservoir relationships, fracture intensity comparison between wellbore and outcrop data is of interest. We emphasize that only vertical intensity is measurable for the Bork 10 wellbore, which is not equally to intensity measured parallel to bedding (Gale et al. 2014). However, it can provide an insight into fracture abundance under subsurface conditions. Therefore, fracture intensities averaged over the total thickness of the drilled Upper Carboniferous sandstone units of the Bork 10 wellbore are set into relation to outcrop derived fracture intensities.

The orientations of the outcrop fracture sets 2 and 3 compare rather well to the W-E, respectively N-S fracture sets of the Bork 10 wellbore (Figure 2.5a, Figure 2.7a, Figure 2.9a). Accounting for the W-E set/set 2, the averaged Terzaghi corrected P_{10} of the Bork 10 wellbore (0.70 m^{-1}) is lower than the measured averaged intensities at both reservoir analogs (Hattingen: 1.21 m^{-1}, Nachtigall: 3.12 m^{-1}) (see Table 2.5). Deviations between subsurface and reservoir analog intensities are smaller for the N-S set/set 3, with the Bork 10s' Terzaghi corrected P_{10} (0.38 m^{-1}) approaching the corresponding fracture intensity of the Nachtigall outcrop (0.40 m^{-1}), still being more than two times lower than at the outcrop Hattingen P_{10} (0.73 m^{-1}) (Table 2.5).

In general, outcrop derived Terzaghi corrected average fracture intensities are between 1.1 to 4.5 times higher than wellbore derived P_{10} values. Beside the underestimation of the fracture quantity caused by the sampling challenge of the vertical wellbore (Narr 1996; Gale et al. 2014), surface stress relief associated fracturing as well as the horizontal scanline configuration might lead to higher fracture intensities in both outcrops (Gale et al. 2014; Becker et al. 2019b; Arndt et al. 2020).

Table 2.5: Terzaghi corrected fracture intensity averaged either for the length of the scanline or the total thickness of drilled Upper Carboniferous sandstone.

Fracture orientation	**Outcrop Hattingen (Kaisberg sst, Namurian C)**	**Outcrop Nachtigall (Finefrau sst, Westphalian A)**	**Bork 10 wellbore (Westphalian A)**
	Corrected mean fracture intensity P_{10} [m^{-1}]		
Set 1	2.02	0.58	-
Set 2 or W-E	1.21	3.12	0.70
Set 3 or N-S	0.73	0.40	0.38

2.6.3 Fracture height

Fracture height analysis could only be performed for the outcrop fracture networks. Borehole fracture height identification is difficult even if image log data would be available. Measured fracture height distributions can be used to derive three-dimensional fracture geometries, assuming a constant aspect ratio (height-length ratio) (Wüstefeld et al. 2018; Milad et al. 2018). Scanline derived fracture orientation data subdivided into three sets for detailed fracture network parameter characterization show no significant differences in measured height for both outcrops. Bed boundedness analysis revealed the Kaisberg sandstone fractures tend to follow a top bounded height distribution pattern after Hooker et al. (2013). Most of the tallest fractures end at mechanically significant interfaces, respectively bedding interfaces, with a wide range of smaller fractures to exist within the sandstone layer (Figure 2.6). Therefore, approximately 93 % of the detected fracture population either is restricted by the bed thickness (top- or base-bounded and perfect bed-bounded types) or is present within the layer itself (confined type). Only 5 % of the fractures are unbounded, thus cross the bedding interface (unbounded type) (Figure 2.6). The bed boundedness characteristics are mostly consistent between all three sets. However, unbounded, thus cross-bedding fractures are largely observed for set 2.

The Finefrau sandstone fractures appear to follow a top bounded height distribution pattern after Hooker et al. (2013) with approximately 96 % of the detected fracture population to be bed restricted (Figure 2.8). Therefore, bed-bounded fractures within fluvial channels are controlled by the variation in bed thickness along channel fills (Figure 2.4b). However, compared to the Kaisberg sandstone fracture network, the share of top- or base-bounded and perfect bed-bounded fractures is higher, with less fractures being of confined character (Figure 2.8). This might be related to the generally lower bed thickness of the exposed Finefrau sandstone.

2.6.4 Dipmeter log vs core description comparison

For the Bork 10 borehole a dipmeter log as well as detailed core description is available. However, the comparison of fracture depth location and dip azimuth indicates a mismatch between core and dipmeter log data (Figure 2.10a). The angular mismatch in dip azimuth might result from the 3-arm caliper tool (101 mm diameter) used for the dipmeter log. We infer that the picking of the fracture orientation in the dipmeter log has at least an error of 25°. The error in the determination of the dip azimuth at the drill core might be in a similar range. Additionally, it might be possible that the depth indications could be biased by core loss. Therefore, we assume an error of 6 m for the depth location of the core description.

Considering fractures observed at drill cores as reliable hard data, the quality of fracture interpretations from the dip meter log can be evaluated. Results indicate a limited suitability of the dipmeter log for fracture detection in this study, with neither the quantity of fractures nor their orientation and depth location are matching the hard data satisfactorily.

Drilling induced fractures (DIF) need to be removed from the core derived fracture population to avoid a bias. With only core descriptions available, no detailed distinction between DIF and natural fractures on the core material itself could be carried out. Since DIFs generally being oriented parallel to S_{Hmax} (154°) (Aadnøy and Bell 1998; Tingay et al. 2008), this fracture orientation is only rarely observed within the Bork 10 data set (Figure 2.9a). Therefore, a potential DIF bias appears to be negligible.

2.6.5 Critically stressed fracture analysis

Petrophysical data from the Upper Carboniferous Westphalian strata in the region (Greve et al. 2023) suggests the rock matrix to be generally tight (mean 6.8%; 0.18 mD). Thus, the reservoirs fracture network most likely controls the fluid flow in the Upper Carboniferous strata. Based on the correlation of critically stressed fractures with hydraulic conductivity demonstrated by Barton et al. (1995), fracture orientations with elevated likelihood to control fluid flow can be deduced.

The stress field described by scenario 1 (S_{Hmax} = 154°) represents the most likely S_{Hmax} orientation, highlighting near-vertical N-S and NW-SE striking fractures to be mechanically active and therefore having an elevated likelihood to be hydraulically conductive. While the NW-SE strike orientation is only rarely observed (13 % of the entire population) in the Bork 10 wellbore data set, N-S trending fractures are dominant (24 % of the entire population). Taking the standard deviation of S_{Hmax} into account, scenario 2 (S_{Hmax} = 121°) represents the lower bound of stress orientation. Since highest slip tendencies are observed for strike directions ± 30° to S_{Hmax}, near-vertical W-E and NNW-SSE to NW-SE trending fractures are partially critically stressed. Considering scenario 2, mostly W-E trending fractures seem to control fluid flow in the reservoir. The number of NNW-SSE to NW-SE trending fractures are low, thus they have only minor impact on fluid flow. The upper bound of possible S_{Hmax} orientations (S_{Hmax} = 187°) (scenario 3) revealed NNW-SSE and NE-SW to NNE-SSW striking fractures to be partially critically stressed. These orientations generally exhibit low frequencies within the detected fracture population of the Bork 10 wellbore.

2.6.5.1 Slip- and dilation tendency

The interaction of slip and dilation tendency controls the potential failure mode of fracture reactivation (Ferrill et al. 2020a). Generally, reactivation in shear mode is considered to be associated with fractures that exhibit moderate T_D and high T_S. Pure shear motion is linked to neutral volume change, assuming perfectly flat fracture surfaces. However, natural fractures are rough. Shear displaced fractures show shear dilation caused by the misfit between both rough fracture surfaces (Barton et al. 1985). This can lead to stress-resistant permanent permeability enhancement (Zimmermann et al. 2019; Cheng and Milsch 2021). Cheng and Milsch (2021) highlight the relationship of the increase in fracture aperture and hydraulic conductivity with the fracture surface roughness, as well as a generally higher self-propping potential for harder sedimentary rocks. Therefore, fractures reactivated in shear mode within the period of active present-day stress field may be responsible for today's fracture permeability.

In accordance to the results of the critically stressed fracture analysis, fracture orientations exhibiting highest slip tendencies, also experience moderate to partially high dilation tendencies. N-S and NW-SE striking fractures meet the requirements for reactivation in shear mode (high T_S and moderate T_D) under present-day stress conditions for the most reasonable stress scenario 1 (Figure 2.11). Regarding the standard deviation of S_{Hmax}, W-E and NNW-SSE to NW-SE strike direction for scenario 2 as well as NNW-SSE and NE-SW to NNE-SSW strike direction for scenario 3, are identified to be favorably oriented for shear reactivation. Depending on the stress field scenario, these fracture orientations represent potential fluid pathways created by combined shear and dilation (Barton et al. 1985).

2.6.5.2 T_S and T_D sensitivity to S_{Hmax} orientation

Comparison of the T_S and T_D results for scenario 1, 2 and 3 shows the detected fracture population's sensitivity to the S_{Hmax} direction. With S_{Hmax} being associated with a quantified uncertainty of ± 33°, scenario 2 and 3 covers the possible range of S_{Hmax} orientation under the assumption of a pure strike-slip faulting regime.

Analysis indicates a larger share of the detected fracture population (Bork 10) to exhibit slip tendencies exceeding $\mu = 0.67$ (Ruhr sandstone) for a S_{Hmax} orientation of 121° (Figure 2.14a). With 3 % (n = 3) of the fracture population exceeding $\mu = 0.67$ for S_{Hmax} = 187° (scenario 3), these numbers increase for a S_{Hmax} orientation of 154° (scenario 1) with 10 % (n = 12) being critically stressed. The highest share of fractures exceeding $\mu = 0.67$, respectively being critically stressed (17 %, n = 20) is observed for S_{Hmax} = 121° (scenario 2) (Figure 2.14a).

Dilation tendency exceeding $T_D = 0.9$ is most frequently observed for a S_{Hmax} orientation of 187° (scenario 3) with 14 % (n = 17) of the detected fracture network of the Bork 10 wellbore exceeding this threshold (Figure 2.14b). Significantly lower proportions of the fracture population with dilation tendencies greater than 0.9 are observed for scenarios 1 and 2 (3 % (n = 4) respectively 1 % (n = 1)) (Figure 2.14b).

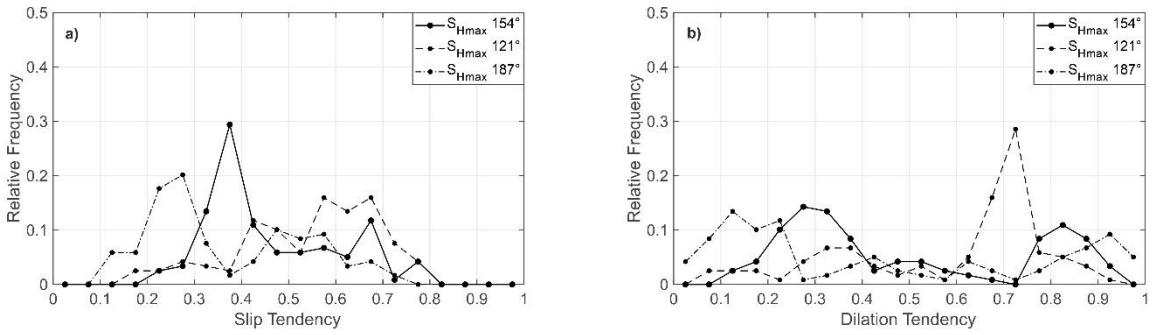

Figure 2.14: a) Relative frequency of the slip tendency calculated for different S_{Hmax} scenarios. b) The relative frequency of dilation tendencies derived for the detected fractures of the Bork 10 wellbore show differences for varying S_{Hmax} orientations.

2.6.5.3 Coefficient of friction

CSF analyses utilize slip tendency in relation to the rocks coefficient of static friction (μ) for cohesionless surfaces, to distinguish between critically and non-critically stressed states. Therefore, the choice of this material parameter controls the percentage of detected fractures classified as mechanically active. The coefficient of static friction ($\mu = 0.67$) used in this study corresponds to fractured Ruhr Sandstone (Kruszewski et al. 2021). Stoeckert et al. (2020) indicate lower coefficients of friction for Carboniferous sandstones containing coal (down to $\mu = 0.55$) or fractures containing clay mineral precipitates (down to $\mu = 0.12$). This could justify the application of lower friction coefficients, which in turn would lead to more critically stressed fractures. Furthermore, Byerlee (1978) described a range for coefficients of friction starting from 0.6. Thus, the coefficient of friction of $\mu = 0.67$ applied in this study can be considered as a conservative approach.

2.6.6 Considerations on exploration strategy

Amongst aspects of borehole stability and availability of drilling locations, the wellbore design generally depends on the wellbore connection to the reservoir fracture network (Ehlig-Economides et al. 2000; Mahmoodpour et al. 2022). In this respect, the orientation of hydraulically conductive fracture trends is a key information. As for a pure strike-slip faulting regime, near-vertical fractures exhibit the highest likelihood to be partially critically stressed, dependent on their strike direction relative to the S_{Hmax} orientation, a horizontal wellbore configuration will maximize the number of intersected fractures. Additionally, wellbore trajectories should be aligned perpendicular to conductive fracture directions for maximum wellbore productivity (Ehlig-Economides et al. 2000).

The Upper Carboniferous of the Ruhr basin hosts natural gas from coal seams with generally lower gas contents associated with normal faults (Juch et al. 2004; Mösle et al. 2009). NW-SE striking normal fault segments may exhibit higher slip tendencies within the present-day stress field according to stress scenario 1 (S_{Hmax} 154°). Further, NW-SE striking normal faults are reported to be fluid migration pathways (Hahne and Schmidt 1982; Hinderfeld et al. 1993), which would match the finding of the scenario 1 CSF analysis on a larger scale.

Future potential geothermal exploration would need to concentrate on depth levels of around 4000 m to ensure sufficient reservoir temperatures. Depth-dependent changes in the stress regime could result in deviations from the strike-slip regime used in this study.

While the Finefrau sandstone has a thickness of 7.2 m, measured at the Nachtigall outcrop, its thickness decreases towards 1.3 m observed in the Bork 10 wellbore. With the Nachtigall outcrop located at the south-eastern edge of the Ruhr basin and the Bork 10 wellbore in a more basinwards position (Figure 2.1), a lower thickness of the Finefrau sandstone is observed for the more distal position within the Ruhr basin. This coincides with reported sediment transport directions ranging from south towards north to east towards west (Drozdzewski 2005; Schäfer 2019).

2.6.7 Impact on mine flooding in the Ruhr basin

A detailed understanding of the Upper Carboniferous fracture network might be beneficial in the context of rising mine water levels following the end of hard coal mining in the Ruhr basin (Drobniewski et al. 2017; Westermann et al. 2020; Rische et al. 2021, 2023). To better assess the spatial evolution of increasing pore pressure, knowledge of the influence and attributes of structural fluid migration pathways is required.

Fluid flow is expected to be mostly layer restricted with less than 5% of the fractures are unbounded and crossing different sandstones beds in an overall tight sandstone (average porosity of 8 % and a permeability up to 3 mD (Greve et al. 2023)) in a multibarrier system of sandstone shale cycles. Wellbore derived fracture intensities of up to 9.1m^{-1} indicate the degree of fracturing of the host Upper Carboniferous.

Although N-S and NW-SE striking fractures might contribute in the context of rising mine water levels (following stress scenario 1), fluid flow is mainly restricted to galleries and shafts. A zone of construction-related tensile and shear fractures close to the walls might be present (Shen and Barton 2018).

2.7 Conclusion

Fracture network characterization of the Kaisberg (Namurian C, outcrop Hattingen) and Finefrau sandstone (Westphalian A, outcrop Nachtigall) revealed comparable outcrop fracture orientation statistics for three dominant fracture sets at different stratigraphic intervals and geographic positions within the southern margin of the Ruhr basin: NNW-SSE to N-S, NNE-SSW to NE-SW and WNW-ESE. Additionally, both outcrop fracture networks show top bounded height distribution patterns with fracture height generally limited by bed thickness. Corrected fracture intensities (P_{10}) differ between all fracture sets as well as both outcrops, ranging from a minimum of 0.40 m^{-1} to a maximum of 3.12 m^{-1}.

Fractures detected in core material of the Bork 10 wellbore strike in two dominant orientations: N-S and W-E. Both fracture trends match the orientations of the outcrops fracture sets 2 and 3. Weakly pronounced NNE-SSW and NW-SE striking fractures are present in the detected fracture population, with the NNE-SSW trending set matching the outcrop's fracture set 1. The averaged fracture intensity in the Bork 10 wellbore is up to 4.3 times lower than observed at the outcrops. The comparison of dipmeter log fracture interpretation with core descriptions of the Bork 10 wellbore suggests dipmeter logs as a less suitable tool for in this study.

Fluid flow within the Upper Carboniferous sandstone units is most likely governed by the reservoirs fracture network due to the low matrix permeability. 10% of the detected fractures within the Bork 10 wellbore are critically stressed, considering a pure strike-slip faulting regime (scenario 1, S_{Hmax} = 154°). N-S as well as NW-SE striking near-vertical fractures are expected to be hydraulically conductive. NNW-SSE striking fractures are subject to the highest dilation tendencies and therefore preferably oriented for dilation under present-day stress conditions with 3 % of the entire fracture population exceeding dilation tendencies of 0.9 (scenario 1, S_{Hmax} = 154°).

Taking the uncertainties of S_{Hmax} orientations into account, CSF analysis identified either W-E and NNW-SSE to NW-SE striking fractures (scenario 2, S_{Hmax} = 121°) or NNW-SSE and NE-SW to NNE-SSW trending fractures (scenario 3, S_{Hmax} = 187°) as potentially hydraulically conductive under the given stress conditions. Dilation is most likely for either WNW-ESE to NE-SE striking fractures (scenario 2, S_{Hmax} = 121°) or N-S trending fractures (scenario 3, S_{Hmax} = 187°). Overall, mine flooding is focused on shafts and galleries, while rising water levels in the host rock are controlled by the natural fracture network.

2.8 Bedding dip removal for better comparability

In extension of the published study by Allgaier et al. (2023), bedding dip removal is applied for the analyzed fracture data sets in order to assess the angular relationship between fracture and bedding.

After bedding dip removal, the analyzed Hattingen and Nachtigall outcrops are predominantly composed of high-angle fractures with respect to bedding (dip angle > 75°) (Figure 2.15 a, b), comprising

89 % and 70 % of the respective outcrop datasets (Figure 2.15 e, f). Fractures with an intermediate angle to bedding (dip angle between 45° and 75°) occur significantly less frequently for the Hattingen (30 %) and Nachtigall (11 %) datasets.

Fractures of the Bork 10 core description dataset show a range of dip angle with respect to bedding (Figure 2.15 c, g). The majority (64 %) is represented by intermediate-angle fractures (45° to 75°), followed by high-angle fractures (25 %) (>75°) and low-angle fractures (11 %) (<45°). The dipmeter log fracture dataset is dominated by high-angle fractures (44 %) and intermediate-angle fractures (44 %), followed by low-angle fractures (13 %) (Figure 2.15 d, h).

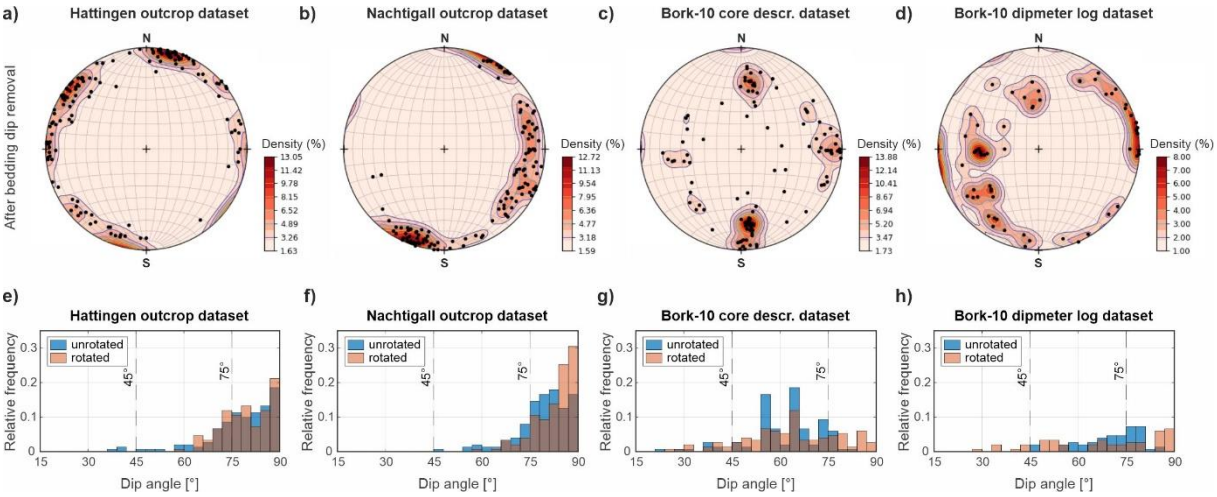

Figure 2.15: a, b, c, d: Fracture pole plots of the outcrop and well datasets after bedding dip removal. e, f, g, h: Histograms (bin size of 3) highlighting the dip angle distribution of the analyzed datasets before and after bedding rotation. Bedding orientation varies between the outcrops Hattingen (117/31) and Nachtigall (331/12). Bedding within the Bork 10 well changes with depth as the dip azimuth ranges between 115° and 145°, while bedding dip varies between 5° and 28°.

Both outcrops as well as the Bork 10 well share a comparable structural setting as they are located on gently dipping (up to 31°) fold limbs, dipping either to the NNW (Nachtigall outcrop) or ESE (Hattingen outcrop and Bork 10 well). In addition, they are hosted within the Upper Carboniferous sequence and therefore share the same lithological setting (Namurian C to Westphalian A). Both outcrops are dominated by high-angle fractures with respect to bedding, while the subsurface datasets are characterized by a mixture of high and intermediate-angle fractures. The lower relative share of high-angle fractures observed for the subsurface datasets might be due to the sampling challenge of detecting near-vertical fractures within a vertical well (Terzaghi 1965; La Pointe et al. 1993; Laubach et al. 2000). In addition, this might be explained by the different uplift histories, as both outcrops lack significant horizontal and vertical confining pressure due to its surface exposure. Stress relief-induced fracturing at low differential stresses might have introduced the formation of extensional high-angle fractures, which are absent in the subsurface dataset. Furthermore, it is noticeable that in both outcrop datasets, intermediate-angle fractures are significantly underrepresented compared to the subsurface datasets.

3 Post-mining related reactivation potential of faults hosted in tight reservoir rocks around flooded coal mines, eastern Ruhr Basin, Germany

3.1 Abstract

The cessation of hard coal mining in the Ruhr Basin in 2018 marked the region's transition to the post-mining phase. Controlled mine water rebound induces changes in the subsurface stress conditions, as pore pressure increases locally. Presently, mine water rebound is observed in the eastern Ruhr Basin (water province “Haus Aden”) along with associated microseismicity. Furthermore, post-mining challenges might comprise the potential risk of fault reactivation, which is addressed in this study by conducting a fault slip assessment.

Based on subsurface coal seam mapping data, a 3D structural model for the NE part of the “Haus Aden” water province has been constructed to serve as the basis for identifying the most vulnerable fault trends and types of the structural inventory. Slip tendency analysis, considering normal faulting conditions, revealed NW-SE to NNW-SSE trending normal faults to be most susceptible to reactivation. Probabilistic fault slip assessment, focused on NW-SE to NNW-SSE trending normal faults mapped within the “Heinrich-Robert” colliery, show no fault reactivation potential for a mine water rebound up to a level of 640 m below ground. Assuming hydrostatic conditions in the vicinity of the faults, friction coefficients are only partially exceeded for high differential stresses.

In addition, a novel workflow is used to model the spatial variability of the frictional fault strength as input for a fault stability analysis, exemplified for a selected NNW-SSE trending normal fault. For considering hydrostatic pore pressure, results show that the fault consists mainly of stable, but also unstable, horizontally elongated patches. These findings question the conventional simplified approach of using a single constant friction coefficient for fault stability analysis.

3.2 Introduction

With the final cessation of hard coal mining in the Ruhr Basin, Germany, in 2018, the region entered the post-mining phase (Kretschmann et al. 2017; Balzer and Roth 2019; Aristizabal-H et al. 2023). Due to the resulting technical-operational obsolescence of mine water pumping, mine water levels were intentionally allowed to rise up to predefined levels (RAG AG 2014). Consequently, the controlled mine water rebound increases the in situ pore pressure state (Donnelly et al. 2008), as former hard coal mining

activities locally required the lowering of water levels through pumping to achieve dry working conditions. Post-mining challenges associated with the alteration of the local stress conditions might comprise mine water rebound-induced fault reactivation, as observed for hard coal mining in other areas worldwide (Donnelly 2006; Klose 2007; Donnelly et al. 2008; Kinscher et al. 2018; Zhao and Konietzky 2021).

At present, mine water rebound is taking place in the eastern Ruhr Basin (water province "Haus Aden"), with associated microseismicity being documented (Rische et al. 2023). To date, detailed fault reactivation studies have been conducted for the Ruhr Basin (Kruszewski et al. 2022a; Kruszewski et al. 2022b; Kruszewski et al. 2023), assuming strike-slip faulting conditions, however, a detailed analysis for the fault system in the water province "Haus Aden" is still lacking. Based on the work of Niederhuber et al. (2023a), it is clear that the stress field in the Ruhr Basin is not uniformly distributed, which emphasizes the importance of site-specific stress field analyses over large-scale approaches. The published stress data of Stelling and Rummel (1992), collected around the "Haus Aden" colliery, indicate normal faulting conditions. This is consistent with published data from Niederhuber et al. (2023b), enabling an in-depth examination of the post-mining fault reactivation potential.

Fault reactivation potential is generally evaluated by applying the slip tendency approach (Moeck et al. 2009; Worum et al. 2004; Lee et al. 2017) developed by Morris et al. (1996). Therefore, a detailed structural description of the study area is essential as slip tendency magnitudes depend among others on fault geometry characteristics (strike and dip) (Ferrill et al. 2020b). Beside deterministic slip tendency analysis, probabilistic approaches additionally account for input parameter uncertainties (Healy and Hicks 2022). While fault reactivation analyses typically consider Mohr-Coulomb frictional failure theory and a homogeneous value for the friction coefficient (Moeck et al. 2009; López 2012; Vadacca et al. 2021; Ekpo Johnson et al. 2023; Zhang et al. 2023), outcrop studies suggest a heterogeneous spatial distribution of the frictional fault strength along faults (Childs et al. 1997; Kato and Hirono 2016). Since the spatial variability of the frictional strength of subsurface faults cannot be studied due to inaccessibility, a clay content prediction algorithm based on a perfect clay mixing model can be utilized to either derive the spatial distribution of fault rock types (Meng et al. 2017) or frictional coefficients (Jin et al. 2023). However, Freeman et al. (2008) suggest non-perfect clay mixing models as more suitable, since outcrop observation could be matched more satisfactorily.

Within this study, we first construct a structural 3D model covering the NE part of the water province "Haus Aden" based on 2.5-dimensional legacy data, acquired during decades of active hard coal exploration and mining (Juch 1996). Additionally, we validate the derived 3D model with depth structure map information. Applying slip tendency analysis on the constructed fault model enables us to identify the most susceptible fault trends and types. We incorporate probabilistic fault slip assessment for the identified most vulnerable fault trend to account for input parameter uncertainties (stress magnitudes and orientation as well as geometric fault attributes). A workflow is proposed to assess fault stability based

on spatially heterogeneous frictional fault strength model. We exemplarily model the spatial variability of the friction coefficient for a selected fault based on well log data, using a non-perfect clay mixing model. Beside the assessment of the potential of post-mining related fault reactivation, the derived results might also provide beneficial insights for the current roll-out of deep geothermal exploration in the Ruhr Basin, within the context of the discussed German Heat Transition.

3.3 Geological setting

The Ruhr Basin, as a molasse-type foreland basin formed during the Variscan orogeny, extends laterally for 150 km along-strike in NE-SW direction and 80 km across-strike (Drozdzewski 1993; Drozdzewski et al. 2009). The Ruhr region was once the primary hub of hard coal mining in Germany (Drozdzewski 1993; Drozdzewski and Wrede 1994; Meschede and Warr 2019), with a maximum annual production of 123.000 t hard coal in 1957 (Statistik der Kohlenwirtschaft e.V. 2019). Basin initiation was caused by the Late Palaeozoic convergence of Gondwana and Laurussia (Ziegler 1982). The Variscan deformation front migrated NW-ward contemporaneous to sedimentation in the foreland basin (Drozdzewski 1993), with the Upper Carboniferous molasse sediments reflecting the latest stage of the Variscan orogeny (Drozdzewski and Wrede 1994). The depositional environment in the foreland basin developed from marine to shallow-marine through coastal plain to deltaic conditions (Drozdzewski 1993), with coal-formation taking place between the Namurian C and Westphalian D (Bashkirian – Moscovian, 320 – 305 Ma) (Drozdzewski and Wrede 1994; Suess et al. 2007; Schäfer 2019). Thus, the up to 3500 m thick coal-bearing Upper Carboniferous strata (Schäfer 2019) consists of cyclically occurring sandstones, siltstones, claystones and coal seams (Richter 1971; Suess et al. 2007), building up the 5000 to 7000 m thick sedimentary infill of the Ruhr Basin (Drozdzewski and Wrede 1994). The NW-migrating Variscan deformation front tectonically overprinted the sediments of the Ruhr Basin as a foreland fold-and-thrust belt, with deformation of post-Westphalian age (Drozdzewski 1993). Variscan shortening of up to 50 % near the Variscan orogen decreases to 5-10 % towards the NW (Brix et al. 1988).

The post-Variscan development of the Ruhr Basin is marked by uplift and erosion of the Variscan orogen in the Rotliegend (Permian) (Drozdzewski and Wrede 1994), followed by a subsidence phase from the Late Permian that lasts until the Early Jurassic. Inversion affected the Ruhr Basin in the Late Jurassic and Early Cretaceous, followed by repeated sediment deposition in the Late Cretaceous (Büker 1996). This is reflected in the bedding conditions, with the folded Upper Carboniferous being unconformably overlain by subhorizontal transgressive marine sediments of Cretaceous age (Richter 1971; Drozdzewski 1993; Drozdzewski and Wrede 1994). With a maximum thickness of 2000 m in the Münsterland region, the Cretaceous basin infill thickens towards NW (Richter 1971; Drozdzewski 1993).

Late- to post-Variscan normal faults subdivide the folded Upper Carboniferous into horst and graben systems in the study area, trending WNW-ESE to NW-SE (Drozdzewski and Wrede 1994; Geologischer Dienst NRW 2020) (Figure 16). The fault activity peaked during the Upper Triassic and Upper Jurassic

(Drozdzewski and Wrede 1994; Geologischer Dienst NRW 2020), with additional post-Cretaceous activity reported for the normal faults Königsborner Sprung (Bärtling 1921) and Flierischer Sprung (Stach 1923) in the studied area. Normal faults are often characterized by oblique slip kinematics, with dip slip displacement magnitudes of up to thousand meters (Pilger 1956; Richter 1971; Drozdzewski and Wrede 1994; Geologischer Dienst NRW 2020) and sinistral as well as dextral horizontal slip kinematics (Drozdzewski and Wrede 1994; Geologischer Dienst NRW 2020). Steeply dipping W-E and N-S trending strike-slip faults occur as additional tectonic feature in the Ruhr Basin (Figure 16) (Geologischer Dienst NRW 2020). Dextral kinematics are reported for the E-W fault trend, while N-S trending strike-slip faults are associated with sinistral movement (Drozdzewski and Wrede 1994).

The water province “Haus Aden” hosts the former “Bergwerk Ost” colliery, which was established by the merger of the formerly independent collieries “Monopol” (M), “Haus Aden” (HA) and “Heinrich-Robert” (HR) in 1998 (Scheidat and Kirsch 2000) (Figure 16b). The study area is located within the Bochum syncline, which is characterized by overall low-angle bedding (Figure 16c) (Drozdzewski and Wrede 1994; Geologischer Dienst NRW 2020). Due to the geological segmentation into horst and graben structures, mining operations were conducted at various depth levels (down to -1500 m) within the "Bergwerk Ost" colliery.

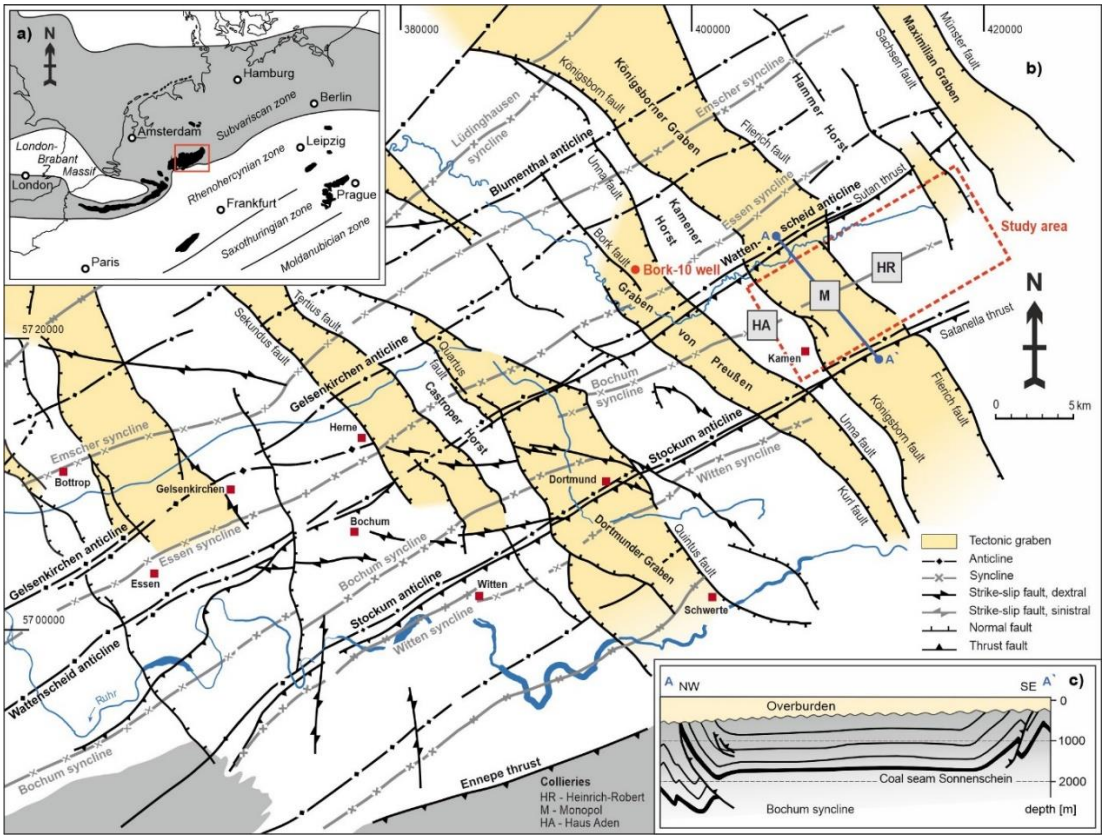

Figure 16: a) The Ruhr Basin located in west Germany is a Variscan foreland basin. Blacked-out areas are referred to as coal provinces (modified after Drozdzewski and Wrede (1994)). b) Overview of the eastern part of the Ruhr Basin, subdivided into characteristic NNW-SSE trending horst and graben structures (modified after Geologischer Dienst NRW (2020)). c) Simplified cross-section in NW-SE orientation (modified after Drozdzewski and Wrede (1994)).

3.4 Methods

3.4.1 Structural model

A structural 3D model of the NE part of the water province "Haus Aden" is constructed to analyze the structural inventory of the study area. The modeling task is performed based on the existing KVB model (KVB = Kohlenvorratsberechnung = coal resources calculation) of the geological survey of North Rhine-Westphalia (Juch 1996). This digital 2.5-dimensional model has been developed based on a geometrical approximation of the spatial position of undisturbed coal seam sections to serve for a detailed hard coal resource assessment (Juch 1996). Since the folds in the Ruhr Basin are mostly characterized as chevron-type or box-type (Brix et al. 1988), the coal seam sections can be approximated by planar polygons (Juch 1996). Thus, the KVB model provides a promising data base describing the structural configuration of the Upper Carboniferous of the Ruhr Basin.

Structural modeling is performed using the Petrel software suite (SLB). In order to construct the structural framework, horizon geometries are modeled based on the coal seam polygons extracted from the KVB model. Because there is no spatial information within the individual coal seam polygons, we need to augment each polygon with randomly generated points distributed within its area to avoid artefacts when performing horizon modeling. This preprocessing step is accomplished using a custom Matlab script. Vertical offset between individual coal seam polygons are interpreted as faults.

A detailed depth structure map of the Sonnenschein coal seam (Westphalian A) is utilized to study small-scale tectonics, which might be not resolved in the KVB model. The coal seam depth map covers the Hammer horst structure between the normal faults Fliericher Sprung and Radbod Sprung in the east of the studied area. Thus, the area between the large faults can be structurally resolved in greater detail.

3.4.2 Fault slip assessment

Slip tendency (T_S) is used as proxy to assess the likelihood of fault reactivation in shear mode. Calculated based on effective principal stresses, the slip tendency (T_S) is defined as the ratio of resolved shear stress (τ) to normal stress (σ_n), acting on a plane of interest. Conditions for reactivation in shear mode are given if slip tendency (T_S) exceeds the coefficient of static friction (μ), acting as frictional resistance against slip initiation between two non-moving rigid bodies (Morris et al. 1996):

$$T_s = \frac{\tau}{\sigma_n} \geq \mu \qquad (1)$$

Slip tendency is deterministically computed for the tectonic inventory of the constructed 3D fault model using the Stress Analysis tool of the MOVE Software Suite (Petroleum Experts Ltd.) to highlight the spatial T_S distribution along the modeled fault surfaces as well as to identify the most exposed fault

trends within the NE part of the water province “Haus Aden”. In a next step, a probabilistic slip tendency analysis (1000 Monte Carlo realizations) is conducted for the identified critical fault orientations in order to account for the input parameter (stress field model and fault geometry) uncertainties. For this purpose, the probabilistic fault slip Python script developed by Healy and Hicks (2022) is employed.

The magnitudes and orientation of the in situ stress field of the Ruhr Basin were subject to several studies (Stelling and Rummel 1992; Kruszewski et al. 2021; Kruszewski et al. 2022a; Niederhuber et al. 2023a). The Stelling and Rummel (1992) dataset is part of the published stress data compilation of Kruszewski et al. (2022a), feeding into an averaged stress model (strike-slip faulting regime) for the entire Ruhr Basin. However, the stress field in the Ruhr Basin is not uniformly distributed as indicated by Niederhuber et al. (2023a). Therefore, the location-specific stress data set of Stelling and Rummel (1992) is chosen as input for this study, indicating normal faulting conditions. Stelling & Rummel (1992) investigated the primary stress state in the Upper Carboniferous based on hydraulic fracturing measurements, conducted in the then still untested northern field of the “Haus Aden” mine. Based on two horizontal (B1/H, B2/H) and vertical (B3/V, B4/V) boreholes, starting from the -940 m level (1000 m below ground), the minimum and maximum horizontal as well as the vertical stresses were determined, describing a normal faulting regime.

We filtered the data set to use only stress measurements taken at least at 20 m distance to the gallery to ensure the representation of the primary stress state, as proposed by Stelling and Rummel (1992). In addition, the stress measurements were checked for plausibility. Therefore, the following stress magnitudes and associated standard deviations (at 1000 m below ground) are calculated based on the B1/H and B3/V wells with the exception for σ_V, for which we assume a standard deviation of 0.5 MPa due to the lack of variability in the measured values: $\sigma_V = 23.6 \pm 0.5$ MPa, $\sigma_{Hmax} = 21.4 \pm 0.8$ MPa and $\sigma_{h\text{-}min} = 16.6 \pm 1.4$ MPa (Table 6).

The regional stress orientation, representative for the study area, is taken from Niederhuber et al. (2023a) with a σ_{Hmax} direction of N156°E ± 13°. Niederhuber et al. (2023a) derived the regional stress orientation from hydraulic fracturing measurements within coal mines from various reports and applied data filtering for measurements influenced by mining operations or stress changes around mine infrastructure. The σ_{Hmax} direction (N156°E ± 13°) can be converted to a Von Mises distribution via the Stereonet software tool (Allmendinger 2023), described by a mean of 156° and a shape parameter (κ) of 16.9 (as a measure of concentration around the mean) (Table 6).

The spatio-temporal pore pressure evolution (P_P) in the study area is impacted by mine water drainage during active mining. Dry conditions are achieved within the mining area by pumping, while hydrostatic conditions might prevail at unspecified distances around it. This hypothesis might be supported by the fact, that the Upper Carboniferous sedimentary succession is characterized as hydraulically tight (Greve et al. 2023), which might delay pore pressure re-equilibrate over wider distances. During the post-mining phase, the mine water rebound is designed to rise up to a depth level of 640 m below ground (RAG AG

2014), re-introducing pore pressure within the mining areas (3.7 MPa at 1000 m below ground). The water level will be kept at that level forever by pumping out excess water (eternity costs) (RAG AG 2014). Still hydrostatic conditions might prevail outside the affected area. Thus, the effective pore pressure in the vicinity of the faults fall somewhere between near-hydrostatic to hydrostatic conditions. The mine water levels have been rising since 2020 at the "Heinrich-Robert" colliery, currently at 790.7 m BMSL, respectively ≈ 850 m below ground (as of August 29, 2023) (RAG-BID 2023). Deeper mining levels of the former "Bergwerk Ost" colliery are already flooded, according to Rische et al. (2023).

Table 6: The stress field of the NE-part of the water province "Haus Aden" (considered depth level of 1000 m below ground), characterized by a normal faulting regime.

Parameter	Mean	Std.	Distribution type
σ_V	23.6 MPa	0.5 MPa	Normal
σ_{Hmax}	21.4 MPa	0.8 MPa	Normal
σ_{hmin}	16.6 MPa	1.4 MPa	Normal
P_P	10.4 MPa	-	
	3.7 MPa	-	
σ_{Hmax} azimuth	156°	13°	Normal
	Mean	**κ**	
	156°	16.9	Von Mises

The fault slip assessment requires a frictional fault strength criterion to determine the likelihood of fault reactivation. Since the Upper Carboniferous lithologies comprise mostly of sandstones, siltstones, claystones, mudstones and coal seams (Greve et al. 2023), the upper limit for the frictional fault strength is given by a coefficient of static friction (μ) of 0.67, measured under laboratory conditions for fractured Ruhr sandstone (Kruszewski et al. 2021). The lower limit is assumed by a coefficient of static friction (μ) of 0.5, representative for Upper Carboniferous shales from the Groningen gas field (Hunfeld et al. 2017).

3.4.3 Distance-to-failure analysis

Faults conceptually consists of hanging and footwall damage zones surrounding the fault core, where most of the strain is localized (Chester and Logan 1987; Caine et al. 1996; Shipton and Cowie 2001). In this zone, different fault rock types can develop depending on the clay content of the faulted host lithologies (Yielding et al. 2010). Here, fault gouge is assumed as the main fault rock type for the Upper

Carboniferous sequence. The frictional strength of the fault gouge depends, among other factors, on its mineralogical composition (Takahashi et al. 2007; Tembe et al. 2010; Kohli and Zoback 2013; Bedford et al. 2022), which is controlled by the faulted host lithologies and thus, on fault displacement. As fault displacement generally varies along-strike (Lewis et al. 2009; Torabi et al. 2019), a heterogeneous pattern of the frictional fault strength along fault zones is likely (Meng et al. 2017; Jin et al. 2023).

To methodically and exemplarily study this phenomenon, we analyze the fault stability of a selected critically-oriented NNW-SSE trending fault in the vicinity of the "Heinrich-Robert" colliery (located on the Hammer horst) by modeling the spatial variability of the friction coefficient. This is done by estimating the fault clay content using the Effective Shale Gouge Ratio (ESGR) algorithm, performed within the Petrel software suite (SLB). A simple geomodel is set up, spatially located on the Hammer horst (Figure 16), with well log data (Bork 10 well) originating from neighbouring regions. The shale volume (V_{sh}) is derived from gamma ray (GR) log data using the Clavier equation (Clavier et al. 1971) based on the previous calculated gamma ray index (IGR) (Rider and Kennedy 2011):

$$IGR = \frac{GR_{log} - GR_{shale}}{GR_{sand} - GR_{shale}}$$

with GR_{log} representing the GR reading in the zone of interest. The sand line (GR_{sand}) is defined at 70 API as the Upper Carboniferous sandstones contain significant amounts of detrital fragments rich in sheet silicates (shale rock fragments, phyllites) (Greve et al. 2023). The shale line is set at 205 API as the Upper Carboniferous claystone sequences show extreme high GR readings (up to 240 API). The V_{sh} calculation after Clavier is defined as (Clavier et al. 1971):

$$V_{sh} = 1.7 - \sqrt{3.38 - (IGR + 0.7)^2}$$

Based on a stochastically populated V_{sh} property model, the clay content for any point on the fault is predicted by using the Effective Shale Gouge Ratio (ESGR) algorithm (Knipe et al. 2004):

$$ESGR = \frac{\sum V_i * \Delta z_i * w_i)}{\sum \Delta z_i * w_i}$$

With the summation over all slipped units i taking the clay content (V_{sh}) V_i, the thickness Δz_i and the weighting factor w_i (Petrel default weighting function) into account (Freeman et al. 2010).

To establish the relationship between the friction coefficient and fault rock clay content requires a study-tailored measurement campaign, which is outside the scope of this study. Hence, the function proposed by Jin et al. (Jin et al. 2023) is taken for modeling, linking the predicted clay content to the static friction coefficient (μ):

$$\mu = 0.1703\ tan^{-1}(-7.022V_{sh} + 3.131) + 0.5013$$

Here, 0 % clay content relates to a friction coefficient of μ = 0.72, which is consistent with published data for fractured Ruhr sandstone (μ = 0.67) (Kruszewski et al. 2021).

To assess fault stability, we quantify the Failure Criterion Stress (FCS) by utilizing the Distance-to-failure tool within the Petrel software suite (SLB). The Failure Criterion Stress (FCS) is defined as the shortest distance between the Mohr-Coulomb failure criterion and the point on the Mohr circle representing the fault of interest (Figure 17). Here, given for optimally oriented faults (Shapiro 2015):

$$FCS = 0.5\sigma_d - sin\varphi_f\left(\sigma_m - P_p\right) - C_c cos\varphi_f$$

Where $\sigma_d = \sigma_1 - \sigma_3$ is the differential stress, φ_f is the friction angle ($\mu = tan\varphi_f$), $\sigma_m = (\sigma_1 + \sigma_3)/2$ is the mean stress, P_p is the pore pressure and C_c is the cohesion. To follow the FCS sign convention, scalar multiplication by -1 is applied to the Distance-to-failure results, as Petrel uses the reverse sign convention. Stable stress conditions are indicated by negative FCS values, while positive FCS values imply unstable stress states.

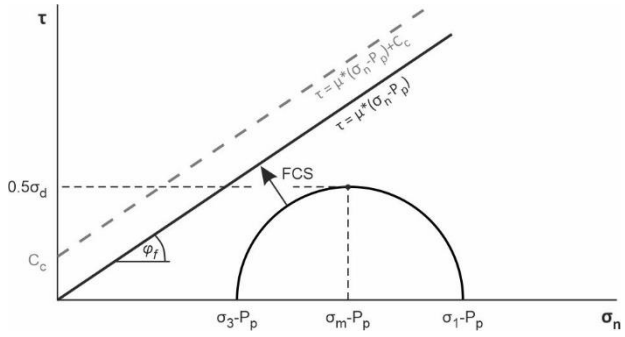

Figure 17: The Failure Criterion Stress (FCS) is defined as the shortest distance between the failure envelope and the point, representing the fault of interest. Here, displayed for the optimal fault orientation.

3.5 Results

3.5.1 Structural model

Based on the KVB model, individual coal seams have been identified, along with all associated coal seam segments. Data has been transferred into Petrel in order to display the 3D subsurface geometries (Figure 18a). A fault model has been constructed based on the offset between individual segments of several coal seams and validated against geological maps (Figure 18b). To derive 3D subsurface geometries, horizon modeling has been performed for the spatial extent of the Bochumer main syncline, based on the coal seam segments and constructed faults (Figure 18c).

Thus, the derived structural 3D model describes the large-scale tectonic features of the study area. NW-SE to NNW-SSE trending normal faults, subdividing the study area into a horst and graben system, are the dominant structural feature (Figure 19a). N-S and WNW-ESE trending faults represent a subordinate part of the 3D model (Figure 19b). Folding is documented by anti- and synclines with WSW-ESE trending fold hinges (Figure 19b).

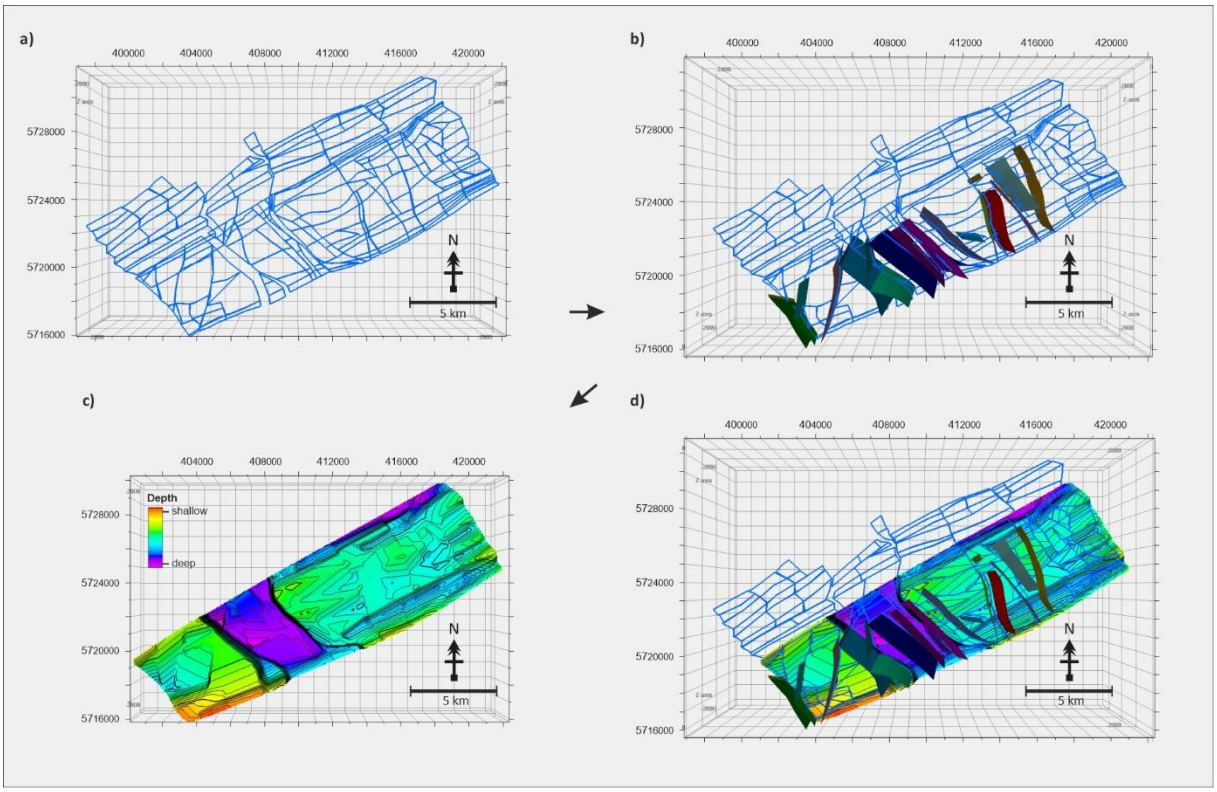

Figure 18: a) KVB model polygons of the coal seam Sarnsbank (Sprockhövel-Fm., Namurian C, FLZ 0654/107) (CRS: UTM WGS84 32U). b) Coal seam polygons with constructed fault network of the study area. c) Modeled coal seam horizon (Sarnsbank). d) Input data and modeling results shown together.

The structural inventory described by the depth map of the Sonnenschein coal seam (Westphalian A) comprise normal, strike-slip and thrust faults (Figure 19c). While dip slip kinematics are reported for the normal and thrust faults, no shear sense indication is given for the strike-slip faults. Orientation statistics reveal a dominant NW-SE to NNW-SSE trend, with N-S and W-E striking faults subordinately developed (Figure 19d). While the normal faults generally trend NW-SE (N143.5°E) (Figure 19e), strike-slip faults occur at various orientation, with roughly NW-SE to N-S and W-E trends dominating (Figure 19f). Mapped fold axes and thrust faults appear at NE-SW to WSW-ESE orientation (Figure 19g). The Hammer horst as part of the km-scale characteristic horst and graben structures in the Ruhr Basin comprises lower-order horst and graben structures within (Figure 19c).

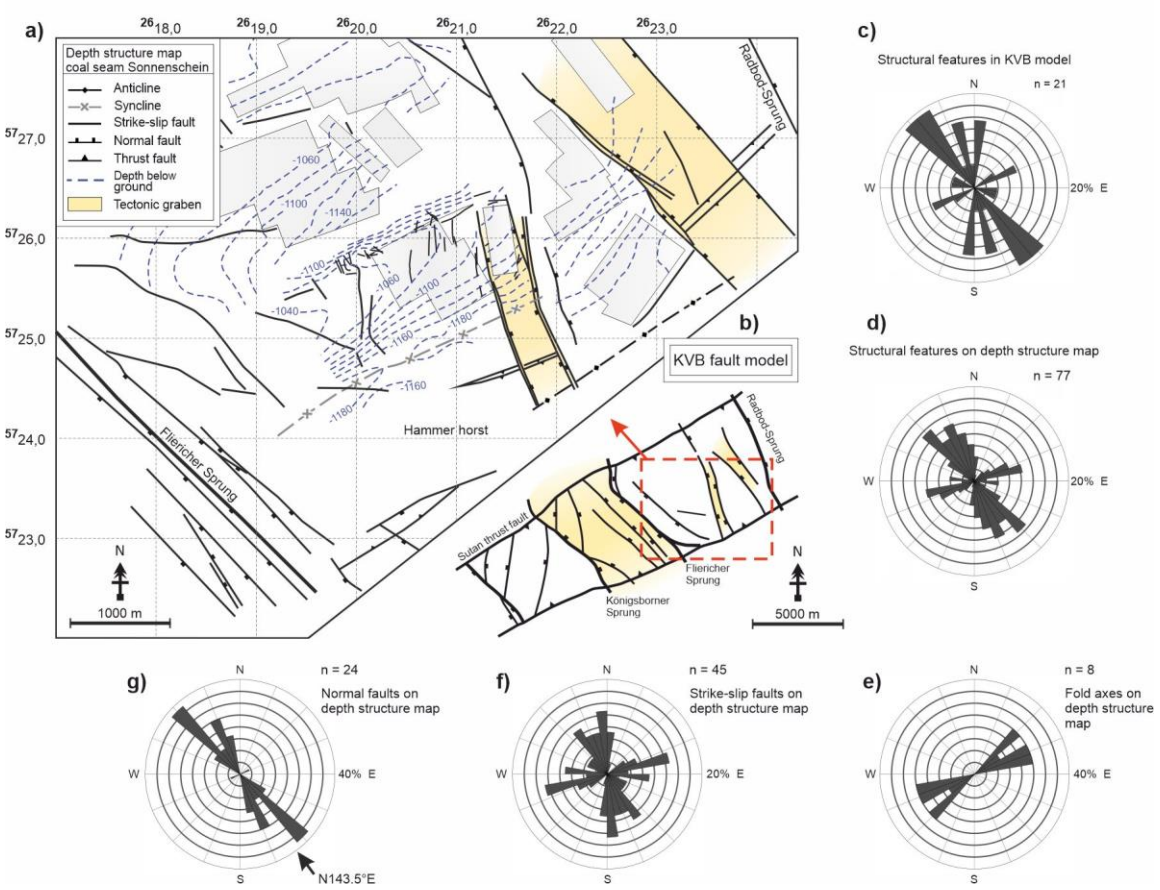

Figure 19: a) Depth structure map of the Sonnenschein coal seam (Bochum fm., Westphalian A) with parts of the mining areas of the "Heinrich Robert" colliery, shown as shaded polygons (CRS: Gauß-Krüger zone 3). b) 2D top view of the constructed fault model based on the KVB model. c) Structural features of the 3D fault model are plotted on a Rose diagram. d) Orientation statistics of the identified structures on the depth structure map. e) Isolated plot for fold axes and thrust faults observed on the depth structure map striking ENE-WSW to NE-SW. f) Strike-slip fault orientation statistics show NW-SE to N-S and E-W trends. g) Normal faults mapped on the depth structure map generally strike NW-SE to NNW-SSE.

3.5.2 Fault slip assessment

A deterministic slip tendency analysis was performed for the constructed fault model, considering an average σ_{Hmax} orientation of N156°E and hydrostatic pore pressure conditions (Figure 20a). Within the normal faulting regime, slip tendency is highest for σ_{Hmax} parallel fault trends (here roughly NNW-SSE) with dip angles of 60° and generally lowest for ENE-WSW strike direction (Figure 20b). Thus, NW-SE to NNW-SSE trending normal faults exhibit highest slip tendencies of the study area's structural inventory, with slip tendencies ranging from 0.02 to 0.37. Thrust faults striking NE-SW to WSW-ENE exhibit the lowest slip tendencies due to their perpendicular alignment in relation to the horizontal compression.

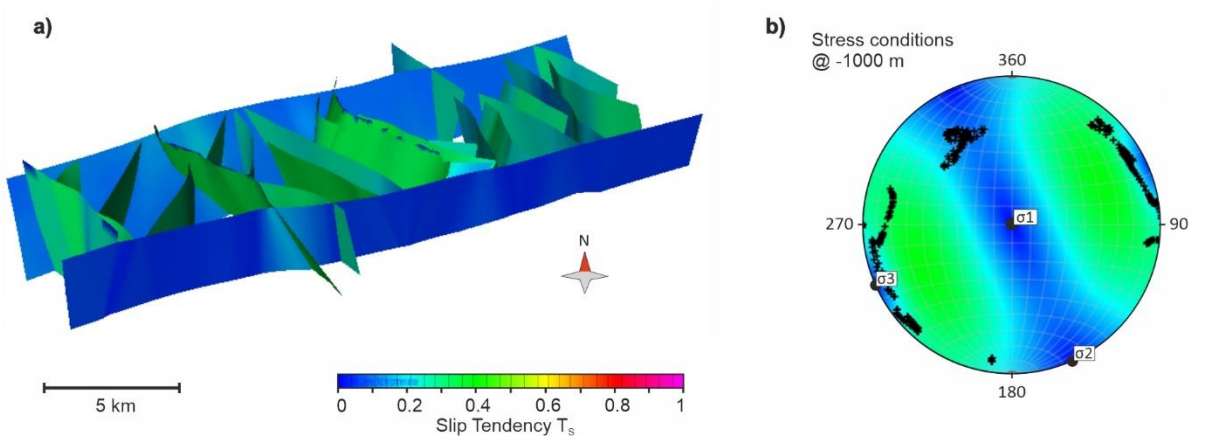

Figure 20: a) Calculated slip tendency color coded on the constructed fault model. b) Stereo plot with fault poles indicating NW-SE to NNW-SSE trending normal faults to be subject to highest slip tendencies.

Slip tendency is probabilistically assessed (1000 Monte Carlo realizations) considering two pore pressure scenarios, for a referential depth of 1000 m below ground, representing former hard coal mining levels. Considering the highest slip tendencies are observed for NW-SE to NNW-SSE trending normal faults (Figure 20b), we use the von Mises orientation statistics of the mapped normal faults (mean = 143.5°, κ = 16.9) from the depth structure map around the "Heinrich Robert" colliery as input (Figure 21e), as this part is subject to mine flooding since 2020. With no data available on the dip angle of the mapped faults, a von Mises distribution is assumed, described by a mean dip value of 60° and a shape parameter κ of 200 (Figure 21f). The stress field data (gradients and σ_{Hmax} orientation) are taken as described in the methods section (Figure 21a, b, c, d).

Considering the expected mine water rebound with water levels to rise up to approximately 640 m below ground, pore pressure amounts to 3.7 MPa at 1000 m below ground. Effective principal stresses amount to $\sigma_{V,eff}$ = 19.9 MPa, $\sigma_{Hmax,eff}$ = 17.7 MPa and $\sigma_{hmin,eff}$ = 12.8 MPa (Figure 22a). Slip tendency results range from 0.05 to 0.44 (Figure 22c), with no slip tendency exceeding the referential frictional strength threshold of either μ = 0.5 nor μ = 0.67 (Figure 22c, d).

Considering hydrostatic pore pressure conditions (P_P = 10.4 MPa) at a depth level of 1000 m below ground (Figure 22h), effective principal stresses comprise $\sigma_{V,eff}$ = 13.2 MPa, $\sigma_{Hmax,eff}$ = 11.0 MPa and $\sigma_{hmin,eff}$ = 6.2 MPa (Figure 22b). Slip tendency results range from 0.01 to 0.91, with 19 % of the slip tendency realizations exceeding the referential frictional strength for Carboniferous shales of μ = 0.5 (Figure 22d, e). Furthermore, 5 % of the slip tendency result exceed the frictional strength criterion for fractured Ruhr sandstone of μ = 0.67 (Figure 22d, e).

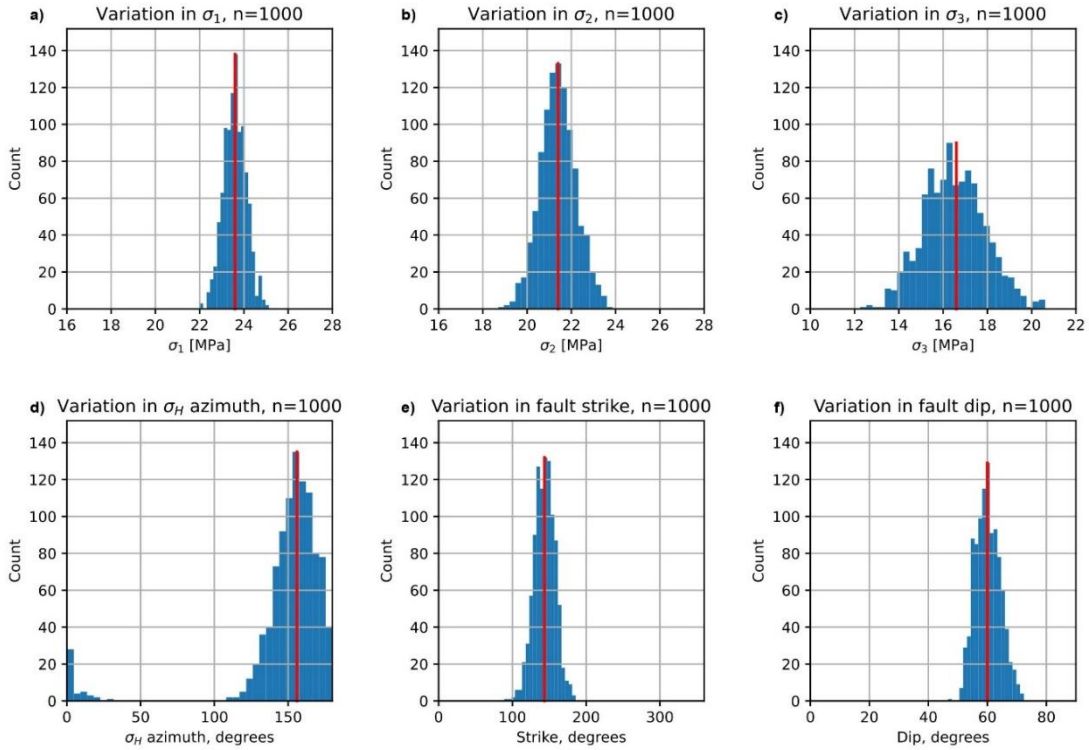

Figure 21: a), b), c) Absolute principal stresses σ_1 (σ_v), σ_2 (σ_{Hmax}) and σ_3 (σ_{hmin}) as input parameters for the probabilistic fault slip assessment given as distributions. The mode value is indicated by the red line. d) Orientation statistics for the maximum horizontal stress component. e) The normal fault strike distribution is derived from the analysis of the depth structure map of coal seam Sonnenschein. f) As dip angle could not be measured for the mapped normal faults, the distribution is assumed.

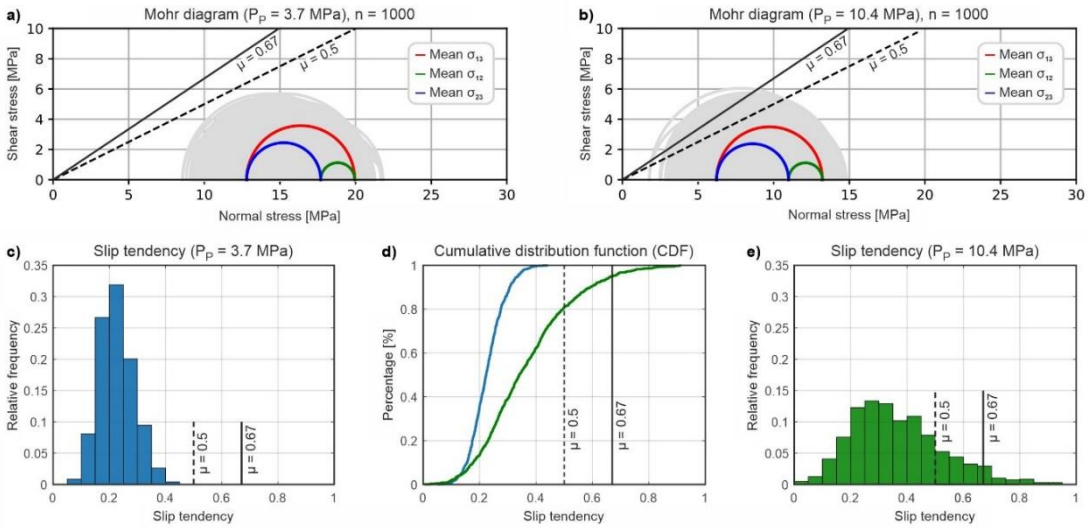

Figure 22: a) Stress conditions for a referential depth of 1000 m below ground assuming a pore pressure of 3.7 MPa, representing a mine water level at 640 m below ground. The failure envelopes are not touched by the Mohr circles. b) Considering full hydrostatic conditions, the Mohr circles partially cross the failure envelopes. c) Slip tendency calculated for the analyzed set of NNW-SSE to NW-SE trending normal faults do not exceed the friction coefficients. d) Cumulative distribution functions (cdf) of the calculated slip tendencies for both pore pressure scenarios. Blue color refers to c); green color refers to e). e) Slip tendency distribution for hydrostatic conditions, partially exceeding the friction coefficients.

3.5.3 Distance-to-failure analysis

The Upper Carboniferous sequence of the Bork 10 well (650 m to 1000 m MD) is used as data input for property modeling, since it partially covers the stratigraphy of the study area. The lithological column comprises alternating sandstone and claystone beds of variable thicknesses (up to 20-40 m), occasionally containing interbedded coal seams (Figure 23a). The gamma ray log response matches the lithological core description (Figure 23a). The constructed geomodel covers the vertical extent of available well log information and consists of multiple zones to honor the vertical lithological architecture. This is reflected in the V_{sh} property model (Figure 23b), with V_{sh} values ranging from 0 to 100 % (Figure 23c). Spatially, the model comprises of a section of a NNW-SSE trending normal fault located on the Hammer horst structure, previously identified as the fault trend most susceptible to reactivation. Fault throw increasing towards SSE, as the fault is only partially modeled since it extends beyond the boundaries of the structural 3D model.

The predicted clay content (V_{sh}) along the fault of interest (using the ESGR algorithm) ranges in between 0 and 100 %, following a normal distribution character (Figure 23d, e). Generally, the V_{sh} property is heterogeneously distributed over the modeled fault surface, with characteristic elongated patches of higher and lower clay content (Figure 23d, e). Lowest predicted V_{sh} values are attributed to sandstone-sandstone juxtapositions. Consequently, the resulting spatial distribution of the friction coefficient follows the observed V_{sh} pattern (Figure 23f). Thus, elongated fault patches of various friction coefficient magnitudes are characteristic. The modeled friction coefficient distribution ranges from 0.28 to 0.72 with a mean of 0.47 (Figure 23g).

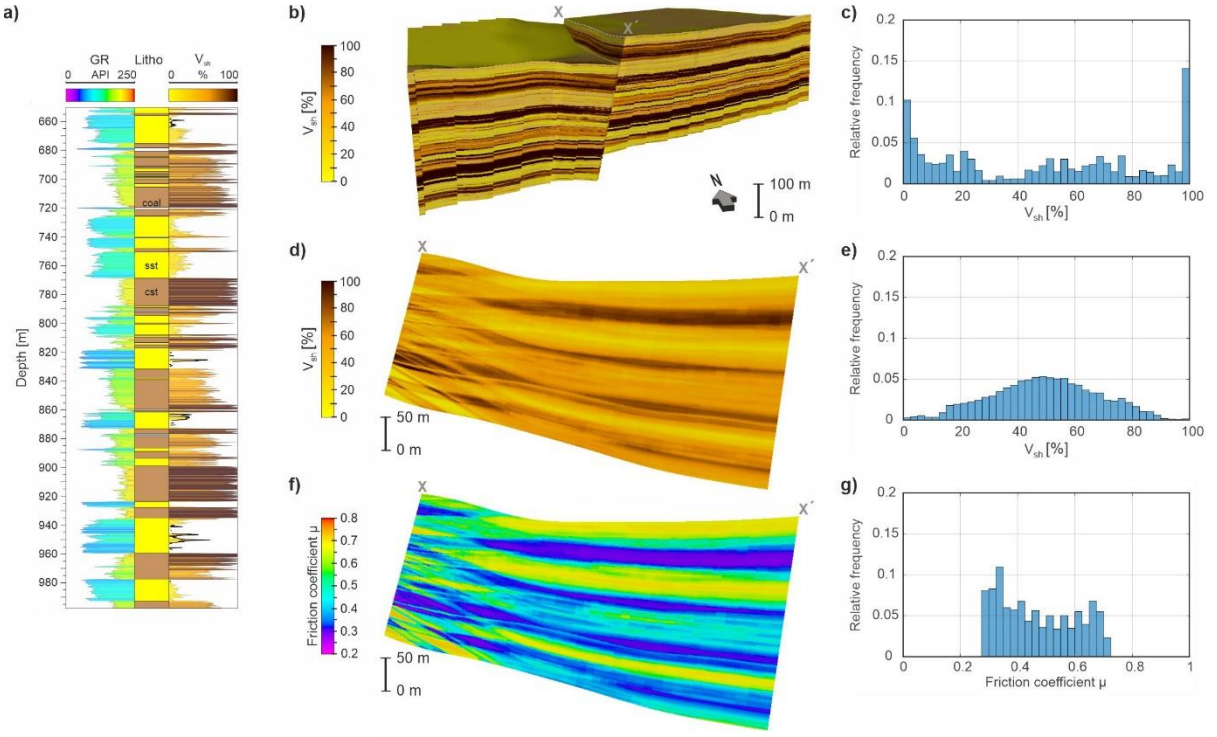

Figure 23: a) The analyzed Upper Carboniferous succession consists of sandstone (sst) and claystone (cst) beds of various thickness with interbedded coal seams. Gamma ray log and corresponding V_{sh} log are displayed. A discrete litho-log is derived from core description. b) The V_{sh} property model is build-up of multiple zones to reflect the characteristic lithological architecture of the analyzed Upper Carboniferous succession (1.5 times vertical exaggeration). c) The V_{sh} distribution of the property model is based on the upscaled well data, reflecting the lithological composition. d) The predicted fault clay content property (V_{sh}) shows a heterogeneous pattern of elongated patches (1.5 times vertical exaggeration), with the associated distribution following a normal distribution character (e). f) The modeled spatial distribution of the friction coefficient follows the fault clay content (V_{sh}) pattern (1.5 times vertical exaggeration), with values ranging from 0.28 to 0.72 (g).

Fault stability is assessed by quantifying the Failure Criterion Stress (FCS) on the assumption of hydrostatic pore pressure conditions, using the same stress field dataset as for the probabilistic fault slip assessment. The approach of assuming two constant frictional fault strength thresholds ($\mu = 0.5$ and $\mu = 0.67$, as used in the fault slip assessment) is compared to the approach of modeling the spatial variability of the friction coefficient (Figure 24a, b, c, d).

For constant friction coefficients, the resulting Failure Criterion Stresses (FCS) are negative with values ranging from -0.95 to -1.15 MPa (for a $\mu = 0.5$) and -1.96 to -2.24 MPa (for a $\mu = 0.67$) respectively, indicating stable conditions (Figure 24a, c, e).

Considering the geologically more realistic scenario, the friction coefficient for every point on the fault is derived as a function of the predicted fault clay content (V_{sh}) (Figure 24b). Horizontal patches of positive FCS are associated with lower friction coefficients and thus, higher clay contents (V_{sh}), reaching up to 0.65 MPa (Figure 24b, g). Negative FCS values range down to -2.43 MPa (Figure 24b, g), with 72.6 % of the modeled fault below the critical FCS threshold of 0 MPa (Figure 24f). These stable zones are linked to intermediate to high friction coefficients and thus, intermediate to low clay contents (V_{sh}).

Fully stable conditions are reached when additionally considering fault rock cohesion (1 MPa) (Figure 24d). The resulting FCS values range between -0.31 and -3.24 MPa (mean of -1.67 MPa), spatially distributed along the same characteristic elongated patches (Figure 24d), without exceeding the critical FCS threshold of 0 MPa (Figure 24f, g).

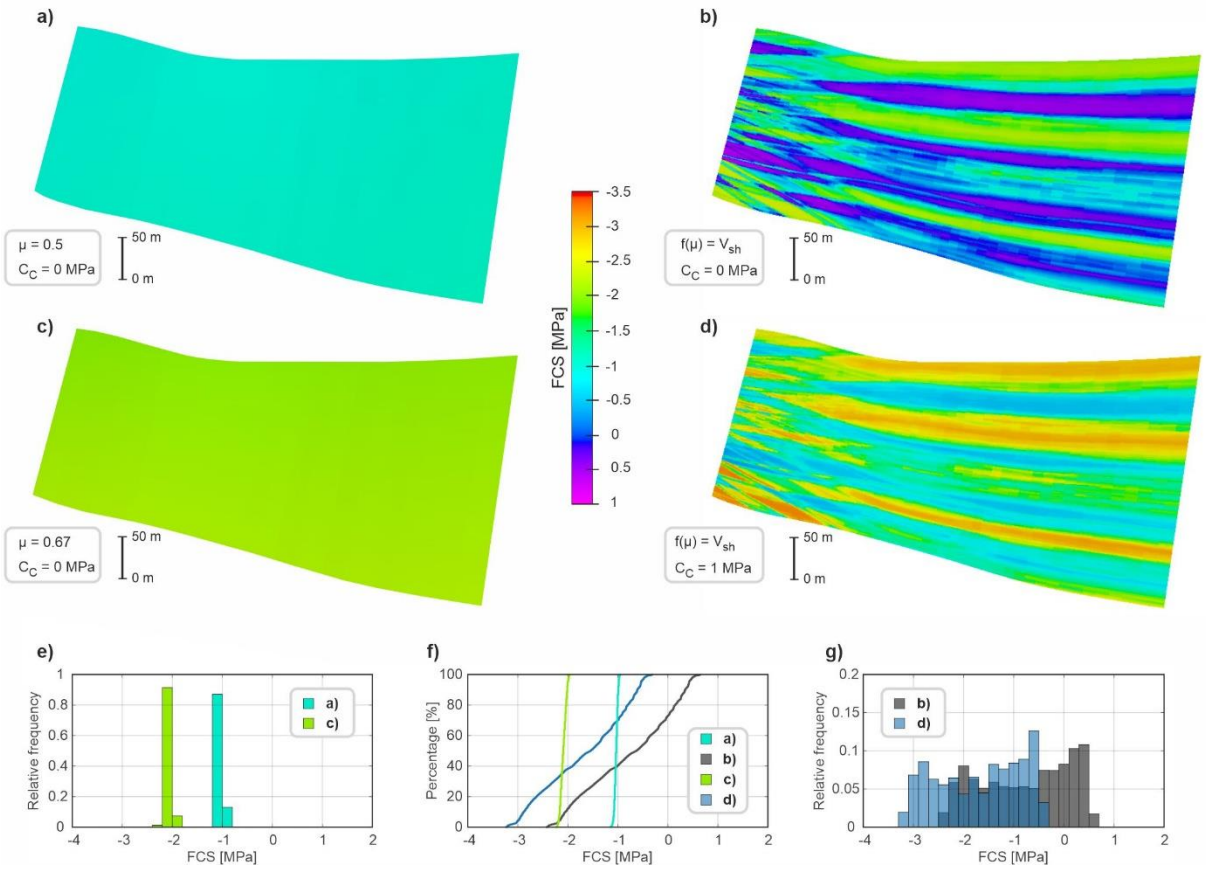

Figure 24: Frictional Criterion Stress (FCS) results for considering constant friction coefficient of μ = 0.5 (a) or μ = 0.67 (c) compared to the predicted frictional strength for cohesionless (b) and cohesive conditions (d). e) Resulting FCS values range from -0.95 to -1.15 MPa (μ = 0.5) and -1.96 to -2.24 MPa (μ = 0.67) assuming constant friction coefficients, without exceeding the critical FCS threshold of 0 MPa. f) Cumulative distribution functions color-coded for all four scenarios. g) FCS distributions for both scenarios of modeled spatially heterogeneous frictional fault strength.

3.6 Discussion

3.6.1 Structural model

The constructed 3D model represents the structural configuration of the study area water province "Haus-Aden". As data basis, the 2.5-dimensional KVB model is associated with a limited three-dimensional resolution, since the coal seams were vertically interpolated following a geometric approach (Juch 1996) and thus, does only locally rely on hard-data. However, it provides a three-dimensional impression of the structural configuration of a tight reservoir analogue based on subsurface mapping in coal mines. Analysis of the depth structure map (Sonnenschein coal seam) provides additional insight into the fault zone architecture of the NE border fault of the Königsborner Graben (Fliericher Sprung). As fault zones

are represented as discrete planar surfaces for the sake of reservoir modeling, detailed depth structure information indicates a complex fault zone architecture comprising several syn- and antithetic fault segments, in alignment with fault zone examples worldwide (Caine et al. 1996; Childs et al. 2009; Richard et al. 2014; Delogkos et al. 2017). However, this level of structural detail is not resolved in the structural 3D model.

Due to decades of active coal mining exploration and exploitation, a significant amount of legacy data has been acquired, which could potentially be employed for future subsurface utilization such as geothermal energy extraction from mine waters (Greve et al. 2023). Therefore, the methodology developed in this study could be applied for deriving 3D models of the deeper subsurface for the vertical extent of available data. This cost-effective exploration option allows for the assessment of the target area's overall structural configuration prior to committing to cost-intensive 3D seismic data acquisition.

3.6.2 Fault slip assessment

The slip tendency analysis for the tectonic inventory of the constructed 3D model revealed NW-SE to NNW-SSE trending normal faults to experience highest slip tendencies. The probabilistic fault slip assessment performed for the identified NW-SE to NNW-SSE trending normal fault set considered two pore pressure scenarios (P_P of 3.7 MPa or 10.4 MPa) to cover the range of possible in situ pore pressure states. Taking into account a mine water level of 640 m below ground and a resulting pore pressure of 3.7 MPa at 1000 m below ground, the calculated slip tendencies do not exceed the friction coefficients. For hydrostatic conditions, 19 % of the Monte Carlo simulations exceed the frictional strength criterion for Carboniferous shales. However, the frictional strength of fractured Ruhr sandstone of $\mu = 0.67$ is exceeded in only 5 % of the realizations, which is the case for highest differential stresses ($\sigma_d > 7$ MPa).

The performed fault slip assessment assumed only frictional resistance to sliding as faults are considered as incohesive. However, postseismic fault healing by fluid-rock interactions can lead to cohesive strengthening of fault rocks (Tenthorey and Cox 2006; Casas et al. 2022). As fault rock cohesion would additionally stabilize the analyzed faults, the chosen approach can be considered as conservative. A heterogeneous spatial distribution of the frictional fault strength is likely, depending on the faulted lithologies and along-strike throw distribution (Meng et al. 2017; Jin et al. 2023) as the phyllosilicate content of the fault gouge controls the frictional strength (Takahashi et al. 2007; Kohli and Zoback 2013; Meng et al. 2017; Hunfeld et al. 2017; Bedford et al. 2022). This could be demonstrated exemplary for a selected fault by the application of a non-perfect clay mixing model (ESGR) with the modeled friction coefficient varying spatially along the fault surface.

The ESGR modeling result indicates a heterogeneous clay content distribution along the fault characterized by horizontally elongated patches. However, sandbox modeling results of Vrolijk et al. (2016) show unstructured patterns of clay mixing along the fault surface, which cannot be resolved using the ESGR approach. The same applies to fault outcrop observations in a mixed Carboniferous sandstone shale sequence, where rapid variation in fault rock content is described (Childs et al. 1997). Furthermore,

unresolved fault zone architectural complexity challenges the application of deterministic clay mixing models (Childs et al. 1997). As such, the employed ESGR approach provides an improved resolution of the spatial change in the frictional fault strength, albeit considering the mentioned limitations. Consequently, this questions the application of a single friction coefficient for fault slip assessments. Considering the spatial variability of frictional fault strength is crucial, particularly as the heterogeneity of fault gouge clay content along faults can lead to an overall reduction in fault strength, as demonstrated by Bedford et al. (2022).

While the employed function $f(\mu) = V_{sh}$ is not derived from a measurement campaign specific to the studied Upper Carboniferous lithologies, the function converges to a value of $\mu = 0.72$ for the 0 % V_{sh} endmember, aligning with experimentally measured friction coefficient for fractured Ruhr sandstone ($\mu = 0.67$) (Kruszewski et al. 2021).

Distance-to-failure analysis, based on the generated friction coefficient model, highlights that the analyzed fault is characterized by stable (FCS < 0, 72.6 %) and unstable (FCS > 0, 27.4 %) zones, assuming no cohesive fault strength is considered. Here, fault stability is directly controlled by the spatial distribution of the friction coefficient. Unstable zones (FCS > 0) are spatially linked to lower friction coefficients, while stable fault patches (FCS < 0) are associated with intermediate to high friction coefficients. However, when additionally considering a cohesive fault strength (1 MPa), the entire modeled fault reaches stable stress conditions.

While unstable zones (FCS > 0) imply an existing potential for fault reactivation, it remains unclear to what extent stabile fault patches (FCS < 0) contribute to the stabilization of the fault. If unstable zones were to trigger fault reactivation, these low frictional strength zones might be dominated by aseismic creep rather than seismic slip, as high clay content fault gouges often show rate-strengthening frictional behavior (Ikari et al. 2009; Kohli and Zoback 2013; Collettini et al. 2019; Bigaroni et al. 2022; Ashman and Faulkner 2023). The proposed workflow for modeling the spatial variability of the frictional fault strength offers an approach to study fault stability based on a geologically more realistic frictional fault strength model, compared to the consideration of a single constant friction coefficient.

Generally, the mining areas were spatially bounded by major fault zones where the in situ pore pressure in the vicinity of the faults is unknown, as no measurements have been conducted. If the area surrounding the faults was influenced by mine water management and thus also by the expected mine water rebound, pore pressures below hydrostatic conditions are conceivable (P_P 3.7 MPa at 1000 m below ground). Therefore, fault slip is unlikely as probabilistically computed slip tendencies do not reach the proposed failure criteria.

If faults were not influenced by mine drainage, hydrostatic pore pressure conditions are conceivable since the hydraulically tight Upper Carboniferous rock matrix (Greve et al. 2023) could have delayed pore pressure re-equilibration between high and low pressure zones. However, this assessment neglects the influence of fracture networks in the Upper Carboniferous lithologies (Allgaier et al. 2023) on fluid

distribution in the subsurface. With respect to the effective mean principal stresses, fault slip is not likely for the considered range of frictional fault strength. In case of high differential stresses, fault slip might be possible. However, potential cohesive fault rock strength is not considered here and provides additional safety buffers. This is in agreement with stability analysis performed for an exemplary fault, based on a spatially heterogeneous frictional fault strength model. Most of the modeled fault is stable (FCS < 0), with fault stability being improved by assuming cohesive strength.

Overall, the fault slip assessment indicates fault slip for NW-SE to NNW-SSE trending normal faults within the NE part of the water province “Haus Aden” to be unlikely within the present-day stress field. This is in alignment with the German seismic hazard map (Gruenthal and Bosse 1996), indicating no natural fault activity to be expected.

3.7 Conclusion

A structural 3D model of the NE part of the water province “Haus Aden” (eastern Ruhr Basin) has been constructed utilizing 2.5-dimensional legacy data. The derived model serves as basis to identify the most exposed fault trends and types of the structural inventory by calculating slip tendency, revealing NW-SE to NNW-SSE trending normal faults.

Probabilistic fault slip assessment revealed no reactivation potential for a mine water rebound up to a level of 640 m below ground. Assuming hydrostatic conditions around the faults, NW-SE trending normal faults exceed the failure threshold only partially for high differential stresses ($T_S > \mu = 0.67$ in 5 % of the cases; $T_S > \mu = 0.5$ in 19 % of the cases).

This aligns with fault stability analysis conducted for an NNW-SSE trending fault within the study area, utilizing a spatially heterogeneous frictional fault strength model. The results indicate that the majority of the modeled fault is stable, with the fault being characterized by a mixture of stable patches (FCS < 0) and unstable zones (FCS > 0). Enhancements to the conventional approach of using a single friction coefficient for fault stability analysis might be achieved by adopting the proposed workflow, which models the spatial heterogeneity of the frictional fault strength through the application of a non-perfect clay mixing model

4 Fault leakage and reservoir charging in the Upper Rhine Graben, Germany – Assessment of the Leopoldshafen fault bend

4.1 Abstract

Faults control subsurface fluid flow in sedimentary basins worldwide, often affecting hydrocarbon migration as well as geothermal fluid circulation. Since the Upper Rhine Graben hosts geothermal, lithium brine, and hydrocarbon resources, the role of faults on fluid flow in the basin is of great interest. To better understand structurally controlled fluid flow in the central Upper Rhine Graben, this study investigates the hydrocarbon migration of the fault-related Leopoldshafen oil field. As fault geometry can change along-strike, fault conductivity might also vary spatially as it depends on, among others, the fault orientation relative to the active stress field. Therefore, slip and dilation tendencies are used as proxies for stress-controlled fault conductivity, computed for a strike-slip faulting regime with NW to NNW oriented σ_{Hmax}. Fault Response Modelling is applied to derive subsurface strain distributions, associated with fault activity during the Miocene phase of basin development. The Leopoldshafen fault, as a fundamental element of the fault-related three-way dip closure trap structure, is characterized by a changing along-strike geometry with NNE-SSW trending fault segments linked by a NNW-SSE trending left-stepping fault bend. Slip and dilation tendencies are highest around the fault bend segment, with a range of considered σ_{Hmax} orientations. As Expansion Index analysis indicates across-fault thickening and thus fault activity of the Leopoldshafen fault during the main phase of graben rifting (Late Eocene to Oligocene), subsurface strain distribution pattern associated with Miocene fault activity highlight strain concentrations around the fault bend segment, which has acted as a releasing bend. Thus, based on slip and dilation tendency analyses, as well as Fault Response Modelling, the fault bend segment is identified as the up-fault fluid migration zone along the Leopoldshafen fault. This underscores the importance of comprehending the structural inventory of the Upper Rhine Graben for the prospect of future subsurface exploration and alternative post-oil utilization.

4.2 Introduction

Faults play an important role in extensional sedimentary basins, controlling subsidence, sediment routing, fluid migration and heat transport (Person et al. 1996; Gupta et al. 1998; Gawthorpe and Leeder 2000; Bächler et al. 2003; Michael et al. 2013; Henstra et al. 2016; Walsh et al. 2018). Fault development has been studied intensively, demonstrating the concepts of fault segmentation and linkage (Childs et al. 1995; Cartwright et al. 1996; Peacock 2002; Rotevatn et al. 2019; Fossen 2020) forming complex along-strike fault geometries. Furthermore, the structural control on potential elevated structural permeability

is often linked to fault interactions, fault bends and transfer zones (Faulds and Hinz 2015; Brogi et al. 2021). With respect to strike-slip faults, releasing bends are often associated with enhanced fluid flow and mineralization (Sibson 1996; Muchez and Sintubin 1998; Stephen 2005; Zhang et al. 2008). Additionally, fault-controlled hydrocarbon migration has been studied in detail (Hooper 1991; Moretti 1998; Smeraglia et al. 2022), with fluid flow along faults being sensitive to the prevailing stress field (Barton et al. 1995; Wiprut and Zoback 2000).

In the context of a multi-phase deformation history, the impact of reactivation on normal faults is often studied for reverse, respectively up-dip reactivation (McClay 1989; Chapman and Meneilly 1991; Kelly et al. 1999). Rotevatn and Peacock (2018) investigated the strike-slip reactivation of normal faults, highlighting the implications for fluid flow caused by the presence of either releasing or restraining bends depending on the along-strike geometry of the reactivated normal fault.

The Upper Rhine Graben is an extensively studied Cenozoic intra-continental rift basin with a long history of hydrocarbon and geothermal exploration and production (Schad 1962; Durst 1991; Agemar et al. 2014; Reinhold et al. 2016; Genter et al. 2016), and faults playing an important role for basin-scale fluid migration and heat flow (Bruss 2000; Bächler et al. 2003; Böcker et al. 2017). This is reflected by still ongoing production from oil fields in the Upper Rhine Graben (Durst 1991; Reinhold et al. 2016; Böcker et al. 2017). Natural resource exploration in the region also relies on fault zones at 3 to 5 km depth in sedimentary as well as crystalline rocks for deep geothermal exploration and aims for lithium brine mining from geothermal waters (Baujard et al. 2021; Fries et al. 2022).

This work uses the geomechanical concepts of slip and dilation tendency as proxies to identify locations along the Leopoldshafen fault which might have acted as fluid migration pathways. First, we will construct a 3D geological model on which we conduct slip and dilation tendency analysis. Then, we will perform Fault Response Modelling to provide additional insights in the spatial distribution of subsurface strain induced by transtensional strike-slip reactivation of the Leopoldshafen fault within the Miocene stress field. Subsequently, the fault-controlled charging of the stacked Leopoldshafen oil reservoirs and potential geothermal utilization will be discussed, considering the interactions of stress- and fault orientations which may benefit the future successful exploration and utilization of the subsurface.

4.3 Geological Setting

The study area is located within the central part of the Upper Rhine Graben between Karlsruhe and Heidelberg, Germany (Figure 4.1a, b). The overall NNE-SSW striking passive continental rift is bound by major normal faults to the east and west and can be spatially subdivided into a northern, central and southern part (Schumacher 2002) (Figure 4.1b). The 300 km long and 40 km wide Upper Rhine Graben is part of the European Cenozoic rift system, which extends over 1100 km from the North Sea to the Mediterranean Sea (Schumacher 2002; Meschede and Warr 2019) (Figure 4.1a).

The crystalline basement was overprinted by the Variscan Orogeny with Late Carboniferous extension leading to the formation of WSW-ENE striking intramontane basins, where eroded material was deposited until the late Permian (Illies 1972; Ziegler and Dèzes 2005; Eisbacher and Fielitz 2010). A NNE-SSW striking fault system was set in place during Variscan times and is related to Permian volcanism (Illies 1978; Schumacher 2002; Edel et al. 2007).

The Mesozoic pre-rift series, comprising of Triassic and Jurassic age sedimentary rocks, was deposited on the peneplained Variscan orogen, unconformably overlying the Permian sedimentary rocks and the older crystalline rocks (Schumacher 2002). The Mesozoic pre-rift sediment series was deposited under marine and continental conditions. While terrestrial depositional conditions prevailed in the Lower Triassic Buntsandstein (Induan to Early Anisian) (Aigner and Bachmann 1992; Bourquin et al. 2006; Meschede and Warr 2019), the transgressive Middle Triassic Muschelkalk (Early Anisian to Early Ladinian) period was characterized by a shallow marine environment (Aigner and Bachmann 1992; Warnecke and Aigner 2019; Meschede and Warr 2019) that changed to terrestrial conditions in the Upper Triassic Keuper (Early Ladinian to Rhaetian) (Aigner and Bachmann 1992). The Triassic is followed by the transgressive phase of the Jurassic, where marine conditions prevailed throughout South Germany and led to the deposition of mainly limestones, marls, and dolomites (Pienkowski et al. 2008). Important Jurassic age source rocks comprise the Lias α and the Posidonia Shale (Lias ε) with oil shales and bituminous marls characterized by good to excellent source rock potential in the Upper Rhine Graben (URG) (Schad 1962; Bruss 2000).

Sedimentation of the Cenozoic syn-rift sequences was controlled by tectonic activity as well as by transgressive phases (Derer et al. 2005; Perner et al. 2018). The Oligocene and Miocene syn-rift sequence comprises mostly of fine-grained sediments with intercalated sand layers (Reinhold et al. 2016). Coarser sediments were deposited along the rift-basin margins (Derer et al. 2005) with sedimentation and palaeoenvironmental conditions being controlled by syn-sedimentary fault activity of the boundary faults (Derer et al. 2005; Reinhold et al. 2016; Perner et al. 2018). Sedimentation of the Oligocene and Miocene syn-rift series was controlled by several transgressive phases alternating with continental sedimentation conditions (Berger et al. 2005b; Berger et al. 2005a) (Figure 4.2). Generally, the transgressive sequences represent the main Cenozoic source rock unit of the rift-basin (Perner et al. 2018).

The development of the Cenozoic Upper Rhine Graben is associated with a changing stress field and the reactivation of deep-ranging Permo-Carboniferous NNE-SSW trending fault systems (Ziegler 1990, 1992; Schumacher 2002). The main rift phase of the Upper Rhine Graben took place during the Oligocene, when the evolving Upper Rhine Graben was subject to W-E to WNW-ESE extension (Buchner 1981; Schumacher 2002; Dèzes et al. 2004). A major reorientation of the stress field during the Miocene caused by the Alpine orogeny, led to a sinistral strike slip movement along the boundary faults of the Upper Rhine Graben in response to the NNW-SSE to NW-SE oriented direction of the maximum principal stress σ_1 (Illies 1978; Buchner 1981; Schumacher 2002; Dèzes et al. 2004). Therefore, NNE-SSW

trending main faults within the Upper Rhine Graben have also been reactivated in the same shear sense (Rotstein et al. 2005). As a result, the central part of the Upper Rhine Graben is acting as restraining bend (Schumacher 2002).

The structural style of the Upper Rhine Graben is characterized by complex horst and graben structures, formed by antithetic and synthetic normal faults (Durst 1991) (Figure 4.1d). The tectonic inventory is influenced by the multiphase Cenozoic deformation history. Main rifting in the Oligocene occurred in response to W-E to WNW-ESE extension in a normal faulting stress regime and involved the formation of NNE-SSW trending graben-parallel faults with fault lengths up to tens of km. Miocene deformation occurred in a strike-slip stress regime, dominated by sinistral strike-slip kinematics and formation of smaller faults with overall NNW-SSE strike direction. While the major NNE-SSW trending faults often displace the whole Cenozoic sequence, the NNW-SSE oriented faults abut against these major faults (Reinhold et al. 2016). Generally, the Upper Rhine Graben is structurally characterized by a cross-sectional asymmetry, with higher subsidence observed at the eastern side of the central Upper Rhine Graben (Figure 4.1d). Subsidence patterns vary within the rift basin with a few hundred meters' difference between structural highs and lows even within the graben center (e.g. Illies 1972, Boigk 1981) affecting reservoir quality (Busch et al. 2022b).

The present-day stress field (direction of principal stresses and magnitudes) for the central part of the Upper Rhine Graben derived from wellbore data at the Bruchsal geothermal site is described as a normal faulting regime with a transition to strike-slip, with σ_{Hmax} striking roughly NW-SE (Meixner et al. 2014). Generally, the Upper Rhine Graben is characterized by low- to medium intra-plate seismicity (Peters et al. 2005), with lower seismic activity observed for the central part (Doubre et al. 2021).

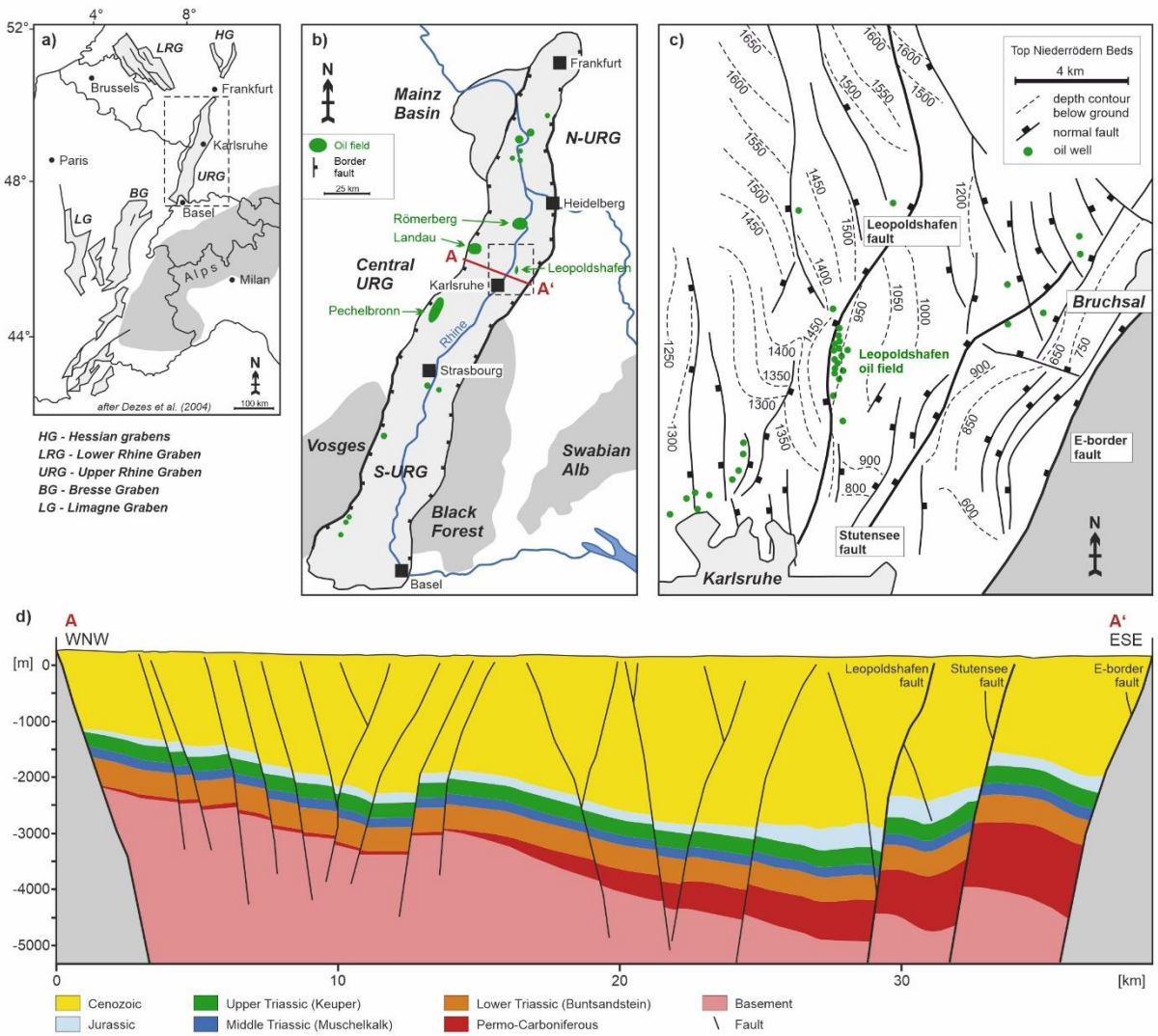

Figure 4.1: a) Simplified map of the European Cenozoic Rift System with rift-related sedimentary basins highlighted in light grey (modified after Dèzes et al. (2004)). b) The Upper Rhine Graben is subdivided into a southern, central and northern part, with the study area located N of the city of Karlsruhe (modified after Böcker et al. (2017)). Prominent oil fields are marked in green. c) Depth structure map of the Top Niederröderner beds with contour lines given as depth below ground level (after Sauer and Nägele (1981)). The Leopoldshafen wells targeting the Cenozoic in the footwall of the Leopoldshafen fault are shown in green. d) WNW-ESE oriented cross-section (2x vertical exaggeration) through the central Upper Rhine Graben reveals the asymmetric style of the rift basin (LGRB-Kartenviewer 2021).

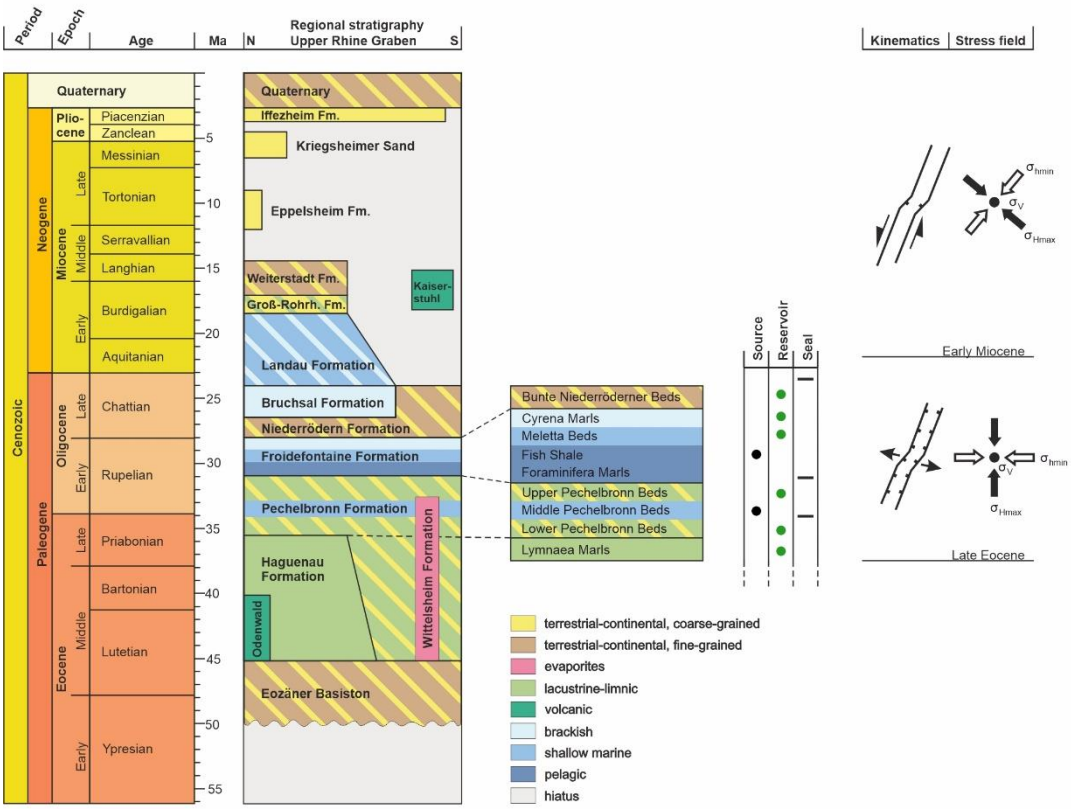

Figure 4.2: Stratigraphy of graben fill and associated depositional environment (after Deutsche Stratigraphische Kommision 2016). Elements of the the Cenozoic petroleum system of the central Upper Rhine Graben (after Reinhold et al. (2016) and Böcker et al. (2017)) without the Jurassic source rocks displayed in the figure. The multiphase deformation history of the Upper Rhine Graben is taken from Dèzes et al. (2004).

4.3.1 Leopoldshafen oil field

This study focuses on the former Leopoldshafen oil field, which produced a total of 1,481,953 bbl from 1957 to 1986 (Reinhold et al. 2016). The considered field is located approximately 10 km north of the city of Karlsruhe (Figure 4.1b). As a fault-related trap (Durst 1991; Reinhold et al. 2016), the Leopoldshafen oil-field is characterized as a three-way dip closure, bounded by the Leopoldshafen fault to the west (Reinhold et al. 2016) (Figure 4.3). Bruss (2000) identified Jurassic (Liassic black shales) and Cenozoic (Fish shale) source rocks to feed a multi-level reservoir system with producing units located in the Rupelian Cyrena Marls, Meletta Beds as well as the Chattian Bunte Niederröderner Beds (Boigk 1981; Durst 1991) (Figure 4.3). In case of the Meletta sandstone beds from the Froidefontaine Fm. the reservoir rocks comprise laterally confined sandstone bodies, with a vertical extent of up to 5 m separated by marl (Boigk 1981). Reservoir quality of the laterally limited Meletta sandstone bodies (Meletta Beds) is made up of variable porosity (Φ: 8.7 -25.6 %) and permeability (κ: 1.3 – 64 mD) (Sauer and Nägele 1981). Böcker et al. (2017) concluded on the basis of geochemical analyses, that Liassic oil (Lias ε, respectively Posidonia Shale) accounts for the major part of the Leopoldshafen oil admixture. According to Reinhold et al. (2016) and Böcker (2017), the main phase of Liassic oil expulsion took place in the Miocene. Significant kitchen areas are located in the graben center around Karlsruhe, with the

Posidonia Shale (Lias ε) reaching the wet gas window, indicated by a vitrinite reflectance of VR_r > 1.3 % (Böcker and Littke 2016). Hydrocarbon charge might be fault-controlled (Bruss 2000) while transgressive intra-formational sequences are believed to form major seals (Böcker et al. 2017).

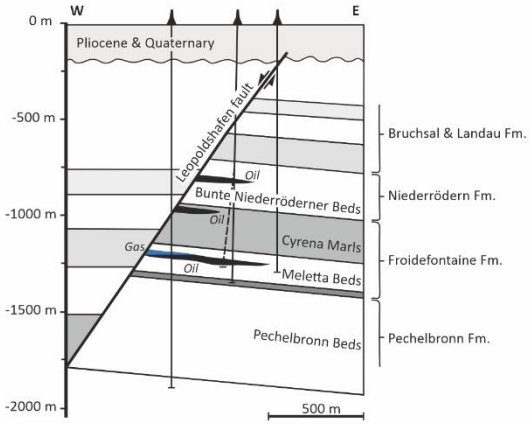

Figure 4.3: Schematic profile through the Leopoldshafen oil field with the hydrocarbon accumulation in the footwall (after Wirth (1962)).

4.4 Materials and Methods

4.4.1 Geomodel

The fundamental structural framework of the Leopoldshafen site is derived from regional-scale depth maps of several Cenozoic (Base Landau Fm., Base Froidefontaine Fm. & Base Tertiary) and Mesozoic (Base Keuper & Base Muschelkalk) stratigraphic horizons as part of the GeORG data set (Sokol et al. 2013). Initiated by the geological surveys of Germany (Baden-Württemberg, Rhineland-Palatinate), France and Switzerland, the regional scale 3D model of the Upper Rhine Graben (GeORG) has been constructed, based on seismic data, borehole information and depth structure maps (Sokol et al. 2013). Furthermore, the Leopoldshafen 1 well report, available at the LGRB (federal geological survey of Baden-Württemberg), was used to constrain the vertical extent of the reservoir zone. Results were evaluated against older 2D depth structure map data of the field, which allowed for the comparison of strike and dip direction of the Leopoldshafen fault considered in this study (Sauer and Nägele 1981). The authors are aware that the GeORG data come with limitations as compared to unpublished 3D seismic acquired by Rhein Petroleum GmbH in 2012 (Deutsche Rohstoff 2012), which will be discussed below.

4.4.2 Expansion index analysis

To better understand the fault activity of the Leopoldshafen fault, the Expansion Index (EI) established by Thorsen (1963), is used to identify periods of fault growth (Pochat et al. 2009; Jackson and Rotevatn 2013; Cong et al. 2020). Defined as the ratio of thickness variation between foot- (FW_t) and hanging wall (HW_t), an EI > 1 indicates across-fault thickening and thus, fault activity during sediment deposition.

$$EI = \frac{HW_t}{FW_t} \tag{1}$$

4.4.3 Slip & dilation tendency analysis

To identify the location of fault-controlled fluid migration pathways, slip and dilation tendency are used as proxies, calculated with the Stress Analysis tool of the MOVE Software Suite (Petroleum Experts Ltd.).

Slip tendency T_S is utilized to identify critically stressed fault segments, which could potentially be permeable under certain stress conditions (Barton et al. 1995; Wiprut and Zoback 2000). Based on effective principal stresses, the slip tendency T_S (not normalized with respect to μ) is computed as the ratio of resolved shear (τ) to normal stress (σ_n) acting on a surface of interest. A fault is considered as critically stressed if its slip tendency values exceed the coefficient of static friction (μ). The slip tendency T_S describes the likelihood for a cohesionless fault to be reactivated in shear mode (Morris et al. 1996):

$$T_s = \frac{\tau}{\sigma_n} \geq \mu \tag{2}$$

Dilation tendency T_D gives the likelihood of a surface to dilate, respectively to open, in tensile mode (Ferrill et al. 1999):

$$T_D = \frac{\sigma_1 - \sigma_n}{\sigma_1 - \sigma_3} \tag{3}$$

Slip and dilation tendency cross-plots are utilized to analyse failure behavior along the modeled fault surface and associated implications for volume changes, following the approach of Ferrill et al. (2020a) (Figure 4.4).

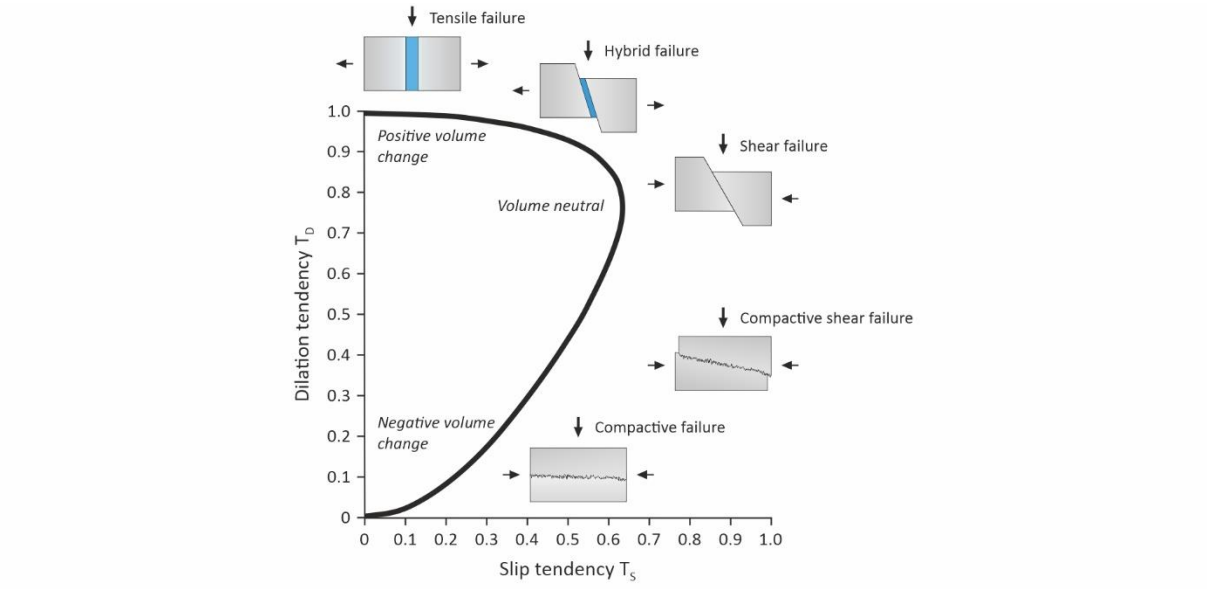

Figure 4.4: Slip and dilation tendency cross-plot linked with failure modes and implications for volume changes (modified after Ferrill et al. (2020a)).

The Miocene stress field is characterized as a strike-slip faulting regime, inducing left-lateral reactivation of favorably oriented faults (Illies 1978; Buchner 1981; Schumacher 2002; Dèzes et al. 2004). Schumacher (2002) describes a σ_{Hmax} (σ_1) orientation of NNW-SSE (N158°E) for the Early Miocene, which rotates towards NW-SE (N135°E). Rotstein and Schaming (2011) proposed a NNW-SSE (N158°E) oriented σ_{Hmax}, while Buchner (1981) suggest NW-SE (N135°E) oriented horizontal compression. To account for the possible σ_{Hmax} orientations, three scenarios (N135°E, N146°E, N158°E) are calculated covering the range between a NW-SE and NNW-SSE orientation.

Since no historic stress gradients are published, σ_V and σ_{hmin} gradients are taken from Meixner et al. (2014), who characterized the present-day stress field at the Bruchsal geothermal site as normal faulting regime with transition to strike-slip. The σ_{Hmax} gradient is guessed considering the requirement of $\sigma_{Hmax} > \sigma_V$, to meet the conditions for a strike-slip regime.

Published stress gradients comprise a density-log derived vertical stress gradient σ_V of 23.8 MPa km^{-1} as well as a minimum horizontal stress gradient of 15.3 MPa km^{-1}, derived from leak-off tests, conducted in the Middle Keuper (Meixner et al. 2014) (Table 4.1). Considering a strike-slip faulting regime for the Miocene (Illies 1978; Buchner 1981; Schumacher 2002; Dèzes et al. 2004), the possible range of σ_{Hmax} has a lower bound of $\sigma_{Hmax} = 1 * \sigma_V$ and an upper bound of $\sigma_{Hmax} = 1.42 * \sigma_V$ according to the stress polygon concept (Meixner et al. 2014). Slip and dilation tendencies are calculated using the averaged σ_{Hmax} gradient of $\sigma_{Hmax} = 1.21 * \sigma_V = 28.8$ MPa km^{-1} (Table 4.1).

Table 4.1: The strike-slip stress model for the Miocene taking the uncertainty of the σ_{Hmax} orientation into account.

Age	Faulting regime	Gradients (MPa/km)				σ_{Hmax} orientation
		σ_V	σ_{Hmax}	σ_{hmin}	P_p	
Miocene	Strike-slip	23.8	28.8	15.3	10.2	N146°E ± 11°

To assess fault stability, slip tendency analyses often assume the frictional fault strength, given by the coefficient of static friction μ, as μ = 0.6 (Worum et al. 2004; Becker et al. 2019b; Kinoshita et al. 2019; Ferrill et al. 2020b). This followes Byerlee (1978) who proposed a range for μ of 0.6 to 0.85. This is valid as upper limit with the friction of fault gouge can be as low as < 0.2 as demonstrated by Ferrill et al. (2017b). The fault's frictional strength depends on, among others, on the mineralogical content of the fault gouge and therefore on the faulted host-rock lithology (Zhang 2019). Research shows a decrease of the coefficient of friction with increasing clay mineral content (Takahashi et al. 2007; Tembe et al. 2010; Kohli and Zoback 2013; Kato and Hirono 2016; Zhang 2019; Bedford et al. 2022). Moreover, the coefficient of static friction can be reduced by the presence of water, demonstrated for sandstone samples by Noël et al. (2021).

Since no samples or information on the mineralogical composition of the Leopoldshafen fault gouge material is available, two failure envelopes are used to cover the possible range of fault strength. With the faulted Cenozoic sedimentary succession consisting mostly of marlstones and mudstones with intercalated sandstones (Perner et al. 2018), a coefficient of static friction of 0.4, representing a clay-rich fault gouge is chosen as lower bound of possible fault strength (Verberne et al. 2010). The upper bound is represented by a coefficient of static friction of μ = 0.6 which is more likely for Mesozoic sedimentary rocks.

4.4.4 Fault Response Modelling

The Fault Response Modelling tool within the MOVE Software Suite computes fault-induced displacement, stress and strain in an ambient elastic medium based on elastic dislocation theory. Complex fault geometries can be resolved by the use of triangular dislocation elements. Fault slip induced deformation within the elastic medium causes a displacement field, from which the corresponding strain and stress fields can then be deduced. Displacement boundary conditions can be defined as slip vectors, with heterogeneous slip distributions derived from fault throw analysis often considered as input data (Maerten et al. 2006). However, this approach is only applicable for pure dip slip kinematics. As transtensional strike-slip or pure strike-slip movement is assumed for the Miocene activity of the Leopoldshafen fault, the horizontal slip distribution cannot be quantified. Instead, a uniform slip distribution, respectively a constant slip vector is assumed. The maximum principal strain axis e_1 (by convention: $e_1 > e_2 > e_3$) as well as dilation (= $e_1 + e_2 + e_3$), as a measure of volumetric strain, are used as two- and three-dimensional

observation attributes. We model the spatial magnitude distribution for e_1 and dilation to identify strain concentrations around the fault.

To cover the range of possible fault slip kinematics, three scenarios are calculated. Scenario 1 describes pure sinistral strike-slip kinematics, which is in agreement with the general assumption of a sinistral strike-slip reactivation of the Upper Rhine Graben (Illies 1978; Schumacher 2002; Dèzes et al. 2004). Scenario 2 and 3 represents transtensional sinistral strike-slip kinematics with an overall oblique slip vector consisting of a horizontal slip and a vertical dip slip component. This is in agreement with paleoseismological observations in the central Upper Rhine Graben (Reicherter et al. 2021; Ritz et al. 2021). As the Upper Rhine Graben is still active, but Miocene slip rates are not available, published neotectonic slip rates are taken instead as an approximation. The authors are aware, that neotectonic slip rates, measured over geologically short time frames, but extrapolated for the Miocene period, might introduce some uncertainty. This issue will be discussed below. Quantified vertical as well as horizontal displacement is given by Pena-Castellnou et al. (2023) derived from paleoseismological trenching at the eastern boundary fault within the central Upper Rhine Graben segment. They documented oblique left-lateral kinematics with a vertical slip rate of 0.02 ± 0.005 mm yr^{-1} and a horizontal slip rate of 0.1 ± 0.01 mm yr^{-1} over a time period of 65 ka.

With the stress field reorientation in the Early Miocene at around 20 Ma ago (Illies 1978; Schumacher 2002; Dèzes et al. 2004), and the fault activity of the Leopoldshafen fault ceased roughly 5 Ma ago (Figure 4.2), absolute slip magnitudes can be calculated based on the considered slip rates. The slip vector for scenario 1 amounts to a horizontal component of 1500 m (Table 4.2) (Figure 4.5). In addition to the horizontal slip vector of 1500 m, scenario 2 considers a vertical dip slip component of 300 m, to form an overall oblique slip vector (Table 4.2) (Figure 4.5). Scenario 3 represents a vertical slip component of 300 m and a lower variation of the horizontal component of 500 m (Table 4.2) (Figure 4.5).

Table 4.2: Fault Response Modelling input data given as slip vector for three scenarios covering sinistral strike-slip kinematics, with a dip slip component considered for scenario 2 and 3. Here we define h = horizontal and v = vertical.

Scenario	**Kinematics**	**Slip vector**
1	Sinistral strike-slip	h = 1500m
2	Sinistral strike-slip + dip slip	h = 1500m, v = 300m
3	Sinistral strike-slip + dip slip	h = 500m, v = 300m

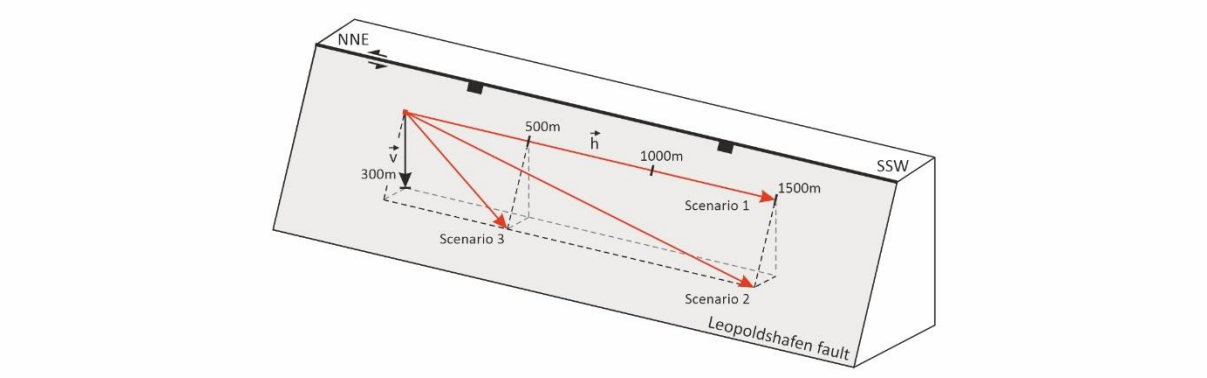

Figure 4.5: Kinematical scenarios for the movement of the hanging wall of the Leopoldshafen fault during Miocene reactivation ranging from pure sinistral strike-slip (scenario 1) to transtensional sinistral strike-slip with dip slip components (scenario 2 and 3).

4.5 Results

4.5.1 Geomodel

The GeORG depth structure maps indicate two major NNE-SSW trending, WNW-dipping normal faults (Leopoldshafen and Stutensee fault) in the study area, which both displace the Cenozoic and Mesozoic horizons, forming a tilted fault block (e.g., Base Froidefontaine Fm. horizon) (Figure 4.6a). The distance between the major normal faults, the horizontal extent of the rigid fault block measured perpendicular to the general fault strike, totals 3 to 5 km (Figure 4.6a).

The former Leopoldshafen oil-field is located in the footwall of the Leopoldshafen fault, which appears to consist of two NNE-SSW trending segments, linked by a left-stepping N-S to NNW-SSE striking fault bend segment (Figure 4.6a). The bend segment zone has a width of approximately 1500 m, measured on the Base Froidefontaine Fm. depth map. The step angles range between 20° and 25° (Figure 4.6a).

To investigate the complex geometry of the Leopoldshafen fault and its impact on vertical fluid migration, a fundamental structural reservoir model is constructed, capturing the surrounding area (Figure 4.6a). With a horizontal extent of 7 km in WNW-ESE and 14 km in NNE-SSW direction, the model represents a model alignment subparallel to the overall Upper Rhine Graben strike. The geomodel incorporates four major Cenozoic horizons (Base Iffezheim Formation, Base Landau Formation, Base Froidefontaine Formation & Base Tertiary) and two major Mesozoic horizons (Base Keuper and Base Muschelkalk), normal-displaced by the Leopoldshafen fault.

A reservoir zone is constructed to constrain the vertical position of the multi-level reservoir system. The zone's vertical extent is calculated using thickness information from the Leopoldshafen-1 well report. With the producing reservoir intervals located in the Froidefontaine Formation (Rupelian Cyrena Marls & Meletta Beds) and Niederrödern Formation (Chattian Bunte Niederröderner Beds), the reservoir zone extents from the referential Base Froidefontaine Fm. horizon until a constructed Top Niederrödern Fm.

horizon. Therefore, this reservoir zone has a vertical extent of 646 m, assuming a constant thickness for the modeled area.

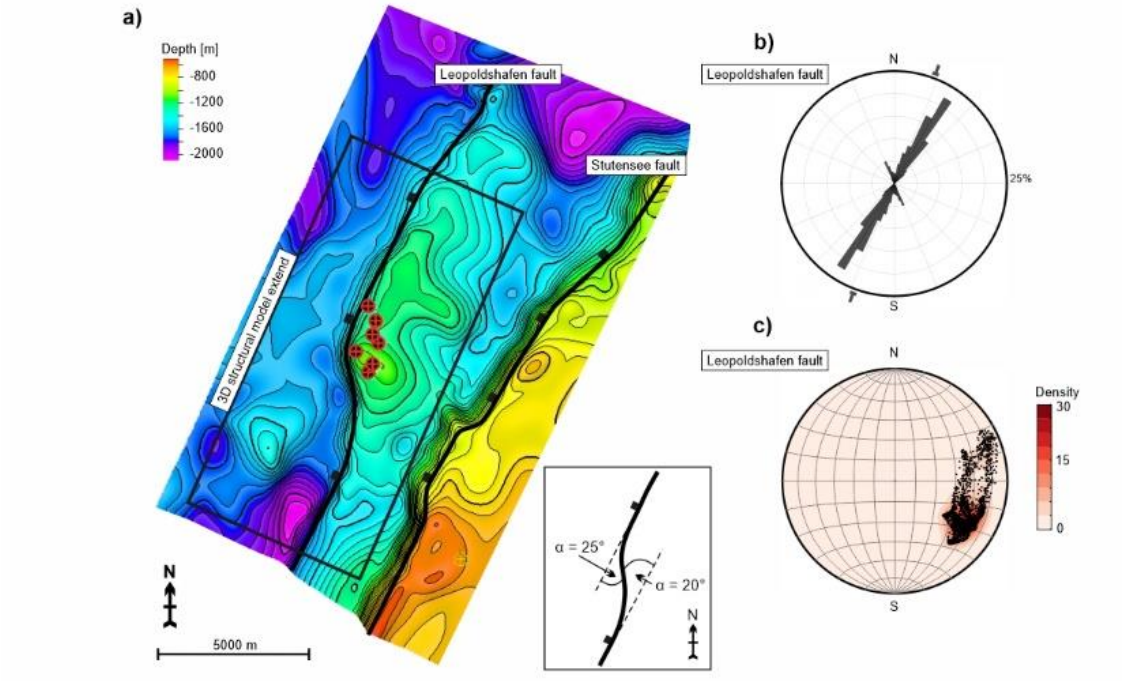

Figure 4.6: a) The structure map of the Base Froidefontaine Formation, given as depth below sea level, highlights two major NNE-SSW trending normal faults. b) Rose plot indicates an overall NNE-SSW trend for the Leopoldshafen fault with a NNW-SSE striking bend segment. c) Poles of the modeled Leopoldshafen fault along strike plotted on a Schmidt net (lower hemisphere) indicating an overall WNW-dipping fault.

4.5.2 Expansion Index (EI) analysis

Expansion Index (EI) analysis is conducted for a W-E oriented line across the Leopoldshafen fault bend, oriented roughly normal to the fault bend trend, (Figure 4.7a), to be able to temporally resolve the fault activity. The studied formations are grouped into zones (from top to bottom):

Zone I: Base Iffezheim Fm. to Base Landau Fm.

Zone II: Base Landau Fm. to Base Froidefontaine Fm.

Zone III: Base Froidefontaine Fm. to Base Tertiary

Zone IV: Base Tertiary to Base Keuper

Zone V: Base Keuper Fm. to Base Muschelkalk

Across-fault thickening is observed for zone I, II and III, indicated by an Expansion Index EI > 1 (Figure 4.7b, c). The zones IV and V show EI values roughly around 1 (Figure 4.7c). The Leopoldshafen fault zone terminates vertically below the Base Iffezheim Fm., which appears not to be faulted (Figure 4.7b).

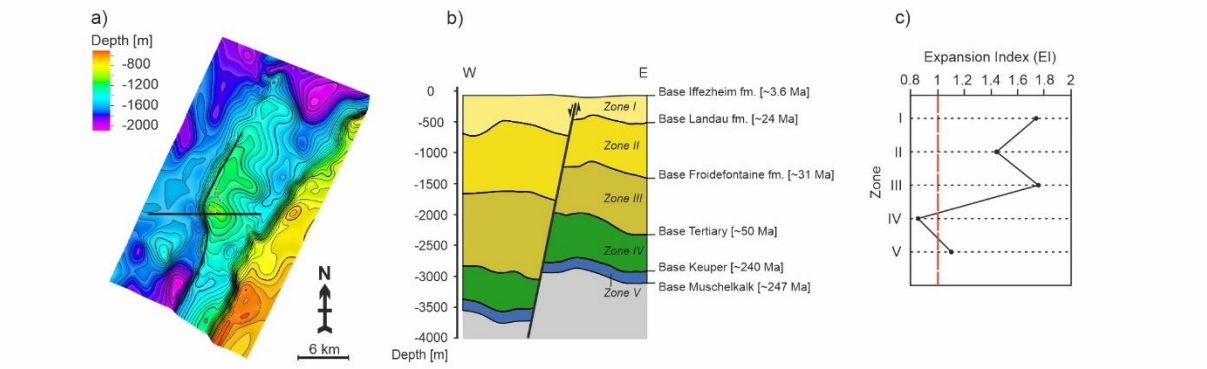

Figure 4.7: a) Overview map of the Base Froidefontaine Fm. depth structure map with the cross-section highlighted by the black line. b) Cross-sectional view in W-E orientation. Assigned ages are taken from Deutsche Stratigraphische Kommission (2016). c) Expansion index (EI) calculated to highlight across-fault thickening.

4.5.3 Slip and dilation tendency analysis

Scenario 1 σ_{Hmax} N135°E (NW-SE)

Slip tendencies calculated for the Leopoldshafen fault, considering NW-SE (N135°E) horizontal compression, range between $T_{Smin} = 0.10$ and $T_{Smax} = 0.69$, with a mean of $T_{Smean} = 0.29$ (Figure 4.8a, e). Slip tendencies for the modeled fault exceeding the referential coefficient of static friction of $\mu = 0.6$ amount to 10 %. Considering a frictional fault strength of $\mu = 0.4$, 22 % of the modeled Leopoldshafen fault is subject to slip tendencies of $T_S > 0.4$. With respect to a depth level of 1000 m, representing roughly the position of the Base Froidefontaine Fm. footwall trace, slip tendencies of $T_S > 0.4$ are observed (17 %) but no $T_S > 0.6$ (Figure 4.8a, c, d).

A heterogeneous spatial distribution of T_S on the modeled fault surface is observed (Figure 4.8a). Highest slip tendencies ($T_S > 0.4$) are located within the NNW-SSE to N-S trending fault segment, while the NNE-SSW trending fault segments are subject to lower slip tendencies (Figure 4.8a). An increase in T_S magnitude with depth is also evident for the fault bend segment (Figure 4.8a).

Dilation tendencies range between $T_{Dmin} = 0.05$ and $T_{Dmax} = 0.91$, with a mean of $T_{Dmean} = 0.27$ (Figure 4.8f). The calculated dilation tendency is spatially heterogeneously distributed along the fault, with highest T_D located within the NNW-SSE to N-S trending fault bend segment (Figure 4.8b). 20 % of this fault segment exceeds dilation tendencies of 0.8. As depth increases, the T_D magnitude increases, which is observable within the fault bend segment (Figure 4.8b).

Combining these results, the NNW-SSE trending fault bend segment at a depth level of around -1000 m ± 200 m was subject to high slip ($T_S > 0.4$) and moderate dilation tendencies ($T_D < 0.8$) (Figure 4.9a, d). Slip and dilation tendencies can be even higher ($T_S > 0.6$ and $T_D > 0.8$) for the steep dipping fault areas at deeper levels (Figure 4.9a, d). Within the NNE-SSW trending fault segments lowest slip ($T_S < 0.4$) and dilation tendencies ($T_D < 0.4$) are observed (Figure 4.9 a, d).

Scenario 2 σ_{Hmax} N146°E

Slip tendencies calculated for the Leopoldshafen fault, considering N146°E horizontal compression, range between T_{Smin} = 0.14 and T_{Smax} = 0.68 (T_{Smean} = 0.36) (Figure 4.8g, k). Slip tendencies exceeding the referential coefficient of static friction of μ = 0.6 amount to 5 %, while 33 % exceed μ = 0.4 (Figure 4.8k). Around the depth level of the Base Froidefontaine Fm. footwall trace, respectively roughly 1000 m depth, slip tendencies of $T_S > 0.4$ are observed (27 %) but no $T_S > 0.6$ (Figure 4.8g, I, j).

A heterogeneous spatial distribution of T_S on the modeled fault surface is evident (Figure 4.8g). Spatial anomalies of higher slip tendencies ($T_S > 0.4$) are located within the NNW-SSE to N-S trending fault segment, while the NNE-SSW trending fault segments are subject to relatively lower slip tendencies (Figure 4.8g). An increase in T_S magnitude with depth is additionally observed for the fault bend segment (Figure 4.8g).

Dilation tendencies fall in a range between T_{Dmin} = 0.09 and T_{Dmax} = 0.98, with a mean of T_{Dmean} = 0.36 (Figure 4.8f). The calculated dilation tendency is spatially heterogeneously distributed along the fault, with highest T_D located within the NNW-SSE to N-S trending fault bend segment (Figure 4.8b). 41 % of this fault segment exceeds dilation tendencies of 0.8. With increasing depth, the T_D magnitude increases, evident within the fault bend segment (Figure 4.8b).

For scenario 2, the NNW-SSE trending fault bend segment at a depth level of around -1000 m ± 200 m was subject to high slip ($T_S > 0.4$) and moderate dilation tendencies ($T_D < 0.8$) (Figure 4.9b, e). Within the steep dipping fault areas at deeper levels, slip and dilation tendencies can be even higher ($T_S > 0.6$ and $T_D > 0.8$) (Figure 4.9b, e). Lowest slip ($T_S < 0.4$) and dilation tendencies ($T_D < 0.4$) are observed for the NNE-SSW trending fault segments (Figure 4.9b, e).

Scenario 3 σ_{Hmax} N158°E (NNW-SSE)

Analysis for the NNW-SSE horizontal compression scenario reveals slip tendencies within the range of T_{Smin} = 0.11 to T_{Smax} = 0.66 (T_{Smean} = 0.43) (Figure 4.8m, q). Results indicate 5 % of the modelled Leopoldshafen fault to be subject to slip tendencies $T_S > 0.6$, while 62 % exceeds a T_S of 0.4. With respect to a depth level of -1000 m, representing roughly the position of the Base Froidefontaine Fm. footwall trace, slip tendencies of $T_S > 0.4$ are observed (51 %) but no $T_S > 0.6$ (Figure 4.8m, o, p).

The spatial slip tendency distribution on the Leopoldshafen fault is heterogeneous (Figure 4.8m) with higher slip tendencies located around the N-S trending edges of the bend segment (Figure 4.8m). Comparably lower slip tendencies are observed for the NNE-SSW striking segments of the Leopoldshafen fault (Figure 4.8m).

Computed dilation tendencies are in a range between T_{Dmin} = 0.16 and T_{Dmax} = 1 (T_{Dmean} = 0.49) (Figure 4.8f). Dilation tendency is spatially heterogeneously distributed along the Leopoldshafen fault. Highest T_D are observed within the NNW-SSE to N-S trending fault segment (Figure 4.8b), with 62 % of this

segment exceeding dilation tendencies of 0.8. Generally, the T_D magnitude increases with depth, evident within the fault bend segment (Figure 4.8b).

For scenario 3, the NNW-SSE trending fault bend segment was subject to high slip ($T_S > 0.4$) and moderate to high dilation tendencies ($T_D > 0.8$) at a depth level of around -1000 m ± 200 m (Figure 4.9c, f). Modeled slip and dilation tendencies may be even higher ($T_S > 0.6$ and $T_D > 0.8$) for the steeply dipping fault areas at deeper levels (Figure 4.9c, f). The lowest slip ($T_S < 0.4$) and dilation tendencies ($T_D < 0.4$) are observed for the NNE-SSW trending fault segments (Figure 4.9c, f).

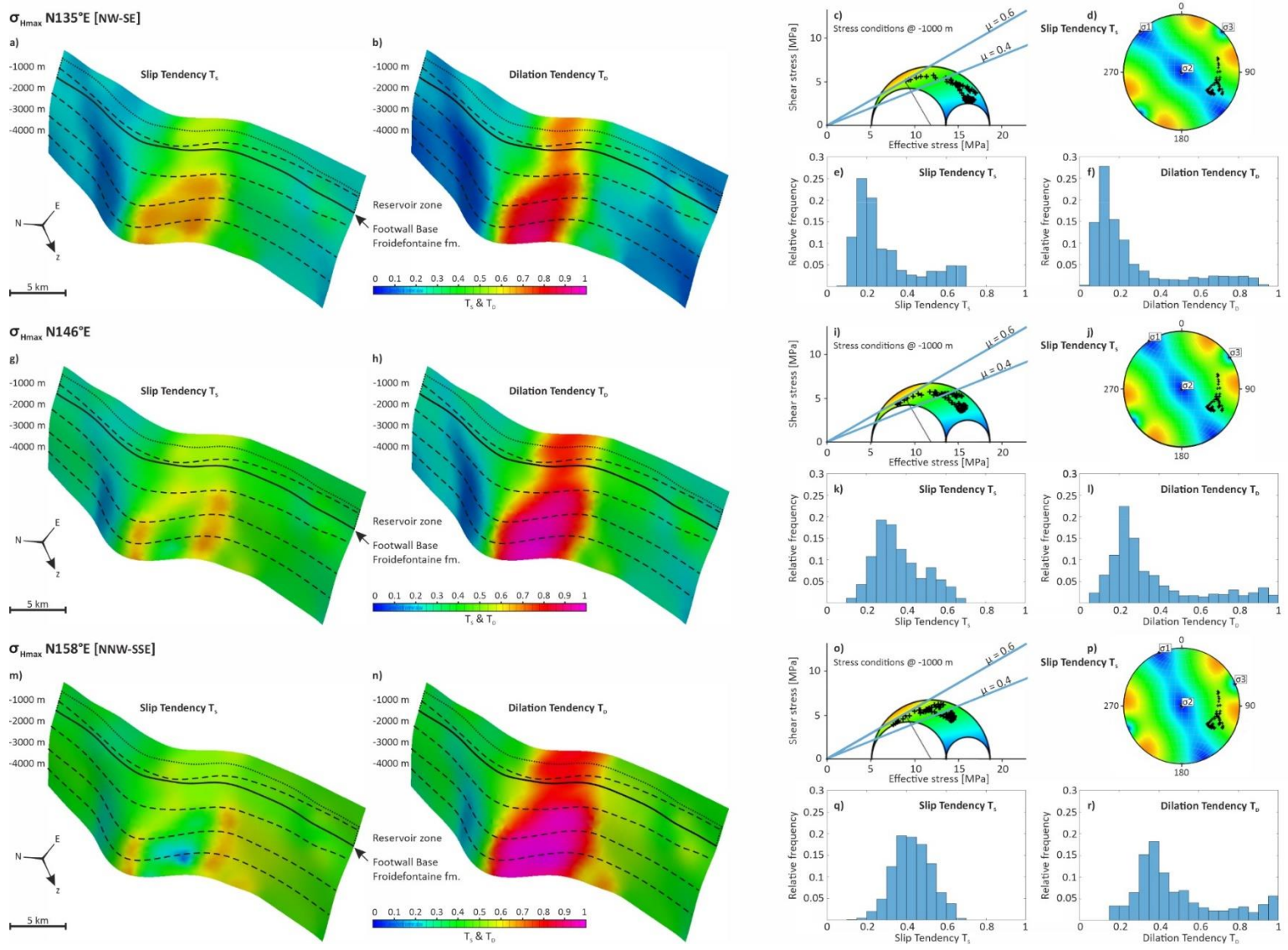

Figure 4.8: a), b), g), h), m), n) Spatial distribution of slip (T_S) and dilation (T_D) tendencies on the modeled Leopoldshafen fault for three different σ_{Hmax} orientations. c), d), i), j), o), p) Stress conditions at 1000 m depth given as Mohr diagram and stereographic plot considering two static friction coefficients ($\mu = 0.4$ and $\mu = 0.6$). e), f), k), i), q), r) Slip and dilation tendency distributions of the modeled fault surface for each σ_{Hmax} scenario.

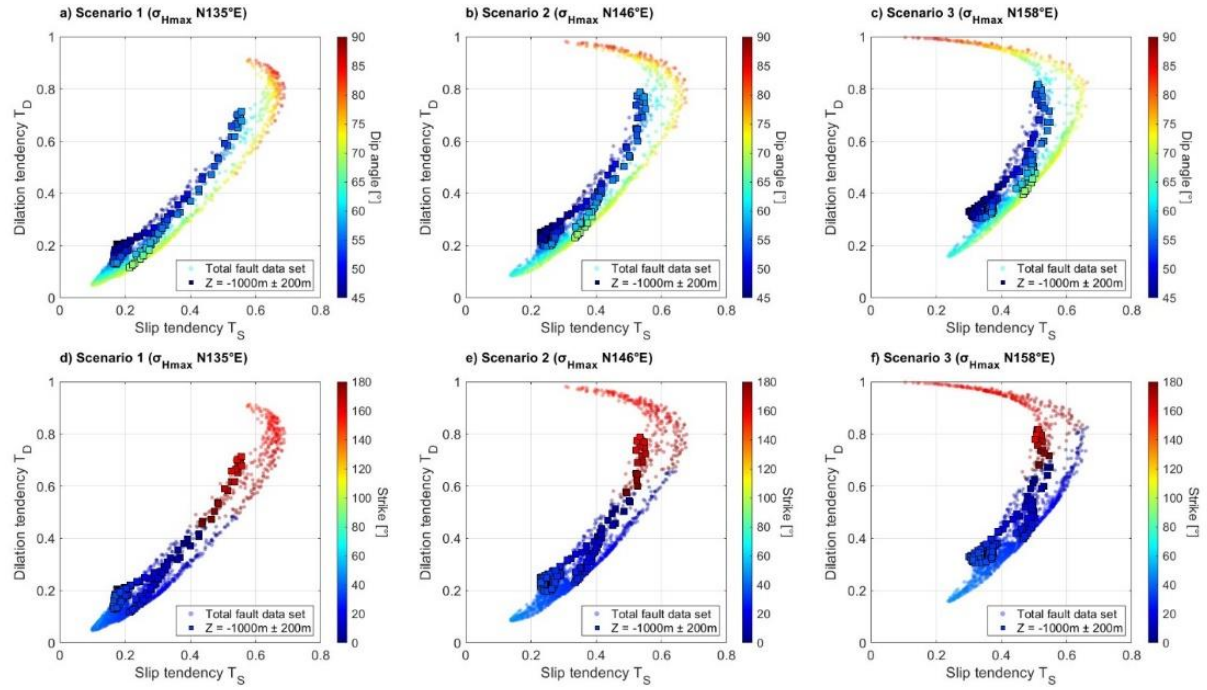

Figure 4.9: a), b), c) Slip and dilation tendency cross-plot for σ_{Hmax} scenarios 1-3 color-coded for the dip angles. Background data given as circles represent the entire modeled Leopoldshafen fault surface, while depth-restricted fault data (z = -1000 m ± 200 m) is indicated by square signatures. d), e), f) Slip and dilation tendency cross-plot color-coded for the strike orientation.

4.5.4 Fault Response Modelling

Fault Response Modelling for pure sinistral strike-slip kinematics (scenario 1) indicate a positive volumetric strain (dilation) concentration around the fault bend segment in the hanging and footwall of the Leopoldshafen fault for an observation horizon at 1000 m depth (Figure 4.10a). The spatial distribution of the maximum principal strain e_1 magnitude highlights strain concentration around the fault bend segment (Figure 4.10d). With strain generally decreasing away from the fault, the spatial extent is more pronounced in the hanging wall.

Fault Response Modelling considering an oblique slip vector (plunging 13°) (scenario 2) results in a positive volumetric strain concentration around the fault bend segment, which is slightly laterally shifted on the same observation horizon at 1000 m depth (Figure 4.10b). The e_1 strain pattern is comparable to the one of scenario 1 with a local strain concentration around the fault bend and a more pronounced zone of intermediate strain within the hanging wall of the Leopoldshafen fault (Figure 4.10e).

Considering an oblique slip vector with a lower variation of the horizontal slip component (plunging 35°) (scenario 3), the resulting volumetric (dilation) and longitudinal strain (e_1) change in magnitude but the spatial strain patterns remain comparable to scenario 1 and 2 on the same observation horizon at a depth level of -1000 m (Figure 4.10c, f).

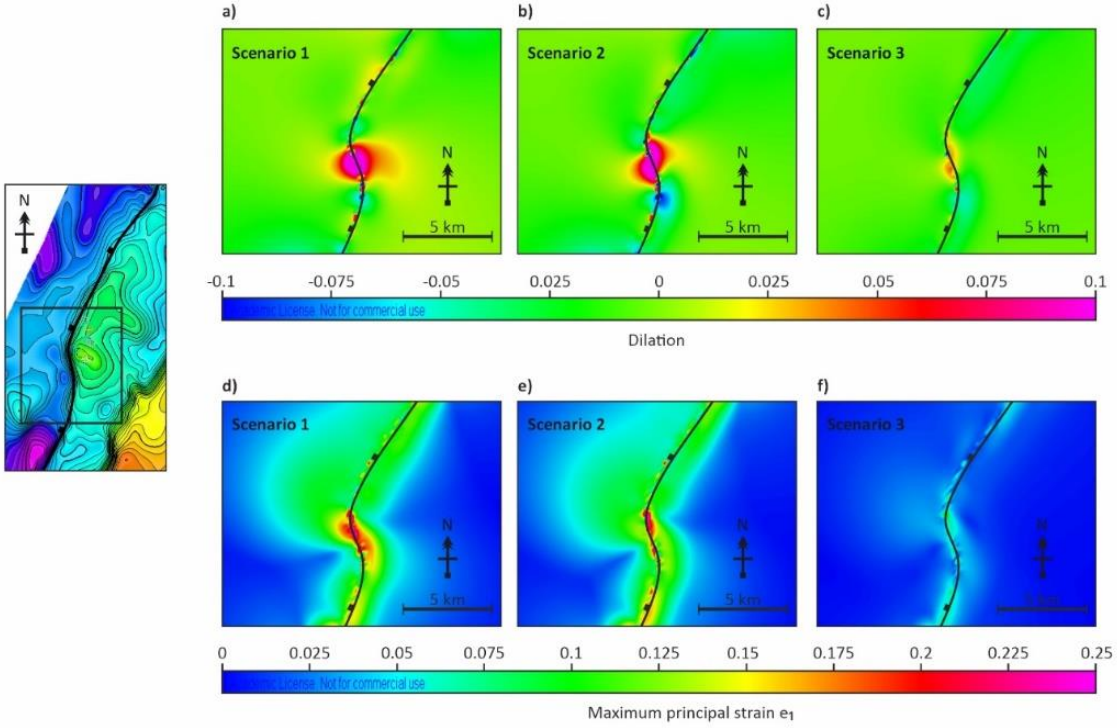

Figure 4.10: Fault Response Modelling simulation results for scenario 1 (a, d), 2 (b, e) and 3 (c, f) shown as volumetric strain magnitude (dilation) and maximum principal strain magnitude (e_1) on an observation horizon at 1000 m depth.

4.6 Discussion

4.6.1 Geomodel

The geographical location of the studied Leopoldshafen fault has been published in several studies (Sauer and Nägele 1981; Boigk 1981; Sokol et al. 2013), with the geomodel being based on published data from the GeORG project (Sokol et al. 2013). The regional-scale GeORG model, whose structural framework is mostly based on 2D seismic fault interpretations, is occasionally supplemented by fault interceptions from borehole reports (Sokol et al. 2013). Concerning the uncertainty of the Leopoldshafen fault, Reinhold et al. (2016) demonstrated the misfit between fault traces derived from 2D seismic interpretations and fault traces from 3D seismics for the Upper Rhine Graben. With up to 20 wells being drilled for exploration and exploitation of the former Leopoldshafen oil field, most of the wells intersected the Leopoldshafen fault, adding confidence in the modeled fault trace of the GeORG model. However, modeled faults and wellbore fault intersections often could not be matched satisfactorily, according to Sokol et al. (2013).

Relay ramps developed as result of fault growth via horizontal linkage are key components of evolving rift basins (Fossen and Rotevatn 2016) and described as a substantial part of the Upper Rhine Graben structural inventory (Le Carlier de Veslud et al. 2005; Reinhold et al. 2016; Kraml et al. 2016). It is therefore likely, that the Leopoldshafen fault is made up of two hard-linked NNE-SSW trending fault segments with the fault bend as a breached relay ramp. The detailed structural character of the 1.5 km wide fault bend zone of the Leopoldshafen fault might be studied in detail with high resolution 3D seismic to identify potential fault linkage via seismic attribute analysis.

4.6.2 Fault activity

Expansion Index analysis revealed across-fault thickening for zone I – III, identifying these as a syn-rift sequence. However, given the coarse stratigraphic resolution of the 3D structural model, and the fact, that fault activity ceased prior to the deposition of the Base Iffezheim Fm. (3.6 Ma), zone I contains parts of the syn-rift as well as the post-rift sequence.

Considering the coarse stratigraphic resolution of zone III, which ranges from 50 Ma (Base Tertiary) to 31 Ma (Base Froidefontaine Fm.), the onset of fault activity falls temporally somewhere in-between. This implies, that fault activity of the Leopoldshafen fault had started prior to the deposition of the Base Froidefontaine Fm. 31 Ma ago (Rupelian/Early Oligocene) (Deutsche Stratigraphische Kommission 2016), and thus can be linked to the main phase of graben formation during the Oligocene (Schumacher 2002; Dèzes et al. 2004). This is consistent with the general assumption that rifting and basin subsidence primarily occurred during the main phase of graben formation, which was accompanied by basin-parallel normal faulting (Reinhold et al. 2016). Since the activity of the Leopoldshafen fault commenced at least 31 million years ago, the fault was subject to the stress field reorientation in the early Miocene.

4.6.3 Slip & dilation tendency analysis

Slip and dilation tendency analysis revealed a spatially heterogeneous distribution along the Leopoldshafen fault. Since slip and dilation tendency are controlled, among other factors, by the angular relationship between the along-strike geometry of the fault and the stress orientation (Morris et al. 1996; Ferrill et al. 1999), a range of possible σ_{Hmax} orientations (NW-SE to NNW-SSE) is tested.

Dilation tendency analysis revealed along-strike T_D anomalies, with the NNW-SSE to N-S trending fault bend segment to experienced highest dilation tendencies ($T_D > 0.8$), valid for the considered σ_{Hmax} orientation range (NW-SE to NNW-SSE). However, the percentage of the area where $T_D = 0.8$ is exceeded, is highest for a NNW-SSE σ_{Hmax} fault-bend orientation.

Slip tendency results indicate a spatial anomaly of higher slip tendencies ($T_S > 0.4$) within the fault bend segment for a NW-SE (N135°E) oriented σ_{Hmax}. For a maximum horizontal stress direction of N146°E and N158°E (NNW-SSE), the location of higher slip tendencies ($T_S > 0.4$) shifts towards the N-S trending edges of the fault bend segment.

With special emphasis on shallower depth levels (around 1000 m), slip tendencies partially exceed the lower coefficient of friction of $\mu = 0.4$ but do not exceed the frictional threshold of $\mu = 0.6$. While for the NW-SE (N135°E) σ_{Hmax} scenario, mainly the NNW-SSE to N-S trending fault bend segment is subject to $T_S > 0.4$, this pattern changes for a NNW-SSE oriented σ_{Hmax} with most of the Leopoldshafen fault experiencing $T_S > 0.4$.

Whether the fault bend segment was critically stressed depends on the choice of the friction coefficient. With respect to the lower bound of frictional fault strength criterion ($\mu = 0.4$), the fault bend segment was partially critically stressed since the stress field reorientation of the Early Miocene. However, as slip tendencies do not exceed $T_S = 0.6$ in any scenario at a depth of 1000 m, the fault can be considered as not critically stressed with respect to the frictional threshold of $\mu = 0.6$.

Fault strength can vary spatially depending on fault rock composition, including clay content (Tembe et al. 2010; Verberne et al. 2010; Meng et al. 2017; Ashman and Faulkner 2023), and thus on faulted lithologies and fault throw. Because the frictional strength of the Leopoldshafen fault is unknown and therefore expressed as a range ($\mu = 0.4 - 0.6$), the results rather qualitatively identify the fault bend segment as a site of higher slip tendencies along strike. The considered range of fault frictional strength is approximated by the mechanical properties of the Rotliegend Slochteren sandstone and Ten Boer claystone with coefficients of static friction of $\mu = 0.6$ and $\mu = 0.4$ respectively (Hunfeld et al. 2017).

Following the approach of Ferrill et al. (2020a), deformation behavior is controlled by the fault's exposure to the prevailing stress field, and thus on slip (T_S) and dilation (T_D) tendencies. Based on T_S-T_D cross-plots, the NNW-SSE trending fault bend segment is subject to high slip and moderate to partially high dilation tendencies across all computed σ_{Hmax} scenarios. The fault bend segment plots within the shear failure zone

for σ_{Hmax} scenarios of N135°E and N146°E and reaches towards the hybrid failure region for a σ_{Hmax} of N158°E (Ferrill et al. 2020a). Volume gain is associated with hybrid failure but also with shear failure, as the misalignment of the rough slip surfaces can create a volume gain (Zimmermann et al. 2019; Cheng and Milsch 2021). As a detailed structural interpretation is key for predicting deformation behaviour along the fault surface (Ferrill et al. 2020a), the resolution of the regional-scale GeORG model has to be considered as a limitation.

Both slip and dilation tendencies are controlled by the magnitude of the prevailing stress field and its orientation (Morris et al. 1996; Ferrill et al. 1999; Meng et al. 2017). The Miocene stress field is described by the stress regime type and the orientation of its three principal stresses (Illies 1978; Schumacher 2002; Dèzes et al. 2004; Rotstein and Schaming 2011). Since no stress information for one of the studied Leopoldshafen wells were available, stress data were taken from the Bruchsal site (Meixner et al. 2014), located at the eastern border fault in the central Upper Rhine Graben, roughly 13 km NE of the Leopoldshafen oil field. While upper and lower bounds of σ_{Hmax} gradients valid for a strike-slip faulting regime are provided by Meixner et al. (2014), an averaged σ_{Hmax} gradient of $\sigma_{Hmax} = 1.21*\sigma_V$ was applied for this study. Any σ_{Hmax} gradient variation within the upper and lower bound would affect the magnitude of calculated T_S, but not the location.

Meixner et al. (2014) presented two σ_{hmin} measurements derived from leak-off pressure tests: one conducted in the consolidated Lower Triassic Middle Buntsandstein and the other in the Upper Triassic Keuper. As the horizontal stress is highly dependent on the lithology (Warpinski and Teufel 1989; Wileveau et al. 2007; Gunzburger and Cornet 2007; Takahashi et al. 2007; Zhang 2019), the σ_{hmin} gradient derived from the Upper Triassic Keuper might be more representative for the often unconsolidated, clay-rich, sedimentary Cenozoic series (Perner et al. 2018).

4.6.4 Fault Response Modelling

Fault bends that locally accommodate extension are referred to as releasing bends (Cunningham and Mann 2007) and can act as dilational jogs (Ando et al. 2004; Zhang et al. 2008). Thereby, the bending geometry of the fault relative to the slip vector determines whether it is a releasing or restraining bend (Sylvester 1988; Mann 2007). Accordingly, the left-stepping Leopoldshafen fault, associated with transtensional sinistral strike-slip kinematics, can be regarded as releasing bend. The localized extensional deformation associated with releasing bends (Cunningham and Mann 2007) is in agreement with Fault Response Modelling results, indicating local positive volumetric (dilation) and maximum principal (e_1) strain concentrations in the hanging and footwall of the bend segment. Therefore, the along-strike geometry of the Leopoldshafen fault appears as a dominant control on subsurface strain distribution patterns.

It has to be considered, that slip vectors used for Fault Response Modelling are based on published neotectonic slip rates recorded over 65 ka (Pena-Castellnou et al. 2023). The vertical slip rate of 0.02 mm yr^{-1} taken from Pena-Castellnou et al. (2023), derived from paleoseismological trenching in the central Upper

Rhine Graben, is in good agreement with fault throw observations for the Base Landau Fm. based on the constructed geomodel. Since the Base Landau Fm. was deposited roughly 24 Ma ago (Deutsche Stratigraphische Kommission 2016), one million years prior to the onset of the Miocene, the observed maximum throw of 280 m yields an averaged vertical slip rate of 0.015 mm yr^{-1} for the period until the Pliocene (5 Ma). This might justify the application of averaged neotectonic slip rates in this study. Considering the observed dip slip fault displacement of the Base Landau Fm., an oblique slip vector (Fault Response Modelling scenario 2 or 3) is generally more reasonable than pure strike-slip kinematics (Fault Response Modelling scenario 1). The magnitude of the horizontal slip vector (1500 m) is also based on paleoseismological trenching analysis (horizontal slip rate of 0.1 mm yr^{-1}) (Pena-Castellnou et al. 2023), without any direct indication to proof the magnitude. To account for this uncertainty, a variation of the horizontal slip magnitude was calculated (scenario 3), without altering the location of positive dilation in the fault bend. However, kinematic sinistral strike-slip components are reported for the graben boundary as well as graben-parallel faults (Frey et al. 2022).

Although the slip vector of the Leopoldshafen fault during the second phase of the Upper Rhine Graben graben development is only roughly known, the Fault Response Modellingresults could qualitatively demonstrate local reactivation-related strain in the fault bend segment for slip vectors ranging from pure strike-slip to strike-slip with a dip-slip component.

4.6.5 Implications for fault controlled hydrocarbon migration

Releasing bends are commonly associated with complex fracture networks, vein formation and fluid flow, controlled by fault-related localized dilation (Sibson 1996; Muchez and Sintubin 1998; Stephen 2005; Cunningham and Mann 2007; Zhang et al. 2008). In addition, fault bends are considered potential locations for hydrocarbon migration (Ligtenberg 2005) as well as prolific structural settings for geothermal systems in e.g., the Great Basin region (Faulds and Hinz 2015). With Fault Response Modelling indicating strain concentrations around the fault bend segment as well as in the hanging wall block, these areas might be more intensively fractured, as fracture intensity can be linked to high strain concentrations (Dee et al. 2007; Watkins et al. 2015).

Beside these structural controls on fluid flow, multiple research studies could establish a link between structurally controlled vertical fluid migration and fault alignment within the prevailing stress field (Linjordet and Skarpnes 1992; Harper and Lundin 1997; Wiprut and Zoback 2000; Ferrill et al. 2017a; Miocic et al. 2020; Smeraglia et al. 2022). Wiprut and Zoback (2000) as well as Miocic et al. (2020) exemplified the correlation between critically stressed faults and fluid migration.

Combining the results of this study, the Leopoldshafen fault bend segment was subject to highest dilation tendencies and high slip tendencies since the Miocene stress field reorientation, with the segment being partially critically stressed when considering a frictional fault strength threshold of $\mu = 0.4$. With reported sinistral strike-slip reactivation of the Upper Rhine Graben (Illies 1978; Schumacher 2002; Dèzes et al.

2004), the fault bend segment acted as releasing bend caused by transtensional strike-slip reactivation, with Fault Response Modelling results documenting strain concentrations (dilation and e_1) within the bend segment.

These findings identify the bend segment as potential local vertical pathway for hydrocarbon migration along the Leopoldshafen fault, with a proven oil accumulation in a structurally high fault-dip trapped structure within the footwall of the NNE trending segment (Durst 1991; Reinhold et al. 2016). Thus, mature pre-rift source rocks (Posidonia Shale) in the hanging wall or at deeper positions within the graben center (Böcker and Littke 2016), expelled Liassic oil, which charged the Leopoldshafen structure during the Miocene (Böcker et al. 2017) likely over localized structural migration pathways along the releasing bend of the Leopoldshafen fault. This would confirm the assessment of Bruss (2000), who suggested fault-controlled hydrocarbon migration charging the oil reservoirs along the eastern graben boundary. As reservoir charging might have taken place by vertical migration via the releasing bend, the hydrocarbons might have entered the reservoir formations to migrate further into the structurally high position along the NNE-SSW trending segment of the Leopoldshafen fault. Since the oil field is described as a fault-related trap structure (Durst 1991; Reinhold et al. 2016), the Leopoldshafen fault sealing behavior appears to have changed along-strike.

This study demonstrates the up-fault fluid flow potential in the Upper Rhine Graben, while highlighting the importance of structural geological evaluations in addition to structured reservoir quality analyses (Busch et al. 2022a; Busch et al. 2022b) to assess the integrity of subsurface fluid reservoirs. Such workflow might contribute to future geothermal exploration, targeting sites of elevated structural permeability to yield economical flow rates, and reduce risks.

4.7 Conclusion

This study focuses on the hydrocarbon migration of the fault-related Leopoldshafen oil field to gain a better understanding of structurally controlled fluid flow in the central Upper Rhine Graben.

Slip and dilation tendency analysis under Miocene stress conditions, demonstrated a spatially heterogeneous T_S and T_D distribution along the Leopoldshafen fault, with highest values observed within the left-stepping fault bend segment. Expansion Index analysis indicates fault activity of the Leopoldshafen fault to have started during the main rifting phase (Late Eocene – Oligocene) of the Upper Rhine Graben. Thus, fault activity within the reoriented Miocene stress field might have caused local strain concentrations around the fault bend segment, which acted as a releasing bend under transtensional sinistral strike-slip kinematics.

Reservoir charging of the Leopoldshafen oil field is suggested to have occurred via up-fault hydrocarbon migration along the Leopoldshafen fault bend segment, which might have acted as releasing bend. Thus,

understanding the structural inventory of the Upper Rhine Graben and its control on fluid flow is crucial for future subsurface exploration and alternative post-oil utilization

5 Summary

In this study, the structural control on subsurface fluid flow in two sedimentary basins (Figure 5.1a) has been investigated: fracture networks hosted in Upper Carboniferous tight sandstones of the Ruhr Basin (Variscan foreland basin) (Figure 5.1b) as well as fault-related hydrocarbon migration in the Upper Rhine Graben (Cenozoic rift basin) (Figure 5.1c). Furthermore, the reactivation potential of faults hosted in the Upper Carboniferous sequence of the Ruhr Basin (NE part of the water province "Haus Aden") (Figure 5.1b) has been assessed in the context of mine flooding.

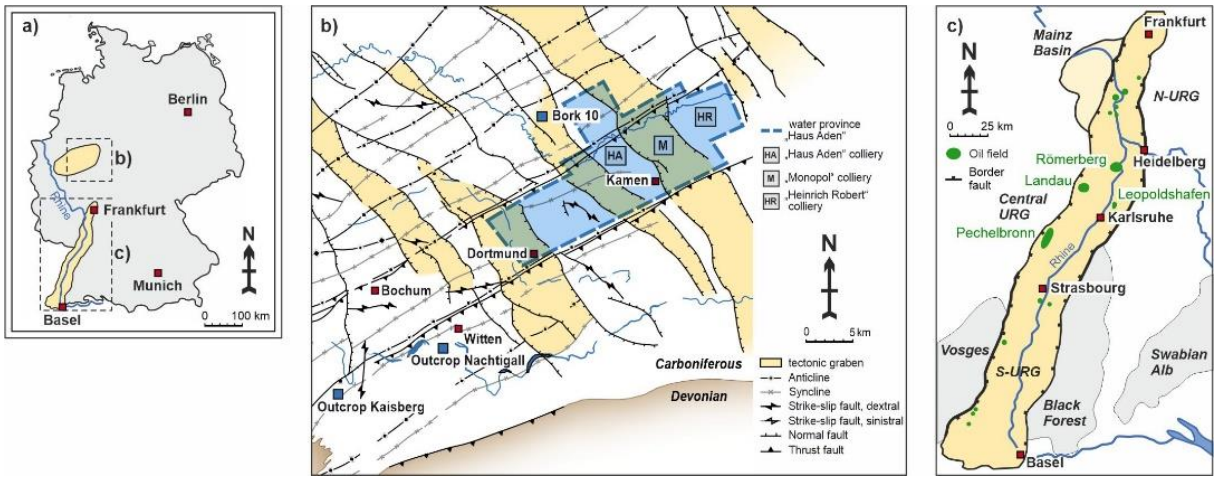

Figure 5.1: a) The study areas are located in west and southwest Germany: the Ruhr Basin (b) (modified after Geologischer Dienst NRW (2020)) and the Upper Rhine Graben (c) (modified after Böcker et al. (2017)).

The fracture networks of Upper Carboniferous tight sandstones have been studied by utilizing digital models of two outcrops (Hattingen, Nachtigall), located along the southern boundary of the Ruhr Basin (Germany) (Figure 5.1b). Three dominant high-angle (w.r.t. bedding) fracture orientations have been identified in the Namurian C Hattingen and Westphalian A Nachtigall outcrop: NNE-SSW to NE-SW (set 1), WNW-ESE (set 2), and NNW-SSE to N-S (set 3) (Figure 5.2a, b). Sandstone bed thickness controls the fracture geometry as it limits the maximum fracture height. In addition, fractures detected in core material of the Bork-10 well (575 to 1212 m TVD), located within the basin, are characterized by two dominant (N-S and W-E) alongside two weakly pronounced trends (NNE-SSW and NW-SE) (Figure 5.2c). Linking the strike directions of the outcrop-derived fractures with the fracture trends of the Bork 10 core data set shows an acceptable match (Figure 5.2a, b, c). Terzaghi-corrected fracture intensities (P_{10}) vary between both analyzed outcrops for comparable orientation trends, ranging from 0.4 to 3.1 m^{-1}. Furthermore, it could be shown that these fracture intensities (P_{10}) are 1.1 to 4.5 times higher than for comparable fracture orientations of the Bork 10 data set.

Critically stressed fracture analysis has been performed for the Bork 10 core data set, utilizing the geomechanical concept of slip tendency, to identify near-vertical N-S and NW-SE striking fractures to show highest slip tendencies (Figure 5.2d), with 10 % of the fracture population exceeding the considered coefficient of static friction of $\mu = 0.67$. Highest dilation tendencies are associated with NNW-SSE trending fractures. The directional preferences for fluid flow in open fractures have been identified for the studied part of the Ruhr Basin.

To study if fault stability is affected by the flooding of abandoned hard coal mines in the eastern Ruhr Basin, a 3D structural model of Upper Carboniferous sequence has been constructed for the NE part of the water province “Haus Aden” (Figure 5.1b).

NNW-SSE to NW-SE trending normal faults (Figure 5.2e) are most susceptible for reactivation in a normal faulting regime, as indicated by slip tendency analysis for the structural inventory of the 3D model. Since hard coal mining activities were focused on inter-fault zones, two pore pressure scenarios arise: either the faults are affected by the mine water rebound up to a level of 640 m below ground, re-introducing low pore pressures (3.7 MPa at 1000 m below ground) (Figure 5.2f), or hydrostatic conditions still prevail. The probabilistic fault slip assessment (1000 realizations), conducted for the NNW-SSE to NW-SE trend of faults located around the “Heinrich Robert” colliery (as part of the water province “Haus Aden”), revealed low fault reactivation potential for considering two frictional fault strength thresholds ($\mu = 0.5$, $\mu = 0.67$) and hydrostatic pore pressure conditions ($T_S > \mu = 0.67$ in 5 % of the cases; $T_S > \mu = 0.5$ in 19 % of the cases) (Figure 5.2g). Conditions for fault reactivation are only reached for high differential stress in combination with hydrostatic pore pressure conditions.

Modeling the spatial variability of the frictional strength, performed for a chosen NNW-SSE trending normal fault, to better capture the heterogeneity is based on fault displacement and clay content of the faulted host rock. The derived frictional fault strength property fed into a fault stability analysis following the concept of the Failure Criterion Stress (FCS). It could be demonstrated that the majority (72.6 %) of the analyzed fault is stable ($FCS < 0$), beside minor unstable patches ($FCS > 0$). Stable conditions ($FCS < 0$) are associated with horizontally elongated patches of intermediate to high friction coefficients while unstable zones ($FCS > 0$) are linked to low friction coefficients. Considering an additional low cohesive fault strength (1 MPa), full-stable conditions are reached ($FCS > 0$). This is consistent with the findings of the probabilistic fault evaluation, demonstrating a low potential for flooding-related reactivation for the most exposed fault trend.

The stress control on fluid flow has been investigated in case of hydrocarbon migration along the Leopoldshafen fault that charged the former Leopoldshafen oil field, located in the central Upper Rhine Graben rift basin (Germany) (Figure 5.1c). The WNW-dipping normal fault structurally consists of two NNE-SSW trending segments that are linked by a left-stepping NNW-SSE to N-S striking bend segment (Figure 5.2h). The Cenozoic multi-level reservoir system is located in the footwall block at a depth of approximately

800 – 1200 m below ground. The fault bend segment was identified as the location along the analyzed fault that experienced highest slip and dilation tendency during the strike-slip faulting regime, active since the Miocene (Figure 5.2i). Associated fault activity has been investigated by modeling faulting-induced deformation for a set of possible slip vectors, ranging from pure sinistral strike-slip to oblique slip. The results highlight elevated volumetric (dilation) as well as longitudinal (e_1) strain magnitudes concentrated along the fault bend segment, suggesting that this part of the fault might have acted as a releasing bend (Figure 5.2j). It could be shown, that the fault bend segment might have provided a local pathway for up-dip hydrocarbon migration along the Leopoldshafen fault.

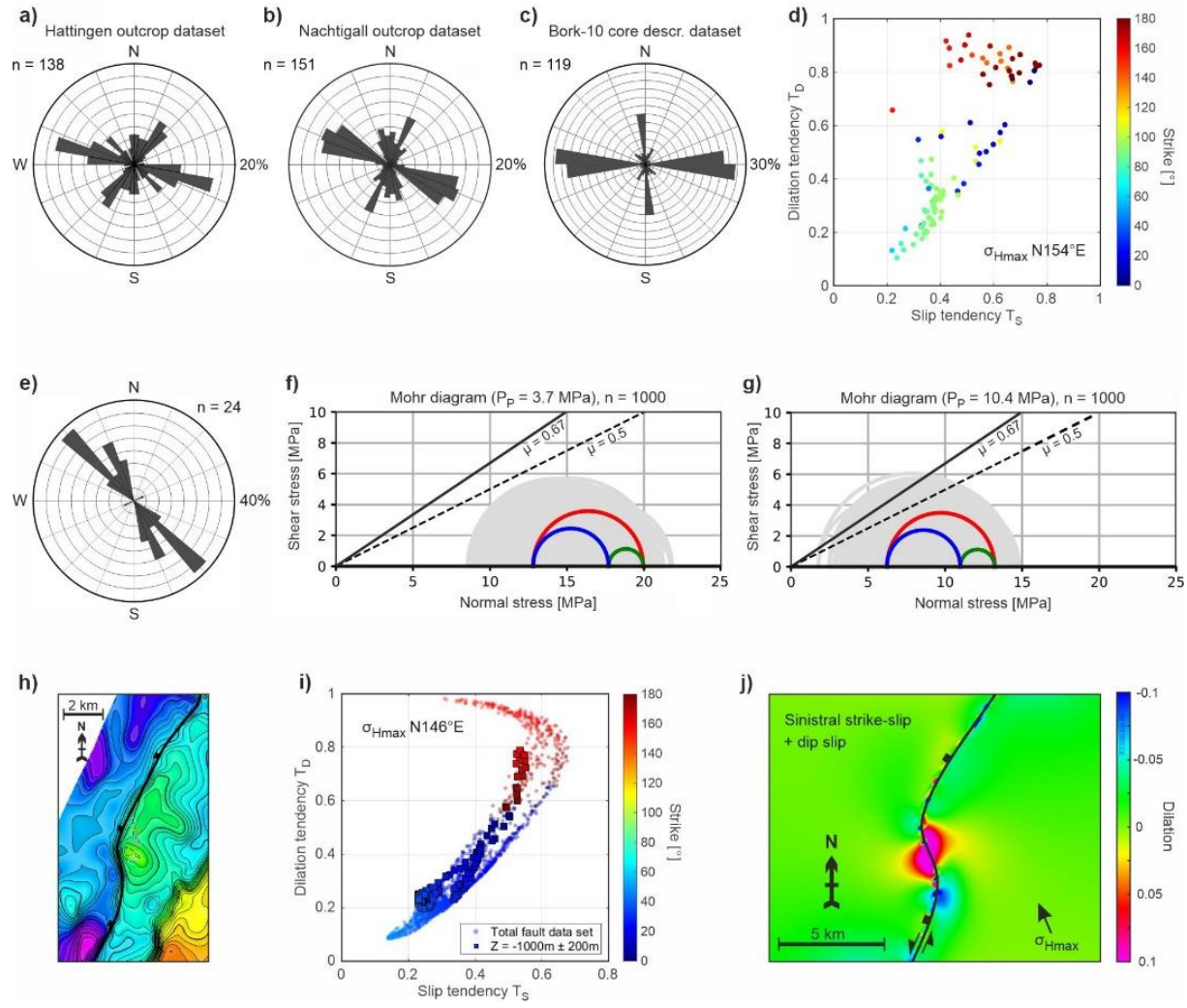

Figure 5.2: Orientation statistics of fractures hosted in Upper Carboniferous tight sandstones (Ruhr Basin, Germany) of the Hattingen (a) and Nachtigall outcrop (b) as well as the Bork10 core description data set (c) indicate comparable dominant orientation trends. d) Geomechanical analysis, utilizing the concepts of slip and dilation tendency, revealed N-S as well as NW-SE trending fractures as preferentially oriented to be hydraulically conductive. e) Orientation statistics of normal faults, mapped in the area of the "Heinrich-Robert" colliery (water province "Haus Aden", Ruhr Basin), served as input for the probabilistic fault slip assessment. f) Results of the probabilistic fault slip assessment indicate no reactivation potential for a mine water rebound up to a level of 640 m below depth. G) Stress conditions for fault reactivation under hydrostatic pore pressure conditions are given for high differential stresses, with the results indicate an overall low reactivation potential. h) The WNW-dipping Leopoldshafen fault with the bend segment visible on a depth structure map (Upper Rhine Graben, Germany). i) Fault Response Modelling indicates localized dilation around the fault bend segment, induced by sinistral oblique slip (strike-slip kinematics with an additional dip slip component). Thus, the fault bend segment might have acted as releasing bend associated with fault activity since the Miocene. j) The fault bend segment was subject to highest slip and dilation tendencies within the strike-slip stress field since the Miocene.

6 Conclusions and Outlook

6.1 Conclusions

The fracture inventory of Upper Carboniferous tight sandstones is studied based on two outcrops and one well dataset. Fracture detection, utilizing digital outcrop models of two Upper Carboniferous sandstone exposures (Kaisberg Sandstone, Namurian C; Finefrau Sandstone, Westphalian A) along the southern edge of the Ruhr Basin (Germany), revealed three dominant high-angle (w.r.t. bedding) fracture orientations: NNE-SSW to NE-SW (set 1), WNW-ESE (set 2), and NNW-SSE to N-S (set 3). The majority of the detected fractures are bed-restricted, indicating that bed thickness controls fracture geometry by limiting maximum fracture height. The fracture orientation statistics demonstrate comparable characteristics in both outcrops. Terzaghi-corrected averaged fracture intensities (P_{10}) vary between both outcrops for comparable fracture orientations, ranging from 0.4 to 3.1 m^{-1}. The Bork 10 well penetrates the Wesphalian A and provides a core description dataset that reveals two dominant N-S and W-E fracture trends alongside subordinate NW-SE and NNE-SSW fracture orientations. Linking the strike directions of the outcrop fractures to the subsurface fracture trends observed in the Bork 10 core description dataset indicates acceptable agreement. Outcrop-derived Terzaghi-corrected averaged fracture intensities (P_{10}) are 1.1 to 4.5 times higher than the P_{10} values for comparable fracture orientations observed in the Bork 10 well. This is attributed to the challenges of sampling (near-) parallel-aligned fractures relative to the horizontal outcrop alignment (if no additional obliquely oriented scanline can be taken) or the vertical wellbore configuration, as well as the surface stress relief of uplifted rocks exposed on the surface. The analysis of outcrop-derived fracture compared to fractures from cores clearly highlights the overall similarity in strike, but a dominance of high-angle fractures, respectively the lack of intermediate angle fractures, in outcrops.

Assuming fluid flow in stress-controlled open fractures, near-vertical N-S and NW-SE trending fractures are subject to highest slip tendencies within a strike-slip faulting regime (S_{Hmax} orientation of N154°E), partially being critically stressed depending on the considered static friction coefficient. Given their prevalence in the orientation statistics of the Bork 10 well core dataset, dominant N-S trending fractures play a primary role in controlling subsurface fluid flow. This might contribute to future geothermal exploration strategies as trajectory planning relies on identifying fracture orientations that are most likely to be hydraulically conductive.

A 3D structural model of the Upper Carboniferous subsurface of the NE part of the water province “Haus Aden” (eastern Ruhr Basin, Germany) is established, based on high-resolution subsurface mapping of coal seams in mines, that fed into a 2.5-dimensional coal resources calculation model. Flooding of abandoned hard coal mines might affect fault stability as stress conditions change. Slip tendency analysis performed based on the constructed structural 3D model, representing the structural inventory of the NE part of the

water province “Haus Aden”, identified NW-SE to NNW-SSE trending normal faults as the most susceptible fault trend for reactivation.

The fault reactivation potential for this identified fault trend is probabilistically assessed (for a depth level of 1000 m below ground, representing former mining levels) considering two pore pressure scenarios: either full hydrostatic and controlled by a mine water rebound up to a level of 640 m below ground. Under hydrostatic conditions, only a low fault reactivation potential is determined. The conditions required for causing fault reactivation are only reached for high differential stresses, but not when considering the mean principal stresses under both pore pressure scenarios for the two employed Mohr-Coulomb failure envelopes ($\mu = 0.5$, $\mu = 0.67$). The probabilistic approach accounts for the input parameter uncertainties associated with the stress model (including magnitudes and orientations) and geometric fault attributes (such as strike and dip). To capture the uncertainties related to the coefficient of static friction, representing the frictional strength of the analyzed faults, two scenarios are considered for the probabilistic fault slip assessment ($\mu = 0.5$, $\mu = 0.67$).

However, the frictional strength of faults can be heterogeneous by varying along strike and dip, which is aimed to be better captured by modeling this phenomenon. Generally, the tested approach is particularly interesting when a detailed analysis of specific areas along a fault is required (e.g. fluid injection scenarios), and the frictional fault strength cannot be adequately captured through a single friction coefficient. Utilizing the constructed friction coefficient fault property model as input for fault stability analysis of a selected NNW-SSE trending normal fault, results indicate predominantly stable, yet interspersed with unstable horizontally elongated patches along the fault surface. For additionally considering a low cohesive fault strength, stable conditions are reached along the entire fault surface. Since fault stability analysis usually assume cohesionless faults (e.g. the conducted probabilistic fault slip assessment), it provides an additional safety buffer and can therefore be regarded a conservative approach. Overall the indicated low reactivation potential is in agreement with the observation of no natural seismicity in the eastern Ruhr Basin, which might be beneficial for future fault-related geothermal applications in the Ruhr area.

The stress control on fluid migration pathways along a fault is exemplary shown for the fault-controlled hydrocarbon migration of the Leopoldshafen oil field located in the central Upper Rhine Graben (Germany). The Leopoldshafen fault was formed during the Oligocene phase of graben formation, as indicated by the Expansion Index analysis. The fault is composed of two NNE-SSW trending segments, connected by a left-stepping NNW-SSE to N-S trending fault bend segment. The highest slip and dilation tendencies were observed along the fault bend segment, underscoring its preferential alignment for fluid flow within the strike-slip fault regime that has characterized the Upper Rhine Graben since the Miocene. Fault activity extended into the Miocene, with the fault likely being reactivated with (oblique) sinistral strike-slip kinematics. Geomechanical simulation results show the bend segment to act as a releasing bend, allowing for vertical hydrocarbon migration. This constrains the hypothesis proposed by Bruss (2000) of fault-controlled

hydrocarbon migration into Cenozoic reservoirs in the central Upper Rhine Graben. Future exploration for deep geothermal and lithium brine mining in the Upper Rhine Graben might benefit from this structural understanding, as fault zones currently are the primary drilling target.

6.2 Outlook

To extend the data base on fractures hosted in the Upper Carboniferous sandstones as well as to enable spatial comparisons of fracture network attributes between outcrops throughout the Ruhr Basin, a follow-up study could incorporate additional sandstone exposures. Furthermore, emphasis could be placed on the influence of faults on fracture network attributes. By quantifying the fracture intensity as a function of the distance to faults, the empirically derived function could serve as input for the construction of fault-related DFN models. Additionally, the surface curvature of the folded Upper Carboniferous sequence could be studied as a potential predictor of fracture style and intensity, which would contribute to facilitate inter-well predictions for the construction of detailed DFN models (Jolley et al. 2007; Feng et al. 2018). Since fracture patterns can be controlled by mechanical stratigraphy (Ruf et al. 1998; Underwood et al. 2003; Wennberg et al. 2006), a follow-up study could focus on the relationship between fracture characteristics and mechanical properties to better understand the spatial fracture distribution in the Upper Carboniferous.

As matrix porosity and permeability in the studied area are low (Greve et al. 2023) the assessment of natural fractures and their specific influence on fluid migration should be the main focus of future work. Besides the assessment of the present-day stress control on preferential fracture orientations for hydraulic conductivity, chemical control on fracture conductivity might be studied to complete the greater picture. If suitable core material of wells penetrating the Upper Carboniferous is available, analysis of fracture cementation (sealed versus partially sealed or barren) could add crucial information on the directional dependency of barren or sealed fractures hosted in the sandstones of the Ruhr Basin.

In the context of the variability of the frictional fault strength, a modeling approach might provide the best possible approximation, as subsurface faults cannot be accessed and sampled. To increase the precision of the fault stability analysis, a case-tailored laboratory study (e.g. using Upper Carboniferous rock samples) of the friction coefficient as a function of the clay content is required. By taking case-specific lithological data as proxy, modeling the spatial variability of the frictional fault strength could be advantageous for a safer utilization of the subsurface, as fault stability can be assessed in greater detail.

To take up the use of geomechanical simulation approaches, the orientation and spatial distribution of faulting-related fractures could be modeled based on faulting-induced deformation. Since geothermal projects often target fault zones (e.g. Upper Rhine Graben, Germany), deep wells could provide fracture datasets

that could be utilized for model calibration. A successfully calibrated geomechanical model might be beneficial for the prediction of fracture orientation and spatial distribution in order to de-risk future geothermal exploration.

7 References

Aadnøy, B.; Bell, J. (1998): Classification of drilling-induced fractures and their relationship to in-situ stress directions. In *The Log Analyst* 39.

Agemar, T.; Weber, J.; Schulz, R. (2014): Deep Geothermal Energy Production in Germany. In *Energies* 7 (7), p. 4397–4416. DOI: 10.3390/en7074397.

Aghajanpour, A.; Qalandari, R.; Gholami, R. (2018): A study on natural fracture characterization for well trajectory design and production improvement: A case study from a tight gas reservoir, Australia. In *International Journal of Chemical Engineering and Applications* 9 (3), p. 82–87. DOI: 10.18178/ijcea.2018.9.3.703.

Aigner, T.; Bachmann, G. H. (1992): Sequence-stratigraphic framework of the German Triassic. In *Sedimentary Geology* 80 (1-2), p. 115–135. DOI: 10.1016/0037-0738(92)90035-P.

Alexander, L. L.; Handschy, J. W. (1998): Fluid Flow in a Faulted Reservoir System: Fault Trap Analysis for the Block 330 Field in Eugene Island, South Addition, Offshore Louisiana. In *AAPG Bulletin* 1998 (82), p. 387-411.

Allgaier, F.; Busch, B.; Niederhuber, T.; Quandt, D.; Müller, B.; Hilgers, C. (2023): Fracture network characterisation of the naturally fractured Upper Carboniferous sandstones combining outcrop and wellbore data, Ruhr Basin, Germany. In *Zeitschrift der Deutschen Gesellschaft für Geowissenschaften (Journal of Applied and Regional Geology)* 173 (4), p. 599–623. DOI: 10.1127/zdgg/2023/0369.

Allmendinger, R. (2023): Stereonet (version 11.5.1). Available online at https://www.rickallmendinger.net/stereonet, checked on 10/30/2023.

Ameen, M. S.; Buhidma, I. M.; Rahim, Z. (2010): The function of fractures and in-situ stresses in the Khuff reservoir performance, onshore fields, Saudi Arabia. In AAPG *Bulletin* 94 (1), p. 27–60. DOI: 10.1306/06160909012.

Ando, R.; Tada, T.; Yamashita, T. (2004): Dynamic evolution of a fault system through interactions between fault segments. In *Journal of Geophysical Research: Solid Earth* 109 (B5). DOI: 10.1029/2003JB002665.

Antics, M.; Papachristou, M.; Ungemach, P. (2005): Sustainable heat mining. A reservoir engineering approach. In Stanford University (Ed.): Proceedings of the 30th Workshop on Geothermal Reservoir Engineering. Thirtieth Workshop on Geothermal Reservoir Engineering. Stanford, California, 31.01.2005. Stanford University.

Aristizabal-H, Gustavo; Goerke-Mallet, Peter; Kretschmann, Jürgen; Restrepo-Baena, Oscar Jaime (2023): Sustainability of coal mining. Is Germany a post-mining model for Colombia? In *Resources Policy* 81, p. 103358. DOI: 10.1016/j.resourpol.2023.103358.

Arndt, M.; Fritschele, T.; Salamon, M.; Thiel, A. (2020): Das Rhenoherzynische Becken – ein hydrothermales Reservoir für NRW und Nordwesteuropa? In *scriptumonline* (16).

Ashman, I. R.; Faulkner, D. R. (2023): The effect of clay content on the dilatancy and frictional properties of fault gouge. In *Journal of Geophysical Research: Solid Earth* 128 (4), . DOI: 10.1029/2022JB025878.

Aydin, A. (2000): Fractures, faults, and hydrocarbon entrapment, migration and flow. In *Marine and Petroleum Geology* 17 (7), p. 797–814. DOI: 10.1016/S0264-8172(00)00020-9.

Bächler, D.; Kohl, T.; Rybach, L. (2003): Impact of graben-parallel faults on hydrothermal convection—Rhine Graben case study. In *Physics and Chemistry of the Earth, Parts A/B/C* 28 (9-11), p. 431–441. DOI: 10.1016/S1474-7065(03)00063-9.

Bagni, F. L.; Bezerra, F. H.; Balsamo, F.; Maia, R. P.; Dall'Aglio, M. (2020): Karst dissolution along fracture corridors in an anticline hinge, Jandaíra Formation, Brazil: Implications for reservoir quality. In *Marine and Petroleum Geology* 115, p. 104249. DOI: 10.1016/j.marpetgeo.2020.104249.

Balcewicz, M.; Ahrens, B.; Lippert, K.; Saenger, E. H. (2020): Characterization of fractures in potential reservoir rocks for geothermal applications in the Rhine-Ruhr metropolitan area (Germany). In *Solid Earth* 12 (1), p. 35-58. DOI: 10.5194/se-12-35-2021.

Balzer, I.; Roth, M. (2019): Mine water in the Ruhr Area - Opportunities for the future. In *Mining Report Glückauf* 2019 (155), p. 254–261.

Barr, D. (2007): Conductive faults and sealing fractures in the West Sole gas fields, southern North Sea. In *Geological Society, London, Special Publications* 292 (1), p. 431–451. DOI: 10.1144/SP292.23.

Bärtling, R. (1921): Transgression, Regression und Faziesverteilung in der Mittleren und Oberen Kreide des Beckens von Münster. In *Zeitschrift der Deutschen Geologischen Gesellschaft* 1921 (72), p. 161–217.

Barton, C. A.; Zoback, M. D.; Moos, D. (1995): Fluid flow along potentially active faults in crystalline rock. In *Geology* 23 (8), p. 683-686. DOI: 10.1130/0091-7613(1995)023%3C0683:FFAPAF%3E2.3.CO;2.

Barton, N.; Bandis, S.; Bakhtar, K. (1985): Strength, deformation and conductivity coupling of rock joints. In *International Journal of Rock Mechanics and Mining Sciences & Geomechanics Abstracts* 22 (3), p. 121–140. DOI: 10.1016/0148-9062(85)93227-9.

Baujard, C.; Rolin, P.; Dalmais, É.; Hehn, R.; Genter, A. (2021): Soultz-sous-Forêts Geothermal Reservoir: Structural Model Update and Thermo-Hydraulic Numerical Simulations Based on Three Years of Operation Data. In *Geosciences* 11 (12), p. 502. DOI: 10.3390/geosciences11120502.

Becker, I.; Busch, B.; Koehrer, B.; Adelmann, D.; Hilgers, C. (2019a): Reservoir quality evolution of Upper Carboniferous (Westphalian) tight gas sandstones, Lower Saxony Basin, NW Germany. In *Journal of Petroleum Geology* 42 (4), p. 371–392. DOI: 10.1111/jpg.12742.

Becker, I.; Koehrer, B.; Waldvogel, M.; Jelinek, W.; Hilgers, C. (2018): Comparing fracture statistics from outcrop and reservoir data using conventional manual and t-LiDAR derived scanlines in Ca2 carbonates from the Southern Permian Basin, Germany. In *Marine and Petroleum Geology* 95, p. 228–245. DOI: 10.1016/j.marpetgeo.2018.04.021.

Becker, I.; Müller, B.; Koehrer, B.; Jelinek, W.; Hilgers, C. (2019b): Present-day stress control on fluid migration pathways: Case study of the Zechstein fractured carbonates, NW-Germany. In *Marine and Petroleum Geology* 103, p. 320–330. DOI: 10.1016/j.marpetgeo.2019.03.002.

Becker, S.; Nguyen, H. T.; Nollet, S.; Fernandez-Steeger, T. M.; Laux, D.; Hilgers, C. (2014): Methods to analyse fracture orientation patterns in a Lower Carboniferous carbonate reservoir analogue in the Voreifel, Germany. In *Zeitschrift der Deutschen Gesellschaft für Geowissenschaften (Journal of Applied and Regional Geology)* 165 (3), p. 319–330. DOI: 10.1127/1860-1804/2014/0078.

Bedford, J. D.; Faulkner, D. R.; Lapusta, N. (2022): Fault rock heterogeneity can produce fault weakness and reduce fault stability. In *Nature communications* 13 (1), p. 326. DOI: 10.1038/s41467-022-27998-2.

Bense, V. F.; Person, M. A. (2006): Faults as conduit-barrier systems to fluid flow in siliciclastic sedimentary aquifers. In *Water Resources Research* 42 (5), DOI: 10.1029/2005WR004480.

Berger, J.-P.; Reichenbacher, B.; Becker, D.; Grimm, M.; Grimm, K.; Picot, L. et al. (2005a): Eocene-Pliocene time scale and stratigraphy of the Upper Rhine Graben (URG) and the Swiss Molasse Basin (SMB). In *International Journal of Earth Sciences (Geologische Rundschau)* 94 (4), p. 711–731. DOI: 10.1007/s00531-005-0479-y.

Berger, J.-P.; Reichenbacher, B.; Becker, D.; Grimm, M.; Grimm, K.; Picot, L. et al. (2005b): Paleogeography of the Upper Rhine Graben (URG) and the Swiss Molasse Basin (SMB) from Eocene to Pliocene. In *International Journal of Earth Sciences (Geologische Rundschau)* 94 (4), p. 697–710. DOI: 10.1007/s00531-005-0475-2.

Berkowitz, B. (2002): Characterizing flow and transport in fractured geological media: A review. In *Advances in Water Resources* 25 (8-12), p. 861–884. DOI: 10.1016/S0309-1708(02)00042-8.

Bigaroni, N.; Scuderi, M. M.; Cappa, F.; Guglielmi, Y.; Nussbaum, C.; Aldega, L. et al. (2022): Frictional properties of Opalinus Clay: influence of humidity, normal stress and grain size on frictional stability. In *Geophysical Journal International* 233 (1), p. 211–228. DOI: 10.1093/gji/ggac457.

Bisdom, K.; Gauthier, B.D.M.; Bertotti, G.; Hardebol, N. J. (2014): Calibrating discrete fracture-network models with a carbonate three-dimensional outcrop fracture network: Implications for naturally fractured reservoir modeling. In AAPG *Bulletin* 98 (7), p. 1351–1376. DOI: 10.1306/02031413060.

Böcker, J.; Littke, R. (2016): Thermal maturity and petroleum kitchen areas of Liassic Black Shales (Lower Jurassic) in the central Upper Rhine Graben, Germany. In *International Journal of Earth Sciences (Geologische Rundschau)* 105 (2), p. 611–636. DOI: 10.1007/s00531-015-1188-9.

Böcker, J.; Littke, R.; Forster, A. (2017): An overview on source rocks and the petroleum system of the central Upper Rhine Graben. In *International Journal of Earth Sciences (Geologische Rundschau)* 106 (2), p. 707–742. DOI: 10.1007/s00531-016-1330-3.

Bödvarsson, G. S.; Tsang, C. F. (1982): Injection and Thermal Breakthrough in Fractured Geothermal Reservoirs. In *Journal of Geophysical Research: Solid Earth* 87 (B2), p. 1031–1048. DOI: 10.1029/JB087iB02p01031.

Boigk, H. (1981): Erdöl und Erdölgas in der Bundesrepublik Deutschland. Erdölprovinzen, Felder, Förderung, Vorräte, Lagerstättentechnik. Stuttgart: Enke.

Bourquin, S.; Peron, S.; Durand, M. (2006): Lower Triassic sequence stratigraphy of the western part of the Germanic Basin (west of Black Forest): Fluvial system evolution through time and space. In *Sedimentary Geology* 186 (3-4), p. 187–211. DOI: 10.1016/j.sedgeo.2005.11.018.

Bredehoeft, J. D.; Belitz, K. (1992): The Hydrodynamics of the Big Horn Basin: A Study of the Role of Faults. In AAPG *Bulletin* 76. DOI: 10.1306/BDFF8862-1718-11D7-8645000102C1865D.

Brix, M. R.; Drozdzewski, G.; Greiling, R. O.; Wolf, R.; Wrede, V. (1988): The N Variscan margin of the Ruhr coal district (Western Germany): structural style of a buried thrust front? In *International Journal of Earth Sciences (Geologische Rundschau)* 77 (1), p. 115–126. DOI: 10.1007/BF01848679.

Brogi, A.; Alçiçek, M. C.; Liotta, D.; Capezzuoli, E.; Zucchi, M.; Matera, P. F. (2021): Step-over fault zones controlling geothermal fluid-flow and travertine formation (Denizli Basin, Turkey). In *Geothermics* 89, p. 101941. DOI: 10.1016/j.geothermics.2020.101941.

Bruss, D. (2000): Zur Herkunft der Erdöle im mittleren Oberrheingraben und ihre Bedeutung für die Rekonstruktion der Migrationsgeschichte und der Speichergesteine. Diss. Forschungszentrum Jülich. Universität Erlangen-Nürnberg.

Buchner, F. (1981): Rhinegraben: Horizontal stylolites indicating stress regimes of earlier stages of rifting. In *Tectonophysics* 73 (1-3), p. 113–118. DOI: 10.1016/0040-1951(81)90178-5.

Bücken, D.; Meier, T.; Backers, T. (2022): Geomechanische Auswirkungen saisonaler Wärmespeicherung in stillgelegten Bergwerken. In *Geomechanics and Tunnelling* 15 (1), p. 82–90. DOI: 10.1002/geot.202100085.

Büker, C. (1996): Absenkungs-, Erosions- und Wärmeflußgeschichte des Ruhr-Beckens und des nordöstlichen Rechtsrheinischen Schiefergebirges. Dissertation. Institut für Chemie und Dynamik der Geosphäre 4: Erdöl und organische Geochemie - Jülich.

Bundesministerium der Justiz (2019): Bundes-Klimaschutzgesetz vom 12. Dezember 2019 (BGBI. I S. 2513). KSG 2019. Available online at https://www.gesetze-im-internet.de/ksg/index.html, checked on 1/18/2022.

Busch, B.; Adelmann, D.; Herrmann, R.; Hilgers, C. (2022a): Controls on compactional behavior and reservoir quality in a Triassic Buntsandstein reservoir, Upper Rhine Graben, SW Germany. In *Marine and Petroleum Geology* 136, p. 105437. DOI: 10.1016/j.marpetgeo.2021.105437.

Busch, B.; Becker, I.; Koehrer, B.; Adelmann, D.; Hilgers, C. (2019): Porosity evolution of two Upper Carboniferous tight-gas-fluvial sandstone reservoirs: Impact of fractures and total cement volumes on reservoir quality. In *Marine and Petroleum Geology* 100, p. 376–390. DOI: 10.1016/j.marpetgeo.2018.10.051.

Busch, B.; Spitzner, A.; Adelmann, D.; Hilgers, C. (2022b): The significance of outcrop analog data for reservoir quality assessment: A comparative case study of Lower Triassic Buntsandstein sandstones in the Upper Rhine Graben. In *Marine and Petroleum Geology* 141, p. 105701. DOI: 10.1016/j.marpetgeo.2022.105701.

Büsche, E. (2014): Development of geothermal district heating in Germany. In *GRC Transactions* (38), p. 197–199. Available online at https://publications.mygeoenergynow.org/grc/1033535.pdf.

Bussmann, G.; Appelhans, K.; Hahn, F.; Jagert, F.; Bracke, R.; Seidel, T.; König, C. (2019): Reutilization of mine water for heating and cooling in the abandoned colliery Dannenbaum in Bochum. In *European Geothermal Congress*, p. 11–14.

Byerlee, J. (1978): Friction of rocks. In *Pure and Applied Geophysics* 116 (4-5), p. 615–626. DOI: 10.1007/BF00876528.

Caine, J. S.; Evans, J. P.; Forster, C. B. (1996): Fault zone architecture and permeability structure. In *Geology* 24 (11), p. 1025. DOI: 10.1130/0091-7613(1996)024%3C1025:FZAAPS%3E2.3.CO;2.

Cartwright, J. A.; Mansfield, C.; Trudgill, B. (1996): The growth of normal faults by segment linkage. In *Geological Society, London, Special Publication* 99 (1), p. 163–177. DOI: 10.1144/GSL.SP.1996.099.01.13.

Casas, N.; Mollon, G.; Daouadji, A. (2022): DEM analyses of cemented granular fault gouges at the onset of seismic sliding: Peak strength, development of shear zones and kinematics. In *Pure and Applied Geophysics* 179 (2), p. 679–707. DOI: 10.1007/s00024-021-02934-5.

Chabora, E.; Zemach, E.; Spielman, P.; Drakos, P.; Hickman, S.; Lutz, S. et al. (2012): Hydraulic stimulation of well 27-15, Desert Peak geothermal field, Nevada, USA. Stanford University, Stanford, California: Thirty-Seventh Workshop on Geothermal Reservoir Engineering.

Chapman, T. J.; Meneilly, A. W. (1991): The displacement patterns associated with a reverse-reactivated, normal growth fault. In *Geological Society, London, Special Publication* 56 (1), p. 183–191. DOI: 10.1144/GSL.SP.1991.056.01.12.

Cheng, C.; Milsch, H. (2021): Hydromechanical investigations on the self-propping potential of fractures in tight sandstones. In *Rock Mechanics and Rock Engineering*54 (10), p. 5407–5432. DOI: 10.1007/s00603-021-02500-4.

Chester, F. M.; Logan, J. M. (1987): Composite planar fabric of gouge from the Punchbowl Fault, California. In *Journal of Structural Geology* 9 (5-6), p. 621-634. DOI: 10.1016/0191-8141(87)90147-7.

Childs, C.; Manzocchi, T.; Walsh, J. J.; Bonson, C. G.; Nicol, A.; Schöpfer, M. P.J. (2009): A geometric model of fault zone and fault rock thickness variations. In *Journal of Structural Geology* 31 (2), p. 117–127. DOI: 10.1016/j.jsg.2008.08.009.

Childs, C.; Walsh, J. J.; Watterson, J. (1997): Complexity in fault zone structure and implications for fault seal prediction. In *Norwegian Petroleum Society Special Publications, Hydrocarbon Seals - Importance for Exploration and Production*, (7), p. 61–72. DOI: https://doi.org/10.1016/S0928-8937(97)80007-0.

Childs, C.; Watterson, J.; Walsh, J. J. (1995): Fault overlap zones within developing normal fault systems. In *Journal of the Geological Society* 152 (3), p. 535–549. DOI: 10.1144/gsjgs.152.3.0535.

Clavier, C.; Hoyle, W.; Meunier, D. (1971): Quantitative interpretation of thermal neutron decay time logs: Part I. Fundamentals and Techniques. In *Journal of Petroleum Technology* 23 (06), p. 743–755. DOI: 10.2118/2658-A-PA.

Collettini, C.; Tesei, T.; Scuderi, M. M.; Carpenter, B. M.; Viti, C. (2019): Beyond Byerlee friction, weak faults and implications for slip behavior. In *Earth and Planetary Science Letters* 519, p. 245–263. DOI: 10.1016/j.epsl.2019.05.011.

Committee on Fracture Characterization and Fluid Flow (1996): Rock fractures and fluid flow: Contemporary understanding and applications: The National Academies Press.

Cong, F.; Zhang, H.; Hao, F.; Xu, S. (2020): Direct control of normal fault in hydrocarbon migration and accumulation in northwestern Bozhong subbasin, Bohai Bay Basin, China. In *Marine and Petroleum Geology* 120, p. 104555. DOI: 10.1016/j.marpetgeo.2020.104555.

Cosgrove, J. W. (2015): The association of folds and fractures and the link between folding, fracturing and fluid flow during the evolution of a fold–thrust belt: a brief review. In *Geological Society, London, Special Publications* 421 (1), p. 41–68. DOI: 10.1144/SP421.11.

Cunningham, W. D.; Mann, P. (2007): Tectonics of strike-slip restraining and releasing bends. In *Geological Society, London, Special Publications* 290 (1), p. 1–12. DOI: 10.1144/SP290.1.

Dee, S. J.; Yielding, G.; Freeman, B.; Healy, D.; Kusznir, N. J.; Grant, N.; Ellis, P. (2007): Elastic dislocation modelling for prediction of small-scale fault and fracture network characteristics. In *Geological Society, London, Special Publications* 270 (1), p. 139–155. DOI: 10.1144/GSL.SP.2007.270.01.10.

Delogkos, E.; Manzocchi, T.; Childs, C.; Sachanidis, C.; Barbas, T.; Schöpfer, M. P. J. et al. (2017): Throw partitioning across normal fault zones in the Ptolemais Basin, Greece. In *Geological Society, London, Special Publications* 439 (1), p. 333–353. DOI: 10.1144/SP439.19.

Derer, C. E.; Schumacher, M. E.; Schäfer, A. (2005): The northern Upper Rhine Graben: basin geometry and early syn-rift tectono-sedimentary evolution. In *International Journal of Earth Sciences (Geologische Rundschau)* 94 (4), p. 640–656. DOI: 10.1007/s00531-005-0515-y.

Dershowitz, W. S. (1985): Rock joint systems, Ph.D. thesis. Cambridge, Massachusetts: Massachusetts Institute of Technology.

Dershowitz, W. S.; Herda, H. (1992): Interpretation of fracture spacing and intensity. In *International Journal of Rock Mechanics and Mining Sciences & Geomechanics Abstracts* 30 (4), p. A212. DOI: https://doi.org/10.1016/0148-9062(93)91769-F.

Deutsche Rohstoff (2012): RheinPetroleum schließt 3D-Seismikprogramm in Süddeutschland erfolgreich ab. Available online at https://rohstoff.de/rhein-petroleum-schliesst-3d-seismikprogramm-in-sueddeutschland-erfolgreich-ab/, checked on 3/13/2023.

Deutsche Stratigraphische Kommission (Hrsg.; Redation, Koordination und Gestaltung: Menning, M. & Hendrich, A.) (2016): Stratigraphische Tabelle von Deutschland 2016 (STD 2016). Potsdam (GeoForschungsZentrum).

Dezayes, C.; Genter, A.; Valley, B. (2010): Structure of the low permeable naturally fractured geothermal reservoir at Soultz. In *Comptes Rendus Geoscience* 342 (7-8), p. 517–530. DOI: 10.1016/j.crte.2009.10.002.

Dèzes, P.; Schmid, S. M.; Ziegler, P. A. (2004): Evolution of the European Cenozoic Rift System: interaction of the Alpine and Pyrenean orogens with their foreland lithosphere. In *Tectonophysics* 389 (1-2), p. 1–33. DOI: 10.1016/j.tecto.2004.06.011.

Diehl, T.; Kraft, T.; Kissling, E.; Wiemer, S. (2017): The induced earthquake sequence related to the St. Gallen deep geothermal project (Switzerland): Fault reactivation and fluid interactions imaged by microseismicity. In *Journal of Geophysical Research: Solid Earth* 122 (9), p. 7272–7290. DOI: 10.1002/2017JB014473.

Donnelly, L. J. (2006): A review of coal mining induced fault reactivation in Great Britain. In *Quarterly Journal of Engineering Geology and Hydrogeology* 39 (1), p. 5–50. DOI: 10.1144/1470-9236/05-015.

Donnelly, L. J.; Culshaw, M. G.; Bell, F. G. (2008): Longwall mining-induced fault reactivation and delayed subsidence ground movement in British coalfields. In *Quarterly Journal of Engineering Geology and Hydrogeology* 41 (3), p. 301–314. DOI: 10.1144/1470-9236/07-215.

Doubre, C.; Meghraoui, M.; Masson, F.; Lambotte, S.; Jund, H.; Bès de Berc, M.; Grunberg, M. (2021): Seismotectonics in Northeastern France and neighboring regions. In *Comptes Rendus. Géoscience* 353 (S1), p. 153–185. DOI: 10.5802/crgeos.80.

Drobniewski, M.; Balzer, I.; Frankenhoff, H.; Witthaus, H. (2017): Mine water management in the Ruhr coalfield. In *Mine Water & Circular Economy*, p. 183–189.

Drozdzewski, G. (2005): Zur sedimentären Entwicklung des Subvariscikums im Namurium und Westfalium Nordwestdeutschlands. In *Courier Forschungsinsitut Senckenberg* (254), p. 271–320.

Drozdzewski, G.; Jansen, F.; Kunz, E.; Pieper, B.; Rabitz, A.; Stehn, O.; Wrede, V. (1982): Geologisches Karte Ruhrkarbon 1:100 000. Krefeld: Geologisches Landesamt Nordrhein-Westfalen.

Drozdzewski, G.; Kunz, E.; Wrede, V.; Bornemann, O. (Eds.) (1980): Beiträge zur Tiefentektonik des Ruhrkarbons. Geologisches Landesamt Nordrhein-Westfalen. Krefeld.

Drozdzewski, G.; Wrede, V. (1994): Faltung und Bruchtektonik - Analyse der Tektonik im Subvariscikum. In Geologisches Landesamt Nordrhein-Westfalen (Ed.): Das Subvariscikum Nordwestdeutschlands. Struktur und Lagerstättenpotential eines Vorlandbeckens, vol. 38. Krefeld (Fortschritte in der Geologie von Rheinland und Westfalen, 38), p. 7–187.

Drozdzewski, Günter (1993): The Ruhr coal basin (Germany): structural evolution of an autochthonous foreland basin. In *International Journal of Coal Geology* 23 (1-4), p. 231–250. DOI: 10.1016/0166-5162(93)90050-K.

Drozdzewski, Günter Henscheid; Hoth, Peer; Juch, Dierk; Littke, Ralf; Vieth, Angelika; Wrede, Volker (2009): The pre-Permian of NW-Germany structure and coalification map. In *Zeitschrift der Deutschen Gesellschaft für Geowissenschaften (Journal of Applied and Regional Geology)* 160 (2), p. 159–172. DOI: 10.1127/1860-1804/2009/0160-0159.

Durst, H. (1991): Aspects of exploration history and structural style in the Rhine graben area. In A. M. Spencer (Ed.): Generation, accumulation, and production of Europe's hydrocarbons. Oxford: Oxford University Press (Special Publication of the European Association of Petroleum Geoscientists, 1), p. 247–261.

Edel, J.-B.; Schulmann, K.; Rotstein, Y. (2007): The Variscan tectonic inheritance of the Upper Rhine Graben: evidence of reactivations in the Lias, Late Eocene–Oligocene up to the recent. In *International Journal of Earth Sciences (Geologische Rundschau)* 96 (2), p. 305–325. DOI: 10.1007/s00531-006-0092-8.

Edwards, B.; Kraft, T.; Cauzzi, C.; Kastli, P.; Wiemer, S. (2015): Seismic monitoring and analysis of deep geothermal projects in St Gallen and Basel, Switzerland. In *Geophysical Journal International* 201 (2), p. 1022–1039. DOI: 10.1093/gji/ggv059.

Ehlig-Economides, C. A.; Taha, Mohamed; Marin, H. D.; Novoa, Enrique; Sanchez, O. (2000): Drilling and completion strategies in naturally fractured reservoirs. In *SPE International Petroleum Conference and Exhibition in Mexico*. Villahermosa, Mexico, 01.02.2000 - 03.02.2000: SPE.

Eisbacher, G. H.; Fielitz, W. (2010): Karlsruhe und seine Region. Nordschwarzwald, Kraichgau, Neckartal, Oberrhein-Graben, Pfälzerwald und westliche Schwäbische Alb. Stuttgart: Borntraeger (Sammlung geologischer Führer, Bd. 103).

Ekpo Johnson, E.; Scherwath, M.; Moran, K.; Dosso, S. E.; Rohr, K. M. (2023): Fault alip tendency analysis for a deep-sea basalt CO2 injection in the Cascadia Basin. In *GeoHazards* 4 (2), p. 121–135. DOI: 10.3390/geohazards4020008.

EnergieAgentur.NRW (2014): Machbarkeitsstudie Fernwärme im Ruhrgebiet. Für Energieeffizienz und Klimaschutz. EnergieAgentur.NRW. Düsseldorf.

European Commission (2020): Communication from the Commission to the European Parliament, The Council, The European Economic And Social Committee And The Committee Of The Regions - The European Green Deal.

Faulds, J. E.; Hinz, N. H. (2015): Favorable Tectonic and Structural Settings of Geothermal Systems in the Great Basin Region, Western USA: Proxies for Discovering Blind Geothermal Systems. In *Proceedings World Geothermal Congress*.

Feng, J.; Chang, L.; Zhao, L.; Li, X. (2018): Discrete fracture modeling of deep tight sandstone reservoir based on convergent multi-information—a case study of KX gas field in Tarim Basin. In *Arabian Journal of Geosciences* 11 (24). DOI: 10.1007/s12517-018-4123-0.

Ferrill, D. A.; Evans, M. A.; McGinnis, R. N.; Morris, A. P.; Smart, K. J.; Wigginton, S. S. et al. (2017a): Fault zone processes in mechanically layered mudrock and chalk. In *Journal of Structural Geology* 97, p. 118–143. DOI: 10.1016/j.jsg.2017.02.013.

Ferrill, D. A.; Morris, A. P.; McGinnis, R. N.; Smart, K. J.; Wigginton, S. S.; Hill, N. J. (2017b): Mechanical stratigraphy and normal faulting. In *Journal of Structural Geology* 94, p. 275–302. DOI: 10.1016/j.jsg.2016.11.010.

Ferrill, D. A.; Smart, K. J.; Morris, A. P. (2020a): Fault failure modes, deformation mechanisms, dilation tendency, slip tendency, and conduits v. seals. In *Geological Society, London, Special Publications* 496 (1), p. 75–98. DOI: 10.1144/SP496-2019-7.

Ferrill, D. A.; Smart, K. J.; Morris, A. P. (2020b): Resolved stress analysis, failure mode, and fault-controlled fluid conduits. In *Solid Earth* 11 (3), p. 899–908. DOI: 10.5194/se-11-899-2020.

Ferrill, D. A.; Winterle, J.; Wittmeyer, G.; Sims, D.; Colton, S.; Armstrong, A.; Morris, A. P. (1999): Stressed rock strains groundwater at Yucca Mountain, Nevada. In *GSA Today* (9), p. 1–8.

Finkbeiner, Thomas; Bertotti, Giovanni; Geiger, S. (2019): Introduction to the thematic collection: Naturally fractured reservoirs. In *Petroleum Geoscience* 25 (4), p. 351–353. DOI: 10.1144/petgeo2019-122.

Fossen, H. (2010): Structural Geology: Cambridge University Press.

Fossen, H. (2020): Fault classification, fault growth and displacement. In *Regional Geology and Tectonics: Principles of Geologic Analysis* (Elsevier), p. 119–147.

Fossen, H.; Rotevatn, A. (2016): Fault linkage and relay structures in extensional settings—A review. In *Earth-Science Reviews* 154, p. 14–28. DOI: 10.1016/j.earscirev.2015.11.014.

Franquet, J. A.; Krisadasima, S.; Bal, A.; Pantic, D. M. (2008): Critically-stressed fracture analysis contributes to determining the optimal drilling trajectory in naturally fractured reservoirs. In *International Petroleum Technology Conference. International Petroleum Technology Conference.* Kuala Lumpur, Malaysia, 2008-12-03: International Petroleum Technology Conference.

Freeman, S. R.; Harris, S. D.; Knipe, R. J. (2008): Fault seal mapping – incorporating geometric and property uncertainty. In *Geological Society, London, Special Publications* 309 (1), p. 5–38. DOI: 10.1144/SP309.2.

Freeman, S. R.; Harris, S. D.; Knipe, R. J. (2010): Cross-fault sealing, baffling and fluid flow in 3D geological models: tools for analysis, visualization and interpretation. In *Geological Society, London, Special Publications* 347 (1), p. 257–282. DOI: 10.1144/SP347.15.

Frey, M; Bär, K; Stober, I; Reinecker, J.; van der Vaart, J; Sass, I (2022): Assessment of deep geothermal research and development in the Upper Rhine Graben. In *Geothermal Energy* 10 (1). DOI: 10.1186/s40517-022-00226-2.

Fries, D.; Lebouil, S.; Maurer, V.; Martin, C.; Baujard, C.; Ravier, G. et al. (2022): Lithium extraction through pilot scale tests under real geothermal conditions of the Upper Rhine Graben. In *Proceedings European Geothermal Congress.*

Gale, J. F.W.; Laubach, S. E.; Olson, J. E.; Eichhuble, P.; Fall, A. (2014): Natural fractures in shale: A review and new observations. In *AAPG Bulletin* 98 (11), p. 2165–2216. DOI: 10.1306/08121413151.

Gawthorpe, R. L.; Leeder, M. R. (2000): Tectono-sedimentary evolution of active extensional basins. In *Basin Research* 12 (3-4), p. 195–218. DOI: 10.1046/j.1365-2117.2000.00121.x.

Genter, A.; Baujard, C.; Cuenot, N.; Dezayes, C.; Kohl, T.; Masson, F. et al. (2016): Geology, geophysics and geochemistry in the upper Rhine Graben: the frame for geothermal energy use. In *Proceedings European Geothermal Congress, EGC 2016*, September 19-24, 2016, Strasbourg, F: International Geothermal Association (IGA), Paper K-2.

Geologischer Dienst NRW (2020): Integrierte geologische Landesaufnahme in Nordrhein-Westfalen - Erläuterungen zum Kartierprojekt Ruhrgebiet. With assistance of B. Dölling, M. Dölling, A. Gawlik, M. Gellendin, M. Hiss, H. Hopp et al. Krefeld: Geologischer Dienst NRW.

geomecon GmbH (2022): KarboEx. Available online at http://karboex.geomecon.de/, checked on 1/31/2022.

Gholipour, A. M.; Cosgrove, J. W.; Ala, M. (2016): New theoretical model for predicting and modelling fractures in folded fractured reservoirs. In *Petroleum Geoscience* 22 (3), p. 257–280. DOI: 10.1144/petgeo2013-055.

Gillespie, P.; Monsen, E.; Maerten, L.; Hunt, D.; Thurmond, J.; Tuck, D. (2011): Fractures in Carbonates: From Digital Outcrops to Mechanical Models. In Ole J. Martinsen, Andrew J. Pulham, Peter D.W. Haughton, Morgan D. Sullivan (Eds.): Outcrops Revitalized: SEPM (Society for Sedimentary Geology), pp. 137–147.

Girardeau-Montaut, D. (2017): CloudCompare (version 2.10alpha). Available online at https://www.danielgm.net/cc/, checked on 10/11/2021.

Glaas, C.; Vidal, J.; Genter, A. (2021): Structural characterization of naturally fractured geothermal reservoirs in the central Upper Rhine Graben. In *Journal of Structural Geology* 148, p. 104370. DOI: 10.1016/j.jsg.2021.104370.

Greve, J.; Busch, B.; Quandt, D.; Knaak, M.; Hartkopf-Fröder, C.; Hilgers, C. (2023): Coupling heat conductivity and lithofacies of the coal-bearing Upper Carboniferous in the eastern Ruhr Basin, NW Germany. In *Journal of Applied and Regional Geology (Zeitschrift der Deutschen Gesellschaft für Geowissenschaften)* 173 (4), p. 673–695. DOI: 10.1127/zdgg/2023/0350.

Gruenthal, Gottfried; Bosse, Christian (1996): Probabilistische Karte der Erdbebengefaehrdung der Bundesrepublik Deutschland - Erdbebenzonierungskarte für das Nationale Anwendungsdokument zum Eurocode 8: Forschungsbericht.

Gunzburger, Y.; Cornet, F. H. (2007): Rheological characterization of a sedimentary formation from a stress profile inversion. In *Geophysical Journal International* 168 (1), p. 402–418. DOI: 10.1111/j.1365-246X.2006.03140.x.

Gupta, S.; Cowie, P. A.; Dawers, N. H.; Underhill, J. R. (1998): A mechanism to explain rift-basin subsidence and stratigraphic patterns through fault-array evolution. In *Geology* 26 (7), p. 595. DOI: 10.1130/0091-7613(1998)026%3C0595:AMTERB%3E2.3.CO;2.

Hahne, C.; Schmidt, R. (1982): Geologic conditions of the Westphalian-Lower Rhine coal district. Die Geologie des Niederrheinisch-Westphaelischen Steinkohlegebietes. Einführung in das Steinkohlengebirge und seine Montangeologie.

Hampson, Gary; Stollhofen, Harald; Flint, Steve (1999): A sequence stratigraphic model for the Lower Coal Measures (Upper Carboniferous) of the Ruhr district, north-west Germany. In *Sedimentology* 46 (6), p. 1199–1231. DOI: 10.1046/j.1365-3091.1999.00273.x.

Hanano, M. (2004): Contribution of fractures to formation and production of geothermal resources. In *Renewable and Sustainable Energy Reviews* 8 (3), p. 223–236. DOI: 10.1016/j.rser.2003.10.007.

Haney, M. M.; Snieder, R.; Sheiman, J.; Losh, S. (2005): Geophysics: a moving fluid pulse in a fault zone. In *Nature* 437 (7055), p. 46. DOI: 10.1038/437046a.

Harper, T. R.; Lundin, E. R. (1997): Fault seal analysis: reducing our dependence on empiricism. In *Norwegian Petroleum Society Special Publications, Hydrocarbon Seals - Importance for Exploration and Production* (7), p. 149–164.

Harstad, H.; Teufel, L. W.; Lorenz, J. C. (1995): Characterization and simulation of naturally fractured tight gas sandstone reservoirs. In *SPE Annual Technical Conference and Exhibition.* Dallas, Texas, 22.10.1995 - 25.10.1995: SPE.

Healy, D.; Hicks, S. P. (2022): De-risking the energy transition by quantifying the uncertainties in fault stability. In 13 (1), p. 15–39. DOI: 10.5194/se-13-15-2022.

Henstra, G. A.; Grundvåg, S.-A.; Johannessen, E. P.; Kristensen, T. B.; Midtkandal, I.; Nystuen, J. P. et al. (2016): Depositional processes and stratigraphic architecture within a coarse-grained rift-margin turbidite system: The Wollaston Forland Group, east Greenland. In *Marine and Petroleum Geology* 76, p. 187–209. DOI: 10.1016/j.marpetgeo.2016.05.018.

Hilden, H. D. (1995): Geologie im Münsterland. Krefeld.

Hilgers, C.; Dilg-Gruschinski, K.; Urai, J. L. (2004): Microstructural evolution of syntaxial veins formed by advective flow. In *Geology* 32 (3), p. 261. DOI: 10.1130/G20024.1.

Hinderfeld, G.; Kunz, E.; Opahle, M.; Stengel, H. (1993): Die Gasführung des Ruhrkarbons in ihrer räumlichen Verteilung und Entstehung zur Prognose der Ausgasung. Essen (DMT-Berichte aus Forschung und Entwicklung, 14).

Hooker, J. N.; Laubach, S. E.; Marrett, R. (2013): Fracture-aperture size—frequency, spatial distribution, and growth processes in strata-bounded and non-strata-bounded fractures, Cambrian Mesón Group, NW Argentina. In *Journal of Structural Geology* 54, p. 54–71. DOI: 10.1016/j.jsg.2013.06.011.

Hooper, E. C. D. (1991): Fluid migration along growth faults in compacting sediments. In *Journal of Petroleum Geology* 14, p. 161–180. DOI: 10.1111/j.1747-5457.1991.tb00360.x.

Hunfeld, L. B.; Niemeijer, A. R.; Spiers, C. J. (2017): Frictional Properties of Simulated Fault Gouges from the Seismogenic Groningen Gas Field Under In Situ P - T -Chemical Conditions. In *Journal of Geophysical Research: Solid Earth* 122 (11), p. 8969–8989. DOI: 10.1002/2017JB014876.

Iding, M.; Ringrose, P. (2010): Evaluating the impact of fractures on the performance of the In Salah CO2 storage site. In *International Journal of Greenhouse Gas Control* 4 (2), p. 242–248. DOI: 10.1016/j.ijggc.2009.10.016.

IEA (2020): Germany 2020. Energy Policy Review. IEA. Paris. Available online at https://www.iea.org/reports/germany-2020, checked on 2/1/2022.

Ikari, M. J.; Saffer, D. M.; Marone, C. (2009): Frictional and hydrologic properties of clay-rich fault gouge. In *Journal of Geophysical Research: Solid Earth* 114 (B5). DOI: 10.1029/2008JB006089.

Illies, J. H. (1972): The Rhine graben rift system-plate tectonics and transform faulting. In *Geophysical Surveys* (1), p. 27–60. DOI: 10.1007/BF01449550.

Illies, J. H. (1978): Two Stages Rhinegraben Rifting. In *Tectonics and Geophysics of Continental Rifts*. Dordrecht: Springer Netherlands, p. 63–71.

Jackson, C. A.-L.; Rotevatn, A. (2013): 3D seismic analysis of the structure and evolution of a salt-influenced normal fault zone: A test of competing fault growth models. In *Journal of Structural Geology* 54, p. 215–234. DOI: 10.1016/j.jsg.2013.06.012.

Jin, Y.-J.; Meng, L.-D.; Lyu, D.-Y.; Fu, X.-F.; Huang, J.-B.; Cao, S.-J.; Li, J.-D. (2023): Risk assessment of fault reactivation considering the heterogeneity of friction strength in the BZ34-2 Oilfield, Huanghekou Sag, Bohai Bay Basin, China. In *Petroleum Science* 20 (5), p. 2695–2708. DOI: 10.1016/j.petsci.2023.06.007.

Jolley, S. J.; Barr, D.; Walsh, J. J.; Knipe, R. J. (2007): Structurally complex reservoirs: an introduction. In *Geological Society, London, Special Publications* 292 (1), p. 1–24. DOI: 10.1144/SP292.1.

Juch, D.; Gaschnitz, R.; Thielemann, T. (2004): The influence of geological history on coal mine gas distribution in the Ruhr district - A challenge for future research and recovery. In *Geologica Belgica* 2004 (7/3-4), p. 191–199.

Juch, Dierk (1996): Assessment of West German hardcoal resources and its relation to coalbed methane. In *Geological Society, London, Special Publications* 109 (1), p. 59–65. DOI: 10.1144/GSL.SP.1996.109.01.05.

Kaldi, J.; Daniel, R.; Tenthorey, E.; Michael, K.; Schacht, U.; Nicol, A. et al. (2013): Containment of CO2 in CCS: Role of Caprocks and Faults. In *Energy Procedia* 37, p. 5403–5410. DOI: 10.1016/j.egypro.2013.06.458.

Kato, N.; Hirono, T. (2016): Heterogeneity in friction strength of an active fault by incorporation of fragments of the surrounding host rock. In *Earth, Planets and Space* 68 (1). DOI: 10.1186/s40623-016-0512-3.

Kelly, P. G.; Peacock, D. C. P.; Sanderson, D. J.; McGurk, A. C. (1999): Selective reverse-reactivation of normal faults, and deformation around reverse-reactivated faults in the Mesozoic of the Somerset coast. In *Journal of Structural Geology* 21 (5), p. 493–509. DOI: 10.1016/S0191-8141(99)00041-3.

Kinoshita, M.; Shiraishi, K.; Demetriou, E.; Hashimoto, Y.; Lin, W. (2019): Geometrical dependence on the stress and slip tendency acting on the subduction megathrust of the Nankai seismogenic zone off Kumano. In Progress in Earth and Planetary Science6 (1). DOI: 10.1186/s40645-018-0253-y.

Kinscher, J.; Namjesnik, D.; Contrucci, I.; Dominique, P.; Klein, E. (2018): Relevance of Seismic Risk Assessment in Abandoned Mining Districts: the Case of the Gardanne Coal Mine, Provence, France. In *12th International conference on mine closure (Mine Closure 2018), Leipzig, Germany*, pp. 615–624.

Klose, Christian D. (2007): Mine Water Discharge and Flooding: A Cause of Severe Earthquakes. In *Mine Water Environ* 26 (3), p. 172–180. DOI: 10.1007/s10230-007-0006-4.

Knipe, R.; Freeman, S.; Harris, S.; Davies, R. (2004): Structural Uncertainty and Scenario Modeling for Fault Seal Analysis. In *Proceedings AAPG Annual Meeting. 18-21 April. Dallas, Texas*.

Kohli, A. H.; Zoback, M. D. (2013): Frictional properties of shale reservoir rocks. In *Journal of Geophysical Research: Solid Earth* 118 (9), p. 5109–5125. DOI: 10.1002/jgrb.50346.

Kraml, M.; Jodocy, M.; Reinecker, J.; Leible, D.; Freundt, F.; Najem, S. et al. (2016): TRACE: Detection of Permeable Deep Reaching Fault Zone Sections in the Upper Rhine Graben, Germany, During Low Budget Isotope Geochemical Surface Exploration. In *European Geothermal Congress 2016*.

Kretschmann, J.; Efremenkov, A. B.; Khoreshok, A. A. (2017): From Mining to Post-Mining: The Sustainable Development Strategy of the German Hard Coal Mining Industry. In IOP Conference Series: Earth and Environmental Science 50, p. 12024. DOI: 10.1088/1755-1315/50/1/012024.

Kruszewski, M.; Klee, G.; Niederhuber, T.; Heidbach, O. (2022a): In situ stress database of the greater Ruhr region (Germany) derived from hydrofracturing tests and borehole logs. In *Earth System Science Data* 14 (12), p. 5367–5385. DOI: 10.5194/essd-14-5367-2022.

Kruszewski, M.; Montegrossi, G.; Backers, T.; Saenger, E. H. (2021): In situ stress state of the Ruhr Region (Germany) and its implications for permeability anisotropy. In *Rock Mechanics and Rock Engineering* (54), p. 6649-6663. DOI: 10.1007/s00603-021-02636-3.

Kruszewski, M.; Montegrossi, G.; Balcewicz, M.; Los Angeles Gonzalez Lucio, G. de; Igbokwe, Onyedika Anthony; Backers, Tobias; Saenger, E. H. (2022b): 3D in situ stress state modelling and fault reactivation risk exemplified in the Ruhr region (Germany). In *Geomechanics for Energy and the Environment* 32, p. 100386. DOI: 10.1016/j.gete.2022.100386.

Kruszewski, M.; Montegrossi, G.; Saenger, E. H. (2023): The risk of fluid-injection-induced fault reactivation in carbonate reservoirs: an investigation of a geothermal system in the Ruhr region (Germany). In *Geomechanics and Geophysics for Geo-Energy and Geo-Resources* 9 (1). DOI: 10.1007/s40948-023-00573-9.

La Pointe, Paul R.; Wallmann, Peter C.; Dershowitz, Williams S. (1993): Stochastic estimation of fracture size through simulated sampling. In *International Journal of Rock Mechanics and Mining Sciences & Geomechanics Abstracts* 30 (7), p. 1611–1617. DOI: 10.1016/0148-9062(93)90165-A.

Larssen, K.; Senger, K.; Grundvåg, S.-A. (2020): Fracture characterization in Upper Permian carbonates in Spitsbergen: A workflow from digital outcrop to geo-model. In *Marine and Petroleum Geology* 122, p. 104703. DOI: 10.1016/j.marpetgeo.2020.104703.

Laubach, S.; Marrett, R.; Olson, J. (2000): New directions in fracture characterization. In *The Leading Edge* 19 (7), p. 704–711. DOI: 10.1190/1.1438694.

Laubach, S. E. (1988): Subsurface fractures and their relationship to stress history in East Texas basin sandstone. In *Tectonophysics* 156 (1-2), p. 37–49. DOI: 10.1016/0040-1951(88)90281-8.

Laubach, S. E.; Lander, R. H.; Criscenti, L. J.; Anovitz, L. M.; Urai, J. L.; Pollyea, R. M. et al. (2019): The role of chemistry in fracture pattern development and opportunities to advance interpretations of geological materials. In *Reviews of Geophysics* 57 (3), p. 1065–1111. DOI: 10.1029/2019RG000671.

Laubach, S. E.; Olson, J. E.; Gale, J. F.W. (2004): Are open fractures necessarily aligned with maximum horizontal stress? In *Earth and Planetary Science Letters* 222 (1), p. 191–195. DOI: 10.1016/j.epsl.2004.02.019.

Le Carlier de Veslud, C.; Bourgeois, O.; Diraison, M.; Ford, M. (2005): 3D stratigraphic and structural synthesis of the Dannemarie basin (Upper Rhine Graben). In *Bulletin de la Société Géologique de France* 176 (5), p. 433–442. DOI: 10.2113/176.5.433.

Leckenby, R. J.; Lonergan, L.; Rogers, S. F.; Sanderson, D. J. (2007): Study of fracture-induced anisotropy from discrete fracture network simulation of well test responses. In *Geological Society, London, Special Publications* 270 (1), p. 117–137. DOI: 10.1144/GSL.SP.2007.270.01.09.

Lee, Hikweon; Shinn, Young Jae; Ong, See Hong; Woo, Sang Woo; Park, Kwon Gyu; Lee, Tae Jong; Moon, Seong Woo (2017): Fault reactivation potential of an offshore CO 2 storage site, Pohang Basin, South Korea. In *Journal of Petroleum Science and Engineering* 152, p. 427–442. DOI: 10.1016/j.petrol.2017.03.014.

Lei, Qinghua; Latham, John-Paul; Tsang, Chin-Fu (2017): The use of discrete fracture networks for modelling coupled geomechanical and hydrological behaviour of fractured rocks. In *Computers and Geotechnics* 85, p. 151–176. DOI: 10.1016/j.compgeo.2016.12.024.

Lewis, C. J.; Gardner, J. N.; Schultz-Fellenz, E. S.; Lavine, A.; Reneau, S. L.; Olig, S. (2009): Fault interaction and along-strike variation in throw in the Pajarito fault system, Rio Grande rift, New Mexico. In *Geosphere* 5 (3), p. 252–269. DOI: 10.1130/GES00198.1.

LGRB-Kartenviewer (2021): Regierungspräsidium Freiburg, Landesamt für Geologie, Rohstoffe und Bergbau. Available online at https://maps.lgrb-bw.de, checked on 3/9/2023.

Ligtenberg, J. H. (2005): Detection of fluid migration pathways in seismic data: implications for fault seal analysis. In *Basin Research* 17 (1), p. 141–153. DOI: 10.1111/j.1365-2117.2005.00258.x.

Linjordet, A.; Skarpnes, O. (1992): Application of horizontal stress directions interpreted from borehole breakouts recorded by four arm dipmeter tools. In *Arctic Geology and Petroleum Potential* (2), p. 681–690. DOI: https://doi.org/10.1016/B978-0-444-88943-0.50045-9.

Lohr, T.; Krawczyk, C. M.; Tanner, D. C.; Samiee, R.; Endres, H.; Oncken, O. et al. (2007): Strain partitioning due to salt: insights from interpretation of a 3D seismic data set in the NW German Basin. In *Basin Research* 19 (4), p. 579–597. DOI: 10.1111/j.1365-2117.2007.00338.x.

López, A. (2012): Andersonian and Coulomb stresses in Central Costa Rica and its fault slip tendency potential: new insights into their associated seismic hazard. In *Geological Society, London, Special Publications* 367 (1), p. 19–38. DOI: 10.1144/SP367.3.

Maerten, L.; Gillespie, P.; Daniel, J.-M. (2006): Three-dimensional geomechanical modeling for constraint of subseismic fault simulation. In AAPG *Bulletin* 90 (9), p. 1337–1358. DOI: 10.1306/03130605148.

Mahmoodpour, S.; Singh, M.; Bär, K.; Sass, I. (2022): Impact of well placement in the fractured geothermal reservoirs based on available discrete fractured system. In *Geosciences* 12 (1). DOI: https://doi.org/10.3390/geosciences12010019.

Mann, P. (2007): Global catalogue, classification and tectonic origins of restraining- and releasing bends on active and ancient strike-slip fault systems. In *Geological Society, London, Special Publications*290 (1), p. 13–142. DOI: 10.1144/SP290.2.

March, R.; Elder, H.; Doster, F.; Geiger, S. (2017): Accurate Dual-Porosity Modeling of CO2 Storage in Fractured Reservoirs. In *SPE Reservoir Simulation Conference*. Montgomery, Texas, USA, 20.02.2017 - 22.02.2017: SPE.

Mattila, J.; Tammisto, E. (2012): Stress-controlled fluid flow in fractures at the site of a potential nuclear waste repository, Finland. In *Geology* 40 (4), p. 299–302. DOI: 10.1130/G32832.1.

McClay, K. R. (1989): Analogue models of inversion tectonics. In *Geological Society, London, Special Publications* 44 (1), p. 41–59. DOI: 10.1144/GSL.SP.1989.044.01.04.

McClure, Mark W.; Horne, Roland N. (2014): An investigation of stimulation mechanisms in Enhanced Geothermal Systems. In *International Journal of Rock Mechanics and Mining Sciences* 72, p. 242–260. DOI: 10.1016/j.ijrmms.2014.07.011.

Meixner, J.; Schill, E.; Gaucher, E.; Kohl, T. (2014): Inferring the in situ stress regime in deep sediments: an example from the Bruchsal geothermal site. In *Geothermal Energy* 2 (1). DOI: 10.1186/s40517-014-0007-z.

Meng, L.; Fu, X.; Lv, Y.; Li, X.; Cheng, Y.; Li, T.; Jin, Y. (2017): Risking fault reactivation induced by gas injection into depleted reservoirs based on the heterogeneity of geomechanical properties of fault zones. In *Petroleum Geoscience* 23 (1), p. 29–38. DOI: 10.1144/petgeo2016-031.

Meschede, M.; Warr, L. N. (2019): The geology of Germany. A process-oriented approach. Cham, Switzerland: Springer (Regional geology reviews).

Michael, N. A.; Whittaker, A. C.; Allen, P. A. (2013): The Functioning of Sediment Routing Systems Using a Mass Balance Approach: Example from the Eocene of the Southern Pyrenees. In *The Journal of Geology* 121 (6), p. 581–606. DOI: 10.1086/673176.

Milad, Benmadi; Ghosh, Sayantan; Suliman, Mohamed; Slatt, Roger M. (2018): Upscaled DFN models to understand the effects of natural fracture properties on fluid flow in the Hunton Group tight Limestone. In *Proceedings of the 6th Unconventional Resources Technology Conference.* Unconventional Resources Technology Conference. Houston, Texas, USA, 23.07.2018 - 25.07.2018. Tulsa, OK, USA: American Association of Petroleum Geologists.

Miocic, J. M.; Johnson, G.; Gilfillan, S. M. V. (2020): Stress field orientation controls on fault leakage at a natural CO_2 reservoir. In *Solid Earth* 11 (4), p. 1361–1374. DOI: 10.5194/se-11-1361-2020.

Moeck, I.; Kwiatek, G.; Zimmermann, G. (2009): Slip tendency analysis, fault reactivation potential and induced seismicity in a deep geothermal reservoir. In *Journal of Structural Geology* 31 (10), p. 1174–1182. DOI: 10.1016/j.jsg.2009.06.012.

Moretti, I. (1998): The role of faults in hydrocarbon migration. In *Petroleum Geoscience* 4 (1), p. 81–94. DOI: 10.1144/petgeo.4.1.81.

Morris, A.; Ferrill, D. A.; Henderson, D. B. (1996): Slip-tendency analysis and fault reactivation. In *Geology* 24 (3), p. 275. DOI: 10.1130/0091-7613(1996)024%3C0275:STAAFR%3E2.3.CO;2.

Mösle, B.; Kukla, P.; Stollhofen, H.; Preuße, A. (2009): Coal bed methane production in the Münsterland Basin, Germany - Past and future. In *EGU General Assembly Conference Abstracts*, p. 4267.

Muchez, P.; Sintubin, M. (1998): Contrasting origin of palaeofluids in a strike-slip fault system. In *Chemical Geology* 145 (1-2), pp. 105–114. DOI: 10.1016/S0009-2541(97)00164-2.

Narr, W. (1996): Estimating average fracture spacing in subsurface rock. In *AAPG Bulletin* 80. DOI: 10.1306/64EDA0B4-1724-11D7-8645000102C1865D.

Narr, W.; Schechter, D. S.; Thompson, L. B. (2006): Naturally Fractured Reservoir Characterization: Society of Petroleum Engineers.

Nelson, R. A. (1985): Geologic analysis of naturally fractured reservoirs. Houston, Texas: Gulf Professional Publishing.

Niederhuber, T.; Kruszewski, M.; Röckel, T.; Rische, M.; Alber, M.; Müller, B. (2023a): Stress orientations from hydraulic fracturing tests in the Ruhr area in comparison to stress orientations from borehole observations and earthquake focal mechanism. In *Journal of Applied and Regional Geology (Zeitschrift der Deutschen Gesellschaft für Geowissenschaften)* 173 (4), p. 625–635. DOI: 10.1127/zdgg/2022/0352.

Niederhuber, T.; Rische, M.; Röckel, T.; Müller, B.; Schilling, F. (2023b): Flooding Induced Seismicity in the Ruhr Area – a geomechanics numerical modelling approach.

Nixon, C. W.; Nærland, K.; Rotevatn, A.; Dimmen, V.; Sanderson, D. J.; Kristensen, T. B. (2020): Connectivity and network development of carbonate-hosted fault damage zones from western Malta. In *Journal of Structural Geology* 141, p. 104212. DOI: 10.1016/j.jsg.2020.104212.

Nixon, C. W.; Vaagan, S.; Sanderson, D. J.; Gawthorpe, R. L. (2019): Spatial distribution of damage and strain within a normal fault relay at Kilve, U.K. In *Journal of Structural Geology* 118, p. 194–209. DOI: 10.1016/j.jsg.2018.10.016.

Noël, C.; Baud, P.; Violay, M. (2021): Effect of water on sandstone's fracture toughness and frictional parameters: Brittle strength constraints. In *International Journal of Rock Mechanics and Mining Sciences* 147, p. 104916. DOI: 10.1016/j.ijrmms.2021.104916.

Odling, N. E.; Gillespie, P.; Bourgine, B.; Castaing, C.; Chiles, J. P.; Christensen, N. P. et al. (1999): Variations in fracture system geometry and their implications for fluid flow in fractures hydrocarbon reservoirs. In *Petroleum Geoscience* 5 (4), p. 373–384. DOI: 10.1144/petgeo.5.4.373.

Ogilvie, S. R.; Dee, S. J.; Wilson, R. W.; Bailey, W. R. (2020): Integrated Fault Seal Analysis: An Introduction. In *Geological Society, London, Special Publications* 496 (1), p. 1–8. DOI: 10.1144/SP496-2020-51.

Orlic, B.; Heege, J. ter; Wassing, B. (2011): Assessing the integrity of fault- and top seals at CO2 storage sites. In *Energy Procedia* 4, p. 4798–4805. DOI: 10.1016/j.egypro.2011.02.445.

Oswald, T.; Salamon, M.; Strozyk, F. (2021): Erkundung der Potenziale für die Tiefengeothermie am Standort des Kraftwerkes Weisweiler der RWE Power AG. In *Erdöl, Erdgas, Kohle* 2021 (3), p. 24–26.

Peacock, D. C. P. (2002): Propagation, interaction and linkage in normal fault systems. In *Earth-Science Reviews* 58 (1-2), p. 121–142. DOI: 10.1016/S0012-8252(01)00085-X.

Pena-Castellnou, S.; Hürtgen, J.; Baize, S.; Preusser, F.; Mueller, D.; Jomard, H. et al. (2023): First Evidence of Surface Rupturing Earthquakes in the Eastern Rhine Graben Boundary Fault (Germany). DOI: 10.2139/ssrn.4472340.

Perner, M.; Jäger, H.; Reinhold, C.; Bechstädt, T.; Stinnesbeck, W. (2018): Impact of rift dynamics on palaeoenvironmental conditions and hydrocarbon system development (northern Upper Rhine Graben, SW Germany). In *Petroleum Geoscience* 24 (4), p. 425–439. DOI: 10.1144/petgeo2016-148.

Person, M.; Raffensperger, J. P.; Ge, S.; Garven, G. (1996): Basin-scale hydrogeologic modeling. In *Review of Geophysics* 34 (1), p. 61–87. DOI: 10.1029/95RG03286.

Peters, G.; Buchmann, T. J.; Connolly, P.; van Balen, R. T.; Wenzel, F.; Cloetingh, S. A. P. L. (2005): Interplay between tectonic, fluvial and erosional processes along the Western Border Fault of the northern Upper Rhine Graben, Germany. In *Tectonophysics* 406 (1-2), p. 39–66. DOI: 10.1016/j.tecto.2005.05.028.

Pienkowski, G.; Schudack, M. E.; Bosak, P.; Enay, R.; Feldman-Olszewska, A.; Golonka, J. et al. (2008): Jurassic. In T. McCann (Ed.): The Geology of Central Europe Volume 2: Mesozoic and Cenozoic: The Geological Society of London, p. 823–922.

Pilger, A. (1956): Tectonic orientations of Carboniferous deposits of the Ruhr region and their relationship with folding. In *Zeitschrift der Deutschen Geologischen Gesellschaft* 107, p. 206–230. DOI: 10.1127/zdgg/107/1956/206.

Pochat, S.; Castelltort, S.; Choblet, G.; van den Driessche, J. (2009): High-resolution record of tectonic and sedimentary processes in growth strata. In *Marine and Petroleum Geology* 26 (8), p. 1350–1364. DOI: 10.1016/j.marpetgeo.2009.06.001.

Pramer, P. (2021): Ein warmes Becken im Untergrund soll künftig Wien heizen. In *der Standard*, 12/6/2021. Available online at https://www.derstandard.at/story/2000131665321/ein-warmes-becken-im-untergrund-soll-kuenftig-wien-heizen, checked on 2/1/2022.

Priest, S. D. (1993): Discontinuity Analysis for Rock Engineering. Dordrecht: Springer Netherlands.

Questiaux, J.-M.; Couples, G. D.; Ruby, N. (2010): Fractured reservoirs with fracture corridors. In *Geophysical Prospecting* 58 (2), p. 279–295. DOI: 10.1111/j.1365-2478.2009.00810.x.

RAG AG (2014): Konzept zur langfristigen Optimierung der Grubenwasserhaltung der RAG Aktiengesellschaft für Nordrhein-Westfalen gemäß §4 Erblastenvertrag zur Bewältigung der Ewigkeitslasten des Steinkohlebergbaus der RAG AG im Rahmen der sozialverträglichen Beendigung des subventionierten Steinkohlenbergbaus in Deutschland vom 14.08.2007. Herne: RAG AG.

RAG-BID (2023): Ruhrkohle AG, Bürger Informations Dienst, Grubenwasser Monitoring. Available online at https://geodaten.rag.de/mapapps/resources/apps/bid/index.html?lang=de, checked on 10/30/2023.

Ramsay J. G.; Huber M. I. (1987): The Techniques of Modern Structural Geology. Volume 2: Folds and Fractures. Cambridge, Massachusetts: Academic Press.

Reicherter, K.; Pena-Castellnou, S.; Hürtgen, J.; Baize, S.; Ritter, J. (2021): Surface rupturing earthquakes in the Upper Rhine Graben: results from paleoseismological trenching. In *10th International INQUA Meeting, Antofagasta, Chile*.

Reinhold, C.; Schwarz, M.; Perner, M. (2016): The Northern Upper Rhine Graben: re-dawn of a mature petroleum province? In *Swiss Bulletin for Applied Geology* 21 (2). DOI: 10.5169/seals-658196.

Richard, P.; Bazalgette, L.; Al-Kindi, M. (2014): North Oman fault geometries in outcrops, analogues and subsurface. In *Geological Society, London, Special Publications* 392 (1), p. 447–460. DOI: 10.1144/SP392.21.

Richter, A. (2019): Replacing coal heating with geothermal in North Rhine-Westphalia (NRW). In *ThinkGeoEnergy*, 2/28/2019. Available online at https://www.thinkgeoenergy.com/replacing-coal-heating-with-geothermal-in-north-rhine-westphalia-nrw/, checked on 2/1/2022.

Richter, A. (2021): Another geothermal heating project to kick off within larger area of Paris, France. In *ThinkGeoEnergy*, 2/18/2021. Available online at https://www.thinkgeoenergy.com/another-geothermal-heating-project-to-kick-off-within-larger-area-of-paris-france/, checked on 2/1/2022.

Richter, A. (2022): City of Hamburg, Germany starts drilling on geothermal project. In *ThinkGeoEnergy*, 2/27/2022. Available online at https://www.thinkgeoenergy.com/city-of-hamburg-germany-starts-drilling-on-geothermal-project/, checked on 2/1/2022.

Richter, D. (1971): Ruhrgebiet und Bergisches Land. Zwischen Ruhr und Wupper. Berlin-Stuttgart: Gebrüder Borntträger.

Rider, M.; Kennedy, M. (2011): The Geological Interpretation of Well Logs. 3rd ed. Glasgow: Rider-French Consulting Ltd.

Rische, M.; Fischer, K. D.; Friederich, W. (2021): Induced micro seismicity due to raising mine water level in former coal mines in the eastern Ruhr area (Germany). With assistance of FID GEO: FID GEO.

Rische, M.; Fischer, K. D.; Friederich, W. (2023): FloodRisk – Induced seismicity by mine flooding – Observation, characterisation and relation to mine water rise in the eastern Ruhr area (Germany). In *Journal of Applied and Regional Geology (Zeitschrift der Deutschen Gesellschaft für Geowissenschaften)* 173 (4), p. 551–564. DOI: 10.1127/zdgg/2023/0346.

Ritz, J.-F.; Baize, S.; Audin, L.; Authémayou, C.; Graveleau, F.; Kaub, C. et al. (2021): New perspectives in studying active faults in metropolitan France: the “Active faults France” (FACT/ATS) research axis from the Resif-Epos consortium. In *Comptes Rendus. Géoscience* 353 (S1), p. 381–412. DOI: 10.5802/crgeos.98.

Rotevatn, A.; Bastesen, E. (2014): Fault linkage and damage zone architecture in tight carbonate rocks in the Suez Rift (Egypt): implications for permeability structure along segmented normal faults. In *Geological Society, London, Special Publications* 374 (1), p. 79–95. DOI: 10.1144/SP374.12.

Rotevatn, A.; Jackson, C. A.-L.; Tvedt, A. B. M.; Bell, Rebecca E.; Blækkan, I. (2019): How do normal faults grow? In *Journal of Structural Geology* 125, p. 174–184. DOI: 10.1016/j.jsg.2018.08.005.

Rotevatn, A.; Peacock, D. C. P. (2018): Strike-slip reactivation of segmented normal faults: Implications for basin structure and fluid flow. In *Basin Research* 30 (6), p. 1264–1279. DOI: 10.1111/bre.12303.

Rotstein, Y.; Behrmann, J. H.; Lutz, M.; Wirsing, G.; Luz, A. (2005): Tectonic implications of transpression and transtension: Upper Rhine Graben. In *Tectonics* 24 (6), n/a-n/a. DOI: 10.1029/2005TC001797.

Rotstein, Y.; Schaming, M. (2011): The Upper Rhine Graben (URG) revisited: Miocene transtension and transpression account for the observed first-order structures. In *Tectonics* 30 (3). DOI: 10.1029/2010TC002767.

rubitec GmbH (2003): Machbarkeitsstudie zur Erschließung tiefengeothermischer Energie durch Niederbringung eines Wärmetauschers bis 4.000m Tiefe (Hot-Dry-Rock-Verfahren).

Ruf, J. C.; Rust, K. A.; Engelder, T. (1998): Investigating the effect of mechanical discontinuities on joint spacing. In *Tectonophysics* (295), p. 245–257. DOI: https://doi.org/10.1016/S0040-1951(98)00123-1.

Samantray, A.; Kraaijveld, M.; Bulushi, W.; Spring, L. (2010): Interpretation and Application of Borehole Image Logs in a New Generation of Reservoir Models for a Cluster of Fields in Southern Oman. In M. Pöppelreiter, C. García-Carballido, M. Kraaijveld (Eds.): Dipmeter and Borehole Image Log Technology: American Association of Petroleum Geologists, p. 1–15.

Sanderson, D. J.; Nixon, C. W. (2015): The use of topology in fracture network characterization. In *Journal of Structural Geology* 72, p. 55–66. DOI: 10.1016/j.jsg.2015.01.005.

Sauer, K.; Nägele, R. (1981): Geothermische Synthese des Oberrheingrabens zwischen Karlsruhe und Mannheim (Anteil Baden-Württemberg): Bestandsaufnahme. Freiburg i. Br.

Schad, A. (1962): Voraussetzungen für die Bildung von Erdöllagerstätten im Rheingraben: Separatdruck.

Schäfer, A. (2019): Klastische Sedimente. Berlin, Heidelberg: Springer Berlin Heidelberg.

Scheidat, L.; Kirsch, F. J. (2000): The Ost colliery; Das Steinkohlenbergwerk Ost. In *Glueckauf* 2000 (136), p. 11–16.

Schleicher, A. M.; Warr, L. N.; van der Pluijm, B. A. (2006): Fluid focusing and back-reactions in the uplifted shoulder of the Rhine rift system: a clay mineral study along the Schauenburg Fault zone (Heidelberg, Germany). In *nternational Journal of Earth Sciences (Geologische Rundschau)* 95 (1), p. 19–33. DOI: 10.1007/s00531-005-0490-3.

Schumacher, M. E. (2002): Upper Rhine Graben: Role of preexisting structures during rift evolution. In *Tectonics* 21 (1), p. 6-1-6-17. DOI: 10.1029/2001TC900022.

Shapiro, S. A. (2015): Fluid-Induced Seismicity: Cambridge University Press.

Shen, B.; Barton, N. (2018): Rock fracturing mechanisms around underground openings. In *Geomechanics and Engineering* 2018 (16), p. 35–47. DOI: http://dx.doi.org/10.12989/gae.2018.16.1.035.

Shipton, Z. K.; Cowie, P. A. (2001): Damage zone and slip-surface evolution over μm to km scales in high-porosity Navajo sandstone, Utah. In *Journal of Structural Geology* 23 (12), p. 1825–1844. DOI: 10.1016/S0191-8141(01)00035-9.

Sibson, R. H. (1996): Structural permeability of fluid-driven fault-fracture meshes. In *Journal of Structural Geology* 18 (8), p. 1031–1042. DOI: 10.1016/0191-8141(96)00032-6.

Smeraglia, L.; Fabbi, S.; Billi, A.; Carminati, E.; Cavinato, G. P. (2022): How hydrocarbons move along faults: Evidence from microstructural observations of hydrocarbon-bearing carbonate fault rocks. In *Earth and Planetary Science Letters* 584, p. 117454. DOI: 10.1016/j.epsl.2022.117454.

Sokol, G.; Nitsch, E.; Anders, B.; Beccaletto, L.; Capar, L.; Mermy, D. C. et al. (2013): Geopotenziale des tieferen Untergrundes im Oberrheingraben, Fachlich- Technischer Abschlussbericht des INTERREG-Projekts GeORG, Teil 3: Daten, Methodik, Darstellungsweise. Freiburg i. Br.

Stach, E. (1923): Horizontalverschiebungen und Sprünge im östlichen Ruhrkohlengebiet. In *Glückauf* 1923 (59), p. 669–678.

Statistik der Kohlenwirtschaft e.V. (2019): Der Kohlenbergbau in der Energiewirtschaft der Bundesrepublik Deutschland im Jahre 2018. Statistik der Kohlenwirtschaft e.V. Essen, Bergheim. Available online at https://kohlenstatistik.de/publikationen/, checked on 10/27/2023.

Stelling, W.; Rummel, F. (1992): Messung von Primärspannungen durch Hydraulik-Fracturing auf dem Bergwerk Haus Aden. In *Das Markscheidewesen* 99 (1), p. 176–184.

Stephen, F. C. (2005): Coupling between Deformation, Fluid Pressures, and Fluid Flow in Ore-Producing Hydrothermal Systems at Depth in the Crust. In *Economic Geology, 100th Anniversary Volume*, p. 39–76.

Stoeckert, F.; Solibida, M.; Alber, M. (2020): Hydraulic fractures in discontinuous, anisotropic and heterogeneous rock - A lab study: ISRM International Symposium - EUROCK 2020, 6/14/2020.

Streit, J. E.; Hillis, R. R. (2004): Estimating fault stability and sustainable fluid pressures for underground storage of CO2 in porous rock. In *Energy* 29 (9-10), p. 1445–1456. DOI: 10.1016/j.energy.2004.03.078.

Suess, M. Peter; Drozdzewski, Guenter; Schaefer, Andreas (2007): Sedimentary environment dynamics and the formation of coal in the Pennsylvanian Variscan foreland in the Ruhr Basin (Germany, Western Europe). In *International Journal of Coal Geology* 69 (4), p. 267–287. DOI: 10.1016/j.coal.2006.05.003.

Sylvester, A. G. (1988): Strike-slip faults. In *GSA Bulletin* 100 (11), p. 1666–1703. DOI: 10.1130/0016-7606(1988)100%3C1666:SSF%3E2.3.CO;2.

Takahashi, M.; Mizoguchi, K.; Kitamura, K.; Masuda, K. (2007): Effects of clay content on the frictional strength and fluid transport property of faults. In *Journal of Geophysical Research: Solid Earth* 112 (B8). DOI: 10.1029/2006JB004678.

Tembe, S.; Lockner, D. A.; Wong, T.-F. (2010): Effect of clay content and mineralogy on frictional sliding behavior of simulated gouges: Binary and ternary mixtures of quartz, illite, and montmorillonite. In *Journal of Geophysical Research: Solid Earth* 115 (B3). DOI: 10.1029/2009JB006383.

Tenthorey, E.; Cox, S. F. (2006): Cohesive strengthening of fault zones during the interseismic period: An experimental study. In *Journal of Geophysical Research: Solid Earth* 111 (B9). DOI: 10.1029/2005JB004122.

Terzaghi, R. D. (1965): Sources of error in joint surveys. In *Géotechnique* 15 (3), p. 287–304. DOI: 10.1680/geot.1965.15.3.287.

Thorsen, C. E. (1963): Age of growth faulting in Southeast Louisiana. In *Transactions of the Gulf Coast Association of Geological Societies* (13), p. 103–110.

Tingay, M.; Reinecker, J.; Müller, B. (2008): Borehole breakout and drilling-induced fracture analysis from image logs. In *World Stress Map Project - guidelines: Image Logs*.

Torabi, A.; Alaei, B.; Libak, A. (2019): Normal fault 3D geometry and displacement revisited: Insights from faults in the Norwegian Barents Sea. In *Marine and Petroleum Geology* 99, p. 135–155. DOI: 10.1016/j.marpetgeo.2018.09.032.

Underwood, C. A.; Cooke, M. L.; Simo, J. A.; Muldoon, M. A. (2003): Stratigraphic controls on vertical fracture pattern I Silurian dolomite, northeastern Wisconsin. In *AAPG Bulletin* (295), p. 121–141.

Vadacca, L.; Rossi, D.; Scotti, A.; Buttinelli, M. (2021): Slip Tendency Analysis, Fault Reactivation Potential and Induced Seismicity in the Val d'Agri Oilfield (Italy). In *Journal of Geophysical Research: Solid Earth* 126 (1), Article 2019JB019185. DOI: 10.1029/2019JB019185.

van der Voet, Eva; Laenen, Ben; Rombaut, Bernd; Kourta, Mourad; Swennen, Rudy (2020): Fracture characteristics of Lower Carboniferous carbonates in northern Belgium based on FMI log analyses. In *Netherlands Journal of Geosciences* 99. DOI: 10.1017/njg.2020.6.

Verberne, B. A.; He, C.; Spiers, C. J. (2010): Frictional Properties of Sedimentary Rocks and Natural Fault Gouge from the Longmen Shan Fault Zone, Sichuan, China. In *Bulletin of the Seismological Society of America* 100 (5B), p. 2767–2790. DOI: 10.1785/0120090287.

Verma, N. K.; Al-Medhadi, F.; Franquet, J. A.; Maddock, R. H.; Dakshinamurthy, N.; AL-Mayyas, E. A. (2007): Critically stressed fracture analysis in naturally fractured carbonate reservoir - A case study in West Kuwait. In *SPE Middle East Oil and Gas Show and Conference*. Manama, Bahrain, 11.03.2007 - 14.03.2007: SPE.

Vidal, J.; Genter, A. (2018): Overview of naturally permeable fractured reservoirs in the central and southern Upper Rhine Graben: Insights from geothermal wells. In *Geothermics* 74, p. 57–73. DOI: 10.1016/j.geothermics.2018.02.003.

Vo Thanh, H.; Sugai, Y.; Nguele, R.; Sasaki, K. (2019): Integrated workflow in 3D geological model construction for evaluation of CO2 storage capacity of a fractured basement reservoir in Cuu Long Basin, Vietnam. In *International Journal of Greenhouse Gas Control* 90, p. 102826. DOI: 10.1016/j.ijggc.2019.102826.

Vrolijk, Peter J.; Urai, Janos L.; Kettermann, Michael (2016): Clay smear: Review of mechanisms and applications. In *Journal of Structural Geology* 86, p. 95–152. DOI: 10.1016/j.jsg.2015.09.006.

Walsh, J. J.; Torremans, K.; Güven, J.; Kyne, R.; Conneally, J.; Bonson, C. (2018): Fault-Controlled Fluid Flow Within Extensional Basins and Its Implications for Sedimentary Rock-Hosted Mineral Deposits. In Antonio M. Arribas R., J. L. Mauk (Eds.): Metals, Minerals, and Society: Society of Economic Geologists (SEG).

Wang, W.; Olson, J. E.; Prodanović, M.; Schultz, R. A. (2018): Interaction between cemented natural fractures and hydraulic fractures assessed by experiments and numerical simulations. In *Journal of Petroleum Science and Engineering* 167, p. 506–516. DOI: 10.1016/j.petrol.2018.03.095.

Wang, X.; Mauldon, M. (2006): Proportional errors of the Terzaghi correction factor. In *American Rock Mechanics Association ARMA*.

Wang, Yulun; Grammer, G. Michael (2019): Characterizing the distribution of natural fractures from outcrop in a Mississippian-aged mixed carbonate-chert system, Mid-Continent, USA. In Donald F. McNeill, Paul Harris, Eugene C. Rankey, Jean C.C. Hsieh (Eds.): *Carbonate Pore Systems: New Developments and Case Studies*: SEPM (Society for Sedimentary Geology), p. 141–161. DOI: https://doi.org/10.2110/sepmsp.112.15.

Warnecke, M.; Aigner, T. (2019): Asymmetry of an epicontinental basin-facies, cycles, tectonics and hydrodynamics: The Triassic Upper Muschelkalk, South Germanic Basin. In *The Depositional Record* 5 (1), p. 147–187. DOI: 10.1002/dep2.59.

Warpinski, N. R.; Teufel, L. W. (1989): In-Situ Stresses in Low-Permeability, Nonmarine Rocks. In *Journal of Petroleum Technology* 41 (04), p. 405–414. DOI: 10.2118/16402-PA.

Watkins, H.; Butler, R. W. H.; Bond, C. E.; Healy, D. (2015): Influence of structural position on fracture networks in the Torridon Group, Achnashellach fold and thrust belt, NW Scotland. In *Journal of Structural Geology* 74, p. 64–80. DOI: 10.1016/j.jsg.2015.03.001.

Watkins, H.; Healy, D.; Bond, C. E.; Butler, R. W.H. (2018): Implications of heterogeneous fracture distribution on reservoir quality; an analogue from the Torridon Group sandstone, Moine Thrust Belt, NW Scotland. In *Journal of Structural Geology* 108, p. 180–197. DOI: 10.1016/j.jsg.2017.06.002.

Weber, J.; Born, H.; Moeck, I. (2019): Geothermal energy use, country update for Germany 2016 - 2018. European Geothermal Congress 2019. Den Haag, The Netherlands.

Weijermars, R.; Drijkoningen, G.; Heimovaara, T. J.; Rudolph, E.S.J.; Weltje, G. J.; Wolf, K.H.A.A. (2011): Unconventional gas research initiative for clean energy transition in Europe. In *Journal of Natural Gas Science and Engineering* 3 (2), p. 402–412. DOI: 10.1016/j.jngse.2011.04.002.

Wennberg, O. P.; Svånå, T.; Azizzadeh, M.; Aqrawi, A. M. M.; Brockbank, P.; Lyslo, K. B.; Ogilvie, S. (2006): Fracture intensity vs. mechanical stratigraphy in platform top carbonates: the Aquitanian of the Asmari Formation, Khaviz Anticline, Zagros, SW Iran. In *Petroleum Geoscience* 12 (3), p. 235–246. DOI: 10.1144/1354-079305-675.

Werner, W.; Dennert, V. (2004): Lagerstätten und Bergbau im Schwarzwald. Freiburg i. Br.

Westermann, S.; Dogan, T.; Reker, B.; Goerke-Mallet, P.; Wolkersdorfer, C.; Melchers, C. (2020): Evaluation of mine water rebound processes in european coal mine districts to enhance the understanding of hydraulic, hydrochemical and geomechanical processes. In *Done for Good 2.0 - Results in Post-Mining Research*, p. 159–166.

Wibberley, C. A. J.; Gonzalez-Dunia, J.; Billon, O. (2017): Faults as barriers or channels to production-related flow: insights from case studies. In *Petroleum Geoscience* 23 (1), p. 134–147. DOI: 10.1144/petgeo2016-057.

Wileveau, Y.; Cornet, F. H.; Desroches, J.; Blumling, P. (2007): Complete in situ stress determination in an argillite sedimentary formation. In *Physics and Chemistry of the Earth, Parts A/B/C* 32 (8-14), p. 866–878. DOI: 10.1016/j.pce.2006.03.018.

Wiprut, D.; Zoback, M. D. (2000): Fault reactivation and fluid flow along a previously dormant normal fault in the northern North Sea. In *Geology* 28 (7), p. 595. DOI: 10.1130/0091-7613(2000)28%3C595:FRAFFA%3E2.0.CO;2.

Wirth, E. (1962): Die Erdöllagerstätten Badens (Abhandlungen des Geologischen Landesamtes in Baden-Württemberg, 4).

Wolansky, D. (1950): Bergmännisch-Geologisches Übersichtskartenwerk des Rheinisch-Westfälischen Steinkohlenbezikes. Erläuterungen: Großblatt Lippramsdorf. Bochum: Westfälische Berggewerkschaftskasse.

Worum, G.; van Wees, J.-D.; Bada, G.; van Balen, R. T.; Cloetingh, S.; Pagnier, H. (2004): Slip tendency analysis as a tool to constrain fault reactivation: A numerical approach applied to three-dimensional fault models in the Roer Valley rift system (southeast Netherlands). In *Journal of Geophysical Research: Solid Earth* 109 (B2). DOI: 10.1029/2003JB002586.

Wüstefeld, P.; Hilse, U.; Koehrer, B.; Adelmann, D.; Hilgers, C. (2017): Critical evaluation of an Upper Carboniferous tight gas sandstone reservoir analog: Diagenesis and petrophysical aspects. In *Marine and Petroleum Geology* 86, p. 689–710. DOI: 10.1016/j.marpetgeo.2017.05.034.

Wüstefeld, P.; Medeiros, M. de; Koehrer, B.; Sibbing, D.; Kobbelt, L.; Hilgers, C. (2018): Evaluation of a workflow to derive terrestrial light detection and ranging fracture statistics of a tight gas sandstone reservoir analog. In *AAPG Bulletin* (11), p. 2355–2387. DOI: 10.1306/04251817103.

Yielding, G.; Bretan, P.; Freeman, B. (2010): Fault seal calibration: a brief review. In *Geological Society, London, Special Publications* 347 (1), p. 243–255. DOI: 10.1144/SP347.14.

Zhang, F.; Nagel, N.; Lee, B.; Sanchez-Nagel, M. (2013): Fracture network connectivity — A key to hydraulic fracturing effectiveness and microseismicity generation. In Rob Jeffrey (Ed.): Effective and Sustainable Hydraulic Fracturing: InTech.

Zhang, J.; Fan, Y.; Liu, W.; Liu, H.; Xu, B. (2023): In Situ Stress Evolution and Fault-Slip Tendency Assessment of an Underground Gas Storage Reservoir in the Turpan Basin (China): In Situ Stress Measurements and Coupled Simulations. In *Rock Mechanics and Rock Engineering* 56 (11), pp. 8019–8039. DOI: 10.1007/s00603-023-03477-y.

Zhang, J. J. (2019): In situ stress regimes with lithology-dependent and depletion effects. In *Applied Petroleum Geomechanics*: Elsevier, pp. 163–185. DOI: http://dx.doi.org/10.1016/B978-0-12-814814-3.00005-8.

Zhang, X.; Sanderson, D. J.; Harkness, R. M.; Last, N. C. (1996): Evaluation of the 2-D permeability tensor for fractured rock masses. In *International Journal of Rock Mechanics and Mining Sciences & Geomechanics Abstracts* 33 (1), p. 17–37. DOI: 10.1016/0148-9062(95)00042-9.

Zhang, Y.; Schaubs, P. M.; Zhao, C.; Ord, A.; Hobbs, B. E.; Barnicoat, A. C. (2008): Fault-related dilation, permeability enhancement, fluid flow and mineral precipitation patterns: numerical models. In *Geological Society, London, Special Publications* 299 (1), p. 239–255. DOI: 10.1144/SP299.15.

Zhao, Jian; Konietzky, Heinz (2021): An overview on flooding induced uplift for abandoned coal mines. In *International Journal of Rock Mechanics and Mining Sciences* 148, p. 104955. DOI: 10.1016/j.ijrmms.2021.104955.

Ziegler, P. A. (1982): Geological Atlas of Western and Central Europe. The Hague, Bath, Eng.: Shell Internationale Petroleum Maatschappij B.V.; Distributed by Geological Society Publishing House.

Ziegler, P. A. (1990): Geological atlas of Western and Central Europe. 2nd and completely rev. ed. The Hague, Bath, Eng.: Shell Internationale Petroleum Maatschappij B.V.; Distributed by Geological Society Publishing House.

Ziegler, P. A. (1992): European Cenozoic rift system. In *Tectonophysics* 208 (1-3), p. 91–111. DOI: 10.1016/0040-1951(92)90338-7.

Ziegler, P. A.; Dèzes, P. (2005): Evolution of the lithosphere in the area of the Rhine Rift System. In *International Journal of Earth Sciences (Geologische Rundschau)* 94 (4), p. 594–614. DOI: 10.1007/s00531-005-0474-3.

Zimmermann, G.; Moeck, I.; Blöcher, G. (2010): Cyclic waterfrac stimulation to develop an Enhanced Geothermal System (EGS)—Conceptual design and experimental results. In *Geothermics* 39 (1), p. 59–69. DOI: 10.1016/j.geothermics.2009.10.003.

Zimmermann, G.; Zang, A.; Stephansson, O.; Klee, G.; Semiková, H. (2019): Permeability Enhancement and Fracture Development of Hydraulic In Situ Experiments in the Äspö Hard Rock Laboratory, Sweden. In *Rock Mechanics and Rock Engineering* 52 (2), p. 495–515. DOI: 10.1007/s00603-018-1499-9.

Zoback, M. D.; Kohli, A. H. (2019): Unconventional Reservoir Geomechanics: Cambridge University Press.

Zoback, Mark D. (2007): Reservoir Geomechanics. Cambridge: Cambridge University Press.

Zucchi, M. (2020): Faults controlling geothermal fluid flow in low permeability rock volumes: An example from the exhumed geothermal system of eastern Elba Island (northern Tyrrhenian Sea, Italy). In *Geothermics* 85, p. 101765. DOI: 10.1016/j.geothermics.2019.101765.

8 Appendix

Supplementary technical information on chapters 2 and 3

Supplementary justification for the use of different published S_{Hmax} azimuth data in Chapter 2 ('Fracture network characterisation of the naturally fractured Upper Carboniferous sandstones combining outcrop and wellbore data, Ruhr Basin, Germany') and Chapter 3 ('Post-mining related reactivation potential of faults hosted in tight reservoir rocks around flooded coal mines, eastern Ruhr Basin, Germany').

The published S_{Hmax} azimuth data from Niederhuber et al. (2023) used in Chapters 2 and 3 differ slightly (Chapter 2: N154° ± 33°; Chapter 3: N156°E ± 13°), despite both studies focusing on challenges within the Ruhr Basin. Chapter 2 examines the potential use of Upper Carboniferous sandstones as a reservoir lithology for future deep geothermal utilization in the Ruhr Basin. Given the difficulties in characterizing the stress field without sufficient deep-reaching offset wells, the S_{Hmax} azimuth used in this chapter is derived from a broader stress indicator dataset, including data from deep boreholes, earthquake focal mechanism, and hydraulic fracturing measurements in mines. In contrast, Chapter 3 investigates post-mining related fault reactivation in the area around existing mine infrastructure. For this purpose, an S_{Hmax} azimuth (N156°E ± 13°) is employed, based specifically on stress data from hydraulic fracturing measurements conducted in mines.

In general, there is only a minor deviation between the used S_{Hmax} mean values (N154° vs. N156°); however, the associated standard deviations differ significantly (± 33° vs. ± 13°).